Influence of hydrogen on the magnetic properties of ultrathin cobalt films in contact with electrolyte

Hyeonseok Sim

INSTITUT POLYTECHNIQUE DE PARIS

NNT : 2022IPPAX035

Thèse de doctorat

Influence of hydrogen on the magnetic properties of ultrathin cobalt films in contact with electrolyte

Thèse de doctorat de l'Institut Polytechnique de Paris
préparée à l'Ecole polytechnique

École doctorale n°626 Ecole Doctorale de l'Institut Polytechnique de Paris (ED IP Paris)
Spécialité de doctorat : Physique

Thèse présentée et soutenue à Palaiseau, le 9 Mai 2022, par

HYEONSEOK SIM

Composition du Jury :

Henri-Jean Drouhin Professeur, Ecole Polytechnique (LSI)	Président
Eric Sibert Chargé de recherches, Université de Grenobles Alpes (LEPMI)	Rapporteur
Nicolas Rougemaille Directeur de recherches, CNRS (Institut Néel)	Rapporteur
Fouad Maroun Directeur de recherches, Ecole Polytechnique (PMC)	Directeur de thèse
Philippe Allongue Directeur de recherches, Ecole Polytechnique (PMC)	Co-directeur de thèse

Abstract

Magnetic ultrathin films have been investigated for decades because of their applications from sensors to memory and data storage devices. Following the modern trend of the downsizing of electronic devices, lowering the energy consumption of the device becomes the main challenge. In this context, controlled manipulation of magnetic properties of a given ferromagnetic material (FM) is crucial to designing low-energy consumption magnetic memory devices. Among various methods to control magnetic properties, voltage control of magnetism (VCM) has been studied mostly in solid-state devices. Voltage control magnetism (VCM) means that applying a voltage between a FM layer and a gate electrode separated by an insulating layer is able to change the magnetic property of the FM layer. However, solid-state devices with VCM study suffer from the inhomogeneity of the dielectric layer which may result in leakage current or dielectric breakdown. In a few studies, VCM was investigated using the electrochemical interface offering several advantages as large (1V/nm) and spatially homogeneous electric field. While studying the VCM in the electrochemical interface (or in the solid-state devices), induced chemical reactions such as hydrogen evolution reaction or the surface oxidation of the magnetic material result in the modification of the magnetic property. Among them, H-insertion into magnetic material or adjacent material (such as substrate) can affect the magnetic property of the sample such as the magnetic anisotropy energy (MAE). To study this kind of chemical reaction on the sample, electrochemistry is best placed for offering the possibility to induce potential-controlled chemical reactions which may result in modifying the magnetic properties.

In this work, we investigate the influence of hydrogen evolution reaction (HER) on the ferromagnetic thin Co layer ($0.5\sim1$ nm) in contact with the electrolyte. The ferromagnetic Co layer is prepared either by electrodeposition or by sputtering on Pt buffer layers. The thickness of the Co layer is optimized to have perpendicular magnetic anisotropy (PMA) in the electrolyte after adsorbing CO on the Co surface. Magnetic properties of Co layer in contact with the electrolyte are characterized using the polar magneto-optical Kerr effect (PMOKE) using a standard PMOKE setup or a MOKE microscopy setup both operated *in situ*. To induce the hydrogen evolution reaction on the sample, HER pulses are systematically applied to study irreversible magnetic property variations. Accumulation of HER pulses induces the decrease of the coercive field (H_c), the saturation magnetization (M_s), the slope of the electric field effect (Γ), and the sample optical reflectivity. Similar experiments were also done on bare Pt to

identify the substrate contribution to the magnetic properties. The Co magnetic property variations upon HER pulses are also investigated as a function of the Co thickness. Using MOKE microscopy, we show that magnetic domain wall (MDW) propagation velocity depends on the applied potential. The effect of HER pulses is that MDW velocity increases continuously indicating the reduction of the PMA. At the same time, magnetic domain nucleation density decreases with increasing number of HER pulses. This may imply an alleviation of defect distribution of the Co layer. Taking advantage of the electrochemistry, the accumulated charge (q_{HER}) is introduced to discuss throughout the different experiments. The changes in the Co magnetic properties are discussed in light of the insertion of H in the Pt layer and its presence at the Pt/Co interface.

Résumé

Les films magnétiques ultra-minces ont été étudiés pendant des décennies en raison de leurs applications allant des capteurs aux mémoires et dispositifs de stockage de données. Suivant la tendance moderne de la réduction de la taille des appareils électroniques, la réduction de la consommation énergétique de l'appareil devient le principal défi. Dans ce contexte, la manipulation contrôlée des propriétés magnétiques d'un matériau ferromagnétique (FM) donné est cruciale pour concevoir des mémoires magnétiques peu gourmands en énergie. Parmi les diverses méthodes de contrôle des propriétés magnétiques, le contrôle du magnétisme par l'application d'un champ électrique (VCM) a été étudié principalement dans les dispositifs tout solides. Le magnétisme de contrôle de tension (VCM) signifie que l'application d'une tension entre une couche FM et une électrode de grille séparées par une couche isolante est capable de modifier la propriété magnétique de la couche FM. Cependant, les dispositifs à semi-conducteurs avec étude VCM souffrent de l'inhomogénéité de la couche diélectrique qui peut entraîner un courant de fuite ou une panne diélectrique. Dans quelques études, le VCM a été étudié en utilisant l'interface électrochimique offrant plusieurs avantages comme un champ électrique important (1V/nm) et spatialement homogène. Lors de l'étude du VCM dans l'interface électrochimique (ou dans les dispositifs à l'état solide), des réactions chimiques induites telles que la réaction de dégagement d'hydrogène ou l'oxydation de surface du matériau magnétique entraînent la modification de la propriété magnétique. Parmi eux, l'insertion de H dans un matériau magnétique ou un matériau adjacent (tel qu'un substrat) peut affecter la propriété magnétique de l'échantillon, telle que l'énergie d'anisotropie magnétique (MAE). Pour étudier ce type de réaction chimique sur l'échantillon, l'électrochimie est la mieux placée pour offrir la possibilité d'induire des réactions chimiques contrôlées en potentiel pouvant entraîner une modification des propriétés magnétiques.

Dans ce travail, nous étudions l'influence de la réaction de dégagement d'hydrogène (HER) sur des couches ultraminces ferromagnétiques de Co (0,5 ~ 1 nm) en contact avec un électrolyte. La couche ferromagnétique de Co est préparée soit par dépôt électrochimique, soit par pulvérisation cathodique sur des couches tampons de Pt. L'épaisseur de la couche de Co est optimisée pour avoir une anisotropie magnétique perpendiculaire (PMA) dans l'électrolyte après adsorption du CO sur la surface du Co. Les propriétés magnétiques de la couche de Co en contact avec l'électrolyte sont caractérisées par effet Kerr magnéto-optique polaire (PMOKE) en utilisant une configuration PMOKE standard ou une configuration de microscopie MOKE,

toutes deux opérées in situ. Pour induire la réaction de dégagement d'hydrogène sur l'échantillon, des impulsions HER sont systématiquement appliquées pour étudier les variations irréversibles des propriétés magnétiques. L'accumulation d'impulsions HER induit la diminution du champ coercitif (*Hc*), de l'aimantation à saturation (*Ms*), de la pente de l'effet du champ électrique (Γ) et de la réflectivité optique de l'échantillon. Des expériences similaires ont également été réalisées sur du Pt nu pour identifier la contribution du substrat aux propriétés magnétiques. Les variations des propriétés magnétiques du Co en fonction des impulsions HER sont également étudiées en fonction de l'épaisseur du Co. En utilisant la microscopie MOKE, nous montrons que la vitesse de propagation des parois de domaine magnétique (MDW) dépend du potentiel appliqué. Les impulsions HER induisent une augmentation continue de la vitesse du MDW indiquant la réduction du PMA. Dans le même temps, la densité de nucléation des domaines magnétiques diminue avec l'augmentation du nombre d'impulsions HER. Cela peut impliquer une atténuation de la distribution des défauts de la couche de Co. Profitant de l'électrochimie, la charge accumulée est introduite pour discuter tout au long des différentes expériences. Les changements des propriétés magnétiques du Co sont discutés à la lumière de l'insertion de H dans la couche de Pt et de sa présence à l'interface Pt/Co.

Acknowledgments

First of all, I would like to thank my supervisors Fouad Maroun and Philippe Allongue for their kind directions during my Ph. D period. Even though there was a hard period because of the outbreak of the COVID-19, they dedicated their efforts to help me completing my Ph.D. I am also grateful to Francis Bern who had his postdoctoral research with me when I started my Ph. D. I would like to acknowledge Hélène Béa (Spintec, Grenoble) for providing the samples which are used throughout the thesis. I am indebted to Jean-Paul Adam (C2N, Université Paris-Saclay) who gave me the space for using MOKE microscopy. I want to mention LPMC members, Mathis Plapp, Anne-Chantal Gouget, François Ozanam, Christophe Renault, Catherine Villeneuve, Anne Moraillon, Michel Rosso, Cassiana Andrei, Mathilde Bouvier, Alexandre Da Silva, Yue Feng, Ivan Pacheco, Ngoc Tram Phung, Weichu Fu. I would like to thank all researchers and doctoral students in LPMC for enriching my Ph. D life. I was honored to work with all of the above.

Especially, I would also like to express my gratitude to my Korean friends, Gookbin Cho, Junha Park, Thomas Sanghyuk Yoo, YongJeong Lee, Sangjun Park, Seonyong Park, Jeongmo Kim, Sunggil Kang, Yunho Ahn, Junbeom Park who filled the loneliness in a distant foreign country.

Lastly, I would like to express my deepest love to my family for all their support.

Table of contents

Abbreviations

CE	Counter electrode
CO	Carbon monoxide
CV	current-voltage curve, or voltammogram
d^*	Spin reorientation transition thickness
d_{Co}	Co thickness
DFT	Density functional theory
DMI	Dzyaloshinskii-Moriya interaction
DW	Domain wall
E	Applied electric field
E_A	Activation energy
E_B	Energy barrier
E_F	The Fermi level
EDX	Energy dispersive x-ray spectroscopy
EFE	Electric field effect
EL	Electrolyte
FM	Ferromagnetic material
H	magnetic field
H_c	Coercivity, Coercive field
H_{sat}	Saturation magnetic field
H_{dep}	Depinning field
HER	Hydrogen evolution reaction
HM	Heavy metal
H_{nuc}	Nucleation magnetic field
H_{prop}	Propagation magnetic field
K_{eff}, K_{MAE}	Effective anisotropy energy
K_s	Surface anisotropy constant
K_v	Bulk anisotropy constant
M	Magnetization
M_r	Remanence
M_s	Saturation magnetization
MAE	Magnetic anisotropy energy
MBE	Molecular beam epitaxy
MDW	Magnetic domain wall
M-H	Magnetic hysteresis plot
ML	Monolayer
MOKE	Magneto-optical Kerr effect
MRAM	Magnetic random access memory
MSE	Mercury-mercurous sulfate electrode
MTJ	Magnetic tunneling junction
NM	non-magnetic metal

PMA	Perpendicular magnetic anisotropy
PMOKE	Polar magneto-optical Kerr effect
R	Reflectivity
RE	Reference electrode
SEM	Scanning electron microscope
SOC	Spin-orbit coupling
SRT	Spin reorientation transition
STT	Spin transfer torque
T	Temperature
t_{dep}	Deposition time
U	Applied potential
U_c	Scaling energy constant
U_{dep}	Deposition potential
U_{HER}	Applied potential to induce the hydrogen evolution reaction
UHV	Ultra-high vacuum
v_{dw}	DW velocity
VCM	Voltage control of magnetism
WE	Working electrode
XMCD	X-ray magnetic circular dichroism
XPS	X-ray photoelectron spectroscopy
β	Electric field effect constant [J $\mathrm{V^{-1}m^{-1}}$]
δ_c	The distance between the Co surface and the plane of counter cations at the CO-covered cobalt surface
μ	Creep exponent
φ	The angle between the magnetization and the easy axis
φ_{Kerr}	Kerr rotation angle
Γ	Relative H_c dependence on applied potential, $\Gamma = \frac{\Delta H_c / H_c^0}{\Delta U}$

Chapter 1. General Introduction

The control of magnetism has been intensively investigated during the past few decades [1], [2] because of its application area such as magnetic data storage [3]–[5]. The signal switching between "0" and "1" is the basic principle for making an information storage device. One important building block of such devices is magnetic tunneling junctions (MTJ) [6]–[8]. The MTJ is composed of three layers: The free magnetic layer, the insulating layer, and the reference magnetic layer (see Figure 1-1). The free and the reference ferromagnetic (FM) layers maintain their magnetization orientation in the absence of an external magnetic field, i.e., the FM layer presents a sufficiently strong magnetic anisotropy energy (MAE) that is larger than several times the thermal energy. The magnetization direction of the reference layer is fixed while that of the free FM layer can be switched by a spin-polarized current or an external magnetic field. The resistance of the MTJ is determined by the relative magnetization directions of these two layers. If the magnetizations of the two layers have opposite directions (Figure 1-1 left), the resistance of the MTJ is high (R_{AP}: Antil parallel resistance) and is low when they are parallel (R_P: Parallel resistance). Two different resistance states can be regarded as binary numbers.

To reduce the energy consumption of the device, magnetization switching energy in the free FM layer is the key to achieve this goal. In the case of the spin-transfer torque magnetic random access memory (STT-MRAM), the required spin-polarized current for the magnetization switching is $\sim 10^6 \mathrm{A/cm^2}$ [9]. This large current density may become problematic when the device becomes small [10]. Furthermore, since the general threshold current of the semiconductor is $\sim 10^5 \mathrm{A/cm^2}$ [1], it is necessary to reduce the magnetization switching current. Therefore, adaptive modulation of MAE is desired. Several works proposed ways to modulate the MAE of FM thin layers using strain [11], [12], surface tailoring [13], [14], ion irradiation [15], [16] etc. Among them, voltage control magnetism (VCM), discovered in 2007 [2] appears very promising.

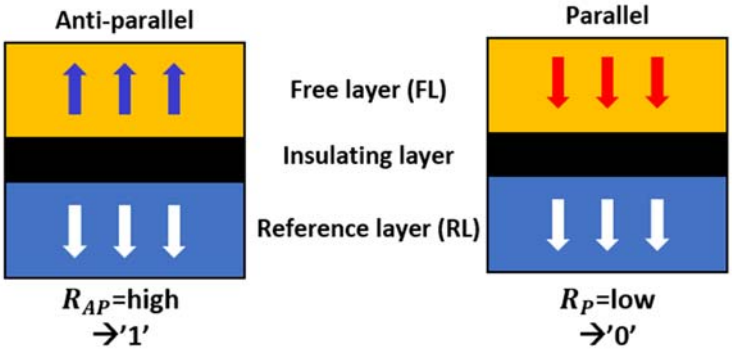

Figure 1-1 The structure of the magnetic tunnel junctions (MTJ). Two magnetic layers (Free layer, Reference layer) are separated by the insulating layer. Left shows the anti-parallel state (R_{AP}) having the opposite magnetization direction between two magnetic layers while the Right shows the parallel state (R_P) having the same magnetization direction.

Voltage control magnetism (VCM) means that applying a voltage between a FM layer and a gate electrode separated by an insulating layer is able to change the magnetic property of the FM layer. The pioneering work of Weisheit *et al*. reported variations of the coercive field by using a liquid contact. The authors immersed a FePd or a FePt film ($2-4\text{nm}$) in an organic electrolyte [2]. The potential was applied between the FM layer and a counter electrode. With this set-up they observed quasi-linear changes in the coercive field (~4%) with the applied potential, justifying the terminology "electric field effect" (EFE). As will be seen below, a large electric field is present at the FM/electrolyte interface. This work has promoted many theoretical studies. Nakamura *et al*. reported that VCM is due to the electric field-induced changes in the band structure of the *p* orbitals near the Fermi level [17]. Tsujikawa *et al*. investigated a Pt/Fe/Pt/vacuum system and showed PMA change by accumulating charges at the interface through filling the *3d* orbital [18].

Weisheit work promoted many studies employing a solid-state structure, where a dielectric layer is deposited on the FM layer and a gate electrode is then deposited on top to apply a voltage between the FM and the gate. For instance, U. Bauer *et al*. [19] investigated the influence of applied voltage on the magnetic property of ZrO_x/MgO/Fe sample. By applying a negative bias ($V_G < 0$, white region in Figure 1-2), the coercive field (H_c) varied linearly while a non linear dependence is observed for $V_G > 0$ (gray region in Figure 1-2). While the linear behavior is consistent with EFE, the authors directly correlated the non-linear variations with the motion of ionic charges in the ZrO_x layer. Such phenomenon is called magneto-ionic effect

[20]. The authors pointed out that after releasing the bias, it took a few days to recover the sample's initial magnetic state. Works with solid state systems have revealed that VCM mechanisms may be quite different from pure EFE. In particular, it has been shown that the FM layer may be oxidized upon the deposition of the oxide layer and also in the presence of an applied voltage [1], [21], [22]. These mechanisms have been discussed in many publications [23]–[25] and these have been reviewed by Dieny and Chshiev [20]. In this article, the authors introduce a coefficient beta (β) that quantifies the magnitude of VCM (Figure 1-3).

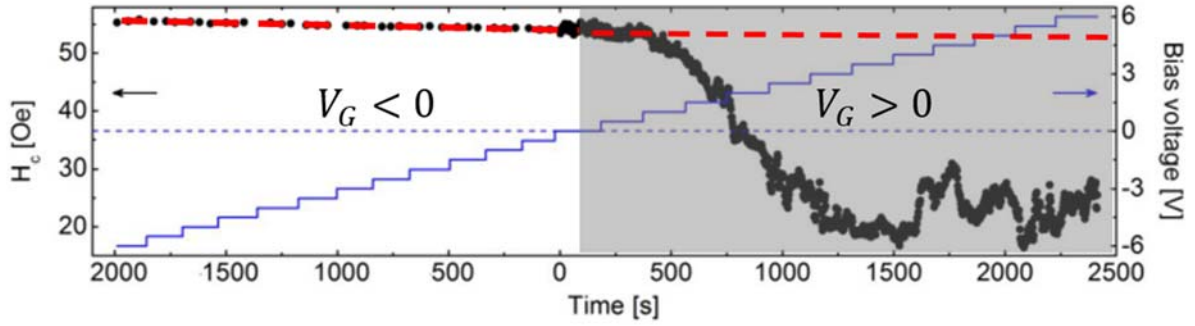

Figure 1-2 Dependence of H_c on bias voltage and bias dwell time. At negative bias (white region), H_c varies linearly with applied potential while a strong decrease of H_c is observed at positive bias (gray region). Figure is adapted from [19].

From the linear variation of the MAE on the applied electric field, thus the slope (β) can be characterized. The EFE coefficient β is expressed in energy per voltage per length [fJ V^{-1} m^{-1}]. Maruyama *et al*. [26] showed a relatively small electric field ($\sim$100mV/nm) applied on Au/Fe/MgO/polyimide/ITO junction. The perpendicular magnetic anisotropy (PMA) in this junction is showed $\sim$8.4 $\mu J/m^2$ and this varies $\sim$90 $\mu J/m^2$ by 1 V/nm ($=$ 90 fJ V^{-1} m^{-1}). Later work of the same group investigated Au/$Fe_{80}Co_{20}$/MgO/Fe/Au MTJs. Surface MAE change is reported as $\sim$37.5 fJ V^{-1} m^{-1} which is smaller than the previous work in Au/Fe/MgO. Later works pointed out that this may be due to the charge trap behavior at the MgO/polyimide interface [26], [27]. Pure electrical manipulation of the MAE of $Co_{40}Fe_{40}B_{20}$ film is also investigated showing the transition of magnetization from in-plane to out-of-plane by applying low voltages [28]. Reported works described above are regarded as "electric field effect induced VCM". They correspond to values of $\beta < 10^2$ fJ V^{-1} m^{-1} (see Figure 1-3).

More recently, VCM studies have reported β values that are 1~2 orders of magnitude larger. Among various starting works on this phenomenon, one group investigated

Au/ $Fe_{80}Co_{20}$ /MgO/polyimide/ITO structure showing PMA variation more than 800 fJ V^{-1} m^{-1} [29]. In Bauer's work [19] that was mentioned above, β is derived as ~944 fJ V^{-1} m^{-1} at positive bias. The author attributed this change to the charge density trapped in an adjacent layer. Furthermore, one work showed that applying a voltage may induce reversible oxidation state change, then the oxidation state influences the magnetism at FeCo/MgO interface [21]. In 2015, Beach's group showed voltage-driven O_2 migration in GdO_x/Co/Pt *in situ* [30] which enables electrochemical variation of interfacial MAE. Derived VCM coefficient shows β ~5000 fJ V^{-1} m^{-1} in this study. Additionally, voltage-induced mechanical strain can result in the change of MAE showing β~7000 fJ V^{-1} m^{-1} [31]. These groups are categorized in the "magneto-ionic induced' or "strain-induced" VCM (see $\beta > 10^2$ fJ V^{-1} m^{-1} group in Figure 1-3).

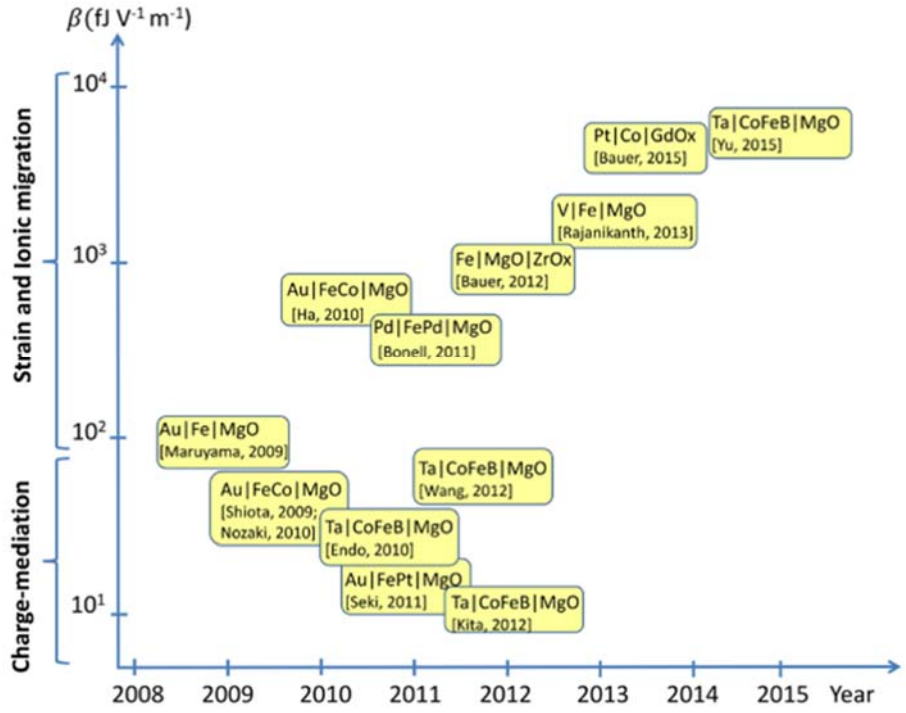

Figure 1-3 A schematic summary of experimental reports relating to the electric field effect (EFE) coefficient β. Figure is adapted from [20].

Because this is relevant to the present work, one must be mentioned that other VCM mechanism exists besides magneto-ionics. Another work of Beach's group used H^+ pumping to control the MAE of GdO_x/Co/Pt device (see Figure 1-4a) [32]. Metals like Pt and Pd [33], [34] have high spin-orbit coupling which induces perpendicular magnetic anisotropy (PMA) when they are in contact with a FM layer [35], [36]. In the work of [32], authors showed 90°

magnetization switching by H^+ insertion while applying the potential and $\beta \sim 5000$ $fJV^{-1}m^{-1}$. This VCM is reversible and fast, and the 90° magnetization switching took place within $\sim 100ms$ at room temperature (from Virgin state to $V_G = 3V$ in Figure 1-4b). The influence of atomic H on the magnetic properties of FM layers is well-known. It has been studied by S. M. Valvidares *et al*. [37] who compared sputtered Co layer on Pt and H covered Pt. Co/H/Pt system presents in-plane magnetization whereas Co/Pt has PMA. This work correlated the presence of H with the reduction of the magnetic moment at Co/Pt interface or with the decoupling of the Pt substrate from the Co. Theoretically, the DFT calculation work of K. Klyukin *et al*. [38] showed the influence of H at the FM/HM (HM: heavy metal) interfaces on the magnetic anisotropy energy. This work showed that the accumulation of H at FM/HM interface affects the hybridization of the spin-orbit coupling (SOC) and eventually reduces the PMA in Co/Pd or Co/Pt.

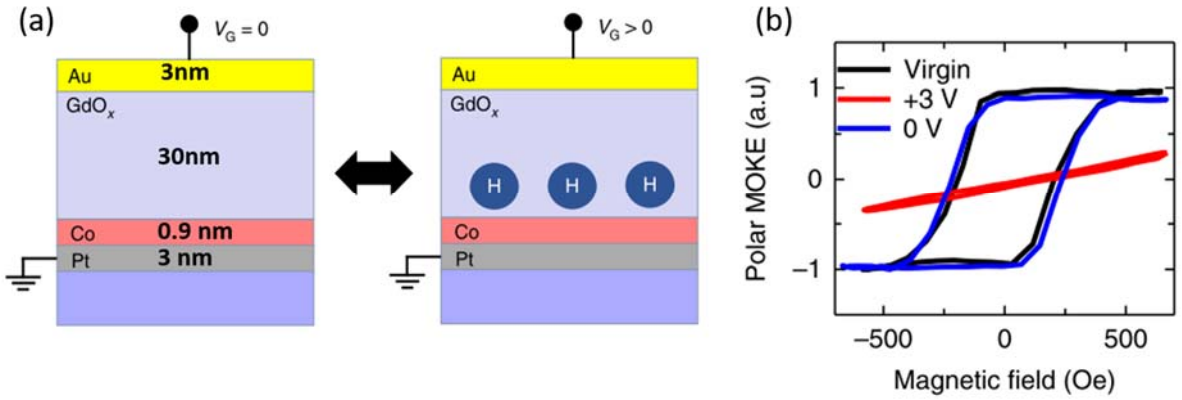

Figure 1-4 (a) Schematic of magneto-ionic switching scheme. H indicates hydrogen at the Co/GdO_x interface. (b) Magnetic hysteresis loops in different states: Virgin state (black), $V_G = +3V$ (red), and $V_G = 0V$ (blue). Figure is adapted from [32].

In the context of using atomic H to modify the MAE, electrochemistry is best placed for the generation of atomic H may be controlled by the applied potential, while promoting the so-called hydrogen evolution reaction (HER). Hydrogen evolution is the electrochemical reduction of protons to form H_2. The global reaction is $H^+ + e^- \rightarrow H_2$ (it will be discussed in more detail in Chapter 2. 3). HER with the electrochemistry, one group reported that the nanoporous Pd/Co in the electrolyte shows the magnetization change upon hydrogen charge (hydrogen absorption in Pd) [39].

Our group studied the potential dependence of the magnetic properties of electrodeposited

Pd/Co/Au(111) layers [40]. In this work, a 4ML of Co capped by a Pd layer is electrodeposited on Au(111) substrate (scheme on the right corner in Figure 1-5). The electrochemical insertion/release of H into/from the Pd overlayer results in the reversible modification of the coercive field of the Co layer (Figure 1-5b). Other works from our group reported the influence of hydrogen on magnetic properties while investigating the VCM on a Co layer in contact with the electrolyte. Tournerie *et al*., electrodeposited Co on Au(111) and passivated the Co surface with CO to increase the Co layer PMA. The authors showed an electric field-induced change in surface anisotropy with the value of $\sim 34 \mathrm{fJ/Vm}$ when the potential remained outside the HER regime [14], [41]. However, the variations become strongly non-linear when the applied potential enters the HER regime. The later work of A. Lamirand *et al*. showed similar behavior when the Co layer is electrodeposited on a Pd substrate [42]. It should be noted that the observed effects are reversible in all these studies since the magnetic properties return to their initial state after applying potential out of the HER regime. Furthermore, these works showed that setting a FM in contact with the electrolyte presents some advantages to study VCM because a large $(> 1 \mathrm{V/nm})$ and spatially homogeneous electric field exists at the FM layer/electrolyte interface [14].

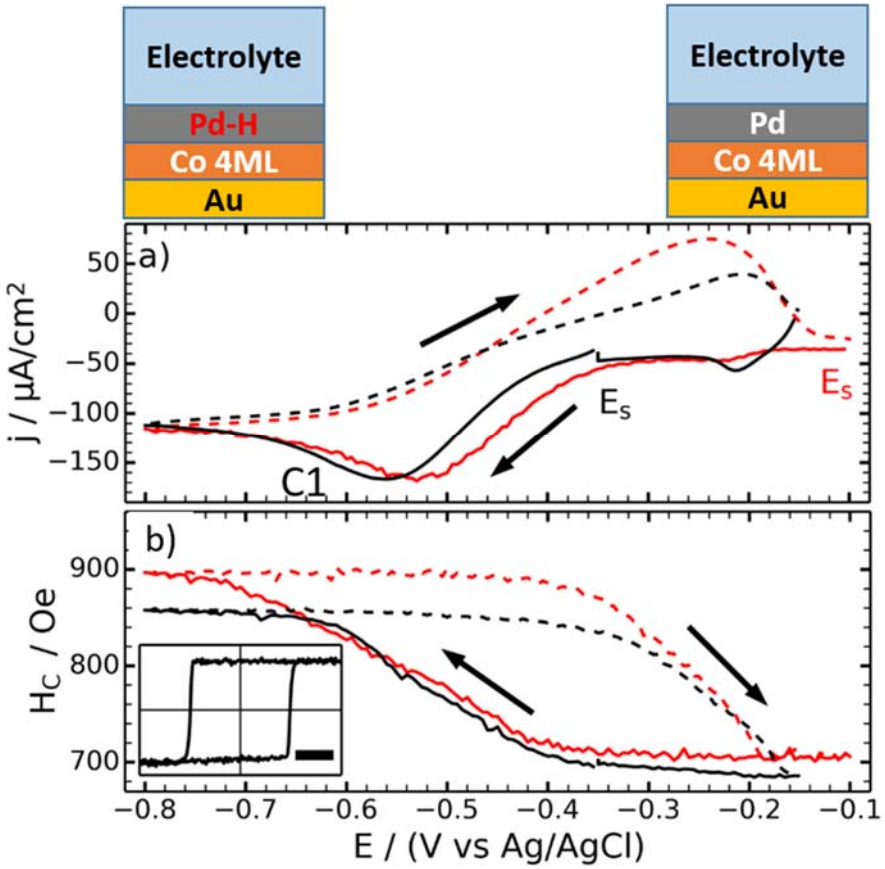

Figure 1-5 (a) Cyclic voltammograms of the Pd/Co/Au (111) interface. C1 indicates the hydrogen evolution reaction cathodic current. (b) Corresponding variations of the coercive field H_c. Inset shows the magnetic hysteresis. Two schemes above data panels are representing each state: after hydrogen evolution reaction (left) and the pristine state (right, or after releasing the hydrogen). The figure is adapted from [40].

The objective of the present work is to investigate VCM at Co/Pt layers in contact with an electrolyte. The Co layer is covered by a CO-monolayer to start with perpendicularly magnetized layers (see Figure 1-6). The work will focus on the effect of hydrogen on magnetic properties. In Chapter 2, theoretical backgrounds of thin-film ferromagnetism will be presented as well as the experimental setup description based on the magneto-optical Kerr effect (MOKE). In Chapter 3, epitaxial growth of Co on Pt is performed in the electrolyte. Then, magnetic properties are characterized after adsorption of CO with *in situ* PMOKE setup. Hydrogen evolution reaction (HER) on the electrodeposited Co/Pt is studied in detail since HER induces irreversible changes in magnetic property. In Chapter 4, the same HER study is applied on sputter-deposited Co/Pt capped with AlO_x. Post-mortem energy-dispersive X-ray spectroscopy

(EDX) study is used to exclude any Co dissolution during the experiments. In Chapter 5, the DW motion is studied using MOKE microscopy on a sputter-deposited Co/Pt sample in the electrolyte. HER effects on magnetic domain characteristics (potential dependence on DW velocity, DW nucleation density variation…) are intensively studied in this chapter. After describing experimental results from Chapter 3 to Chapter 5, a general discussion throughout the manuscript is presented in Chapter 6. Then general conclusion finalizes the manuscript.

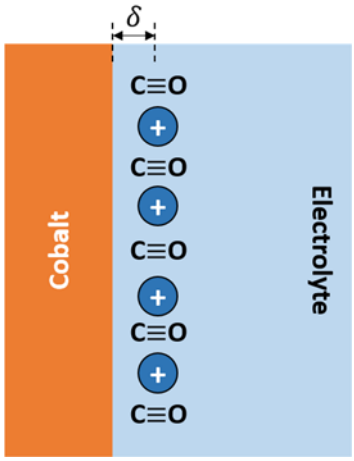

Figure 1-6 Proposed scheme for cobalt interface covered with CO monolayer in the electrolyte. The cations are embedded inside the CO layer. The separation between the Co surface and the first cationic plane is $\delta \sim 0.14\text{nm}$ (adapted from [41]).

Chapter 2. Theoretical background and experimental details

2. 1. Magnetic anisotropy energy (MAE) of ultrathin films

Magnetic anisotropy is the phenomenon where the magnetization has a preference to align with a particular direction (i.e. easy axis $\vec{M}$, see Figure 1-1). The energy governs the magnetic behavior of the material is called magnetic anisotropy energy (MAE). In terms of the energy, it tends to minimize by competing energies contributing to the total MAE. Contributions to the total MAE are well categorized by previous works [43], [44] and we discuss here contribution energies to ultrathin magnetic layers (especially on Co).

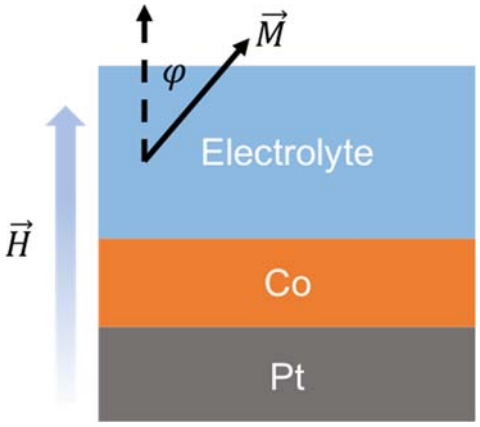

Figure 2-1 The schematic defining the sample geometry and the angle φ between the magnetic easy axis $\vec{M}$ and the sample normal (direction of $\vec{H}$).

a. Magnetostatic anisotropy (shape anisotropy or stray field energy)

The magnetostatic anisotropy (also known as shape anisotropy or stray field energy), results from the magnetization of the sample (M_s). The magnetization generates magnetic poles at the surface of the thin film which encloses the stray fields in a small volume of magnetization. This magnetostatic anisotropy is given by:

$$E_{ms} = -2\pi M_s^2 sin^2\varphi \qquad 2.1$$

In the case of cobalt, M_s is $1407\ \text{emu/cm}^3$ at 298K [14].

b. Magnetocrystalline anisotropy

Crystalline lattice influences the orbits of the atoms through the crystalline electrostatic field (i.e. attraction force between atoms) which interacts with the magnetization through spin-

orbital coupling resulting in the magnetocrystalline anisotropy. For a uniaxial anisotropy, magnetocrystalline energy per unit volume can be written as:

$$E_{mc} = K_{mc,1} sin^2\varphi + K_{mc,2} sin^4\varphi \quad 2.2$$

where φ is the angle between the magnetization and the easy axis. In the case of hcp Co, the easy axis is along c-axis [0001]. $K_{mc,1}$ and $K_{mc,2}$ are derived as $5.3 \times 10^6 \mathrm{erg/cm^3}$ $(= 0.53 \times 10^6 \mathrm{J/m^3})$ and $1.44 \times 10^6 \mathrm{erg/cm^{-3}}$ respectively in the case of hcp Co [45].

c. Magnetic surface anisotropy

Néel was the first to introduce that a surface with the dramatic break of local magnetic symmetry results in strong surface anisotropy. Depending on the magnetization direction on the surface, they are a magnetic contribution to the crystal's free surface (interface) energy. In a quadratic approximation, the magnetic surface anisotropy is given by:

$$E_s = K_s sin^2\varphi / d \quad 2.3$$

where K_s $[\mathrm{erg/cm^2}$ or $\mathrm{J/m^2}]$ is the surface contribution and d is the thickness of a magnetic material. In ultrathin magnetic films, the magnetic surface anisotropy surpasses the demagnetization energy resulting in perpendicular magnetic anisotropy [46].

d. Magnetoelastic anisotropy energy (Strain contribution)

Magnetoelastic energy is related to the deformation of the lattice structure and it can be written as:

$$E_{me} = \frac{3}{2} \lambda \sigma cos^2\phi \quad 2.4$$

where ϕ is the angle between the magnetization and the strain, λ is the magnetostriction which is defined for various crystal directions. σ is the mechanical stress on the sample [47]. Strain in the thin films can be derived from the growth condition such as a lattice mismatch between two layers.

e. Zeeman energy

It is the energy that prefers to align spins along the direction of the applied magnetic field (H_a). The Zeeman energy can be written as:

$$E_z = -M_s H_a cos\varphi \quad 2.5$$

Collecting magnetic anisotropy contributions, we can derive total anisotropy per unit volume as:

$$E_{total} = E_{ms} + E_{mc} + E_s + E_{me}$$
$$= \left[-2\pi M_s^2 sin^2\varphi + K_{1mc} sin^2\varphi + K_{2mc} sin^4\varphi + \frac{3}{2}\lambda\sigma cos^2\phi\right] \quad 2.6$$
$$+ \frac{1}{d}[K_s^{up} sin^2\varphi + K_s^{down} sin^2\varphi]$$

We introduced two surface magnetic anisotropy coefficients K_s^{up} and K_s^{down} which indicate two interfaces in contact with the ferromagnetic layer. d is the thickness of the FM layer. In the simple case where K_{2mc} and σ are zero, Eq. 2.6 can be written as:

$$E_{total} = K_{eff} sin^2\varphi \quad 2.7$$

with

$$K_{eff} = [-2\pi M_s^2 + K_v] + \frac{1}{d}(K_s^{up} + K_s^{down}) \quad 2.8$$

K_v containing different bulk contributions (here $K_{mc,1}$). K_{eff} is known as the effective anisotropy energy (or K_{MAE}). If $K_{eff} > 0$, the easy axis of the magnetization is perpendicular to the surface. When the layer thickens, $K_{eff} < 0$ since $K_v < 2\pi M_s^2$ in most of the systems. The sign change of K_{eff} is accompanied by magnetization easy axis tilt with respect to the surface normal which is known as a spin reorientation transition (SRT).

The hysteresis loop and the magnetic properties

Through the MOKE analysis (which will be explained in Chapter 2. 6), a magnetic hysteresis curve can be obtained and we could learn abundant information about the magnetic properties of a material. The hysteresis loop is acquired by sweeping the magnetic field (H) and measuring the magnetization (M). By using our *in situ* PMOKE, by obtaining Kerr rotation angle, it is proportional to the magnetization of the sample. It is referred to as the M-H loop. Figure 2-2 shows an example of the hysteresis by using our sample.

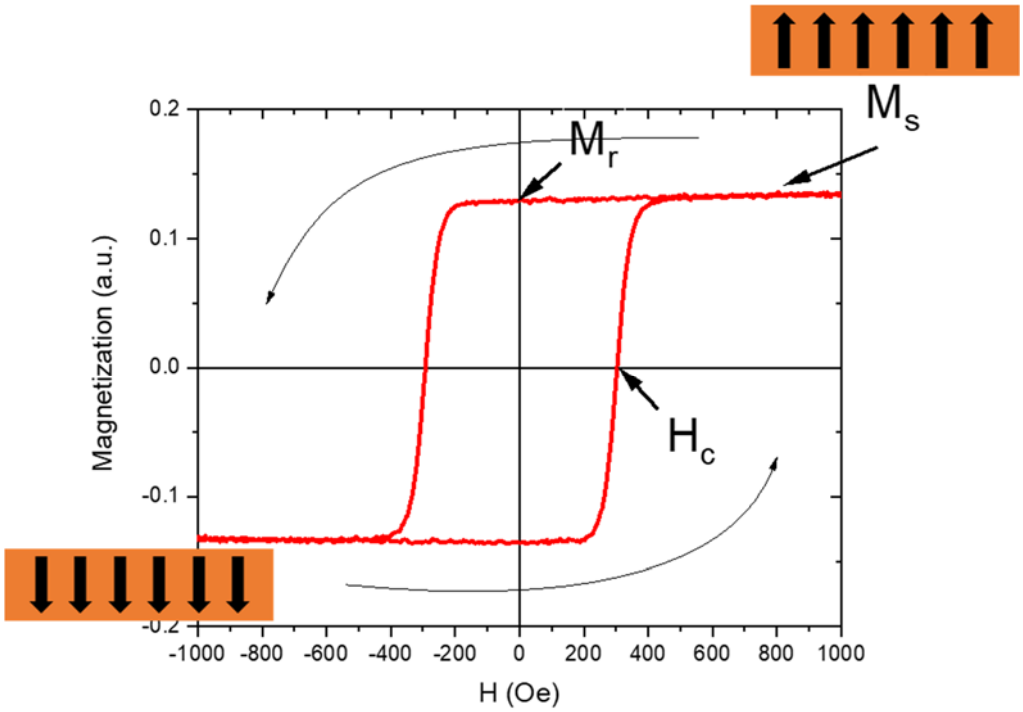

Figure 2-2 Example of the magnetic hysteresis (M-H loop). Magnetic parameters (M_s, M_r, H_c) are indicated and two orange schemes represent magnetic states when the sample is perpendicularly saturated in different directions.

When the magnetic field is sufficiently large (positive or negative), the magnetization reaches a saturation state which is known as M_s. At this state, the sample magnetization is uniformly aligned along the magnetic field. The opposite sign of the magnetization corresponds to the opposite direction. The remanence (M_r) is the magnetization when the applied magnetic field is zero. $M_r \neq 0$ means that the magnetization is non-zero even though the magnetic field is zero. The magnetization sign change (magnetization reversal) corresponds to the coercivity (H_c). H_c is related to the anisotropy energy. The value of H_c is also close to the nucleation field used to study MDW propagation. The theory of the hysteresis loop is explained in the other work [48].

To derive spin reorientation transfer (SRT) thickness (d^*) from the magnetic hysteresis, we use Eq. 2.5 and Eq. 2.7. Minimization of total energy leads to by differentiate (E_{total}):

$$sin\varphi\left[K_{eff} + 2K_{2mc}sin^2\varphi + \frac{HM}{2cos\varphi}\right] = 0 \qquad 2.9$$

In the absence of an external magnetic field, the relation between the φ and magnetic parameters from the hysteresis can be written as [49]:

$$cos\varphi = M_r/M_s = \left[1 + \frac{K_{eff}}{2K_{2mc}}\right]^{1/2} \quad 2.10$$

Since SRT takes place where $\varphi = 45°$, we can derive SRT thickness from Eq. 2.10:

$$d^* = \frac{K_s}{2\pi M_s^2 - K_{1mc} - K_{2mc}} \quad 2.11$$

2. 2. The basic concept of electrodeposition

Electrodeposition is the conventional process of depositing a layer of one metal on top of a different metal by donating electrons to the ions in a solution [50]. The dissolution is the inverse reaction of Eq. 2.12.

$$A^{z+} + Ze^- \leftrightarrow A \quad 2.12$$

2. 2. 1 Structure and energy diagram of metal-solution interface

A metal electrode is an electronic conductor characterized by its Fermi level (E_F) and work function (Φ_F) to extract an electron from the metal. Electrolyte with ions also plays a role as an ionic conductor. The Nernst potential of the redox couple A^{z+}/A is treated as a Fermi level of the electrolyte (Φ_{redox}). When a metal electrode meets an electrolyte, the surface charge of metal is compensated by a reorganization of the charge distribution in the electrolyte, in the close vicinity of the electrode surface ($Q_m < 0$) [51]. The region near the surface is called as Helmholtz layer and it behaves as a capacitor having its typical value as $C_H \sim 10 \mu F/cm^2$ [52].

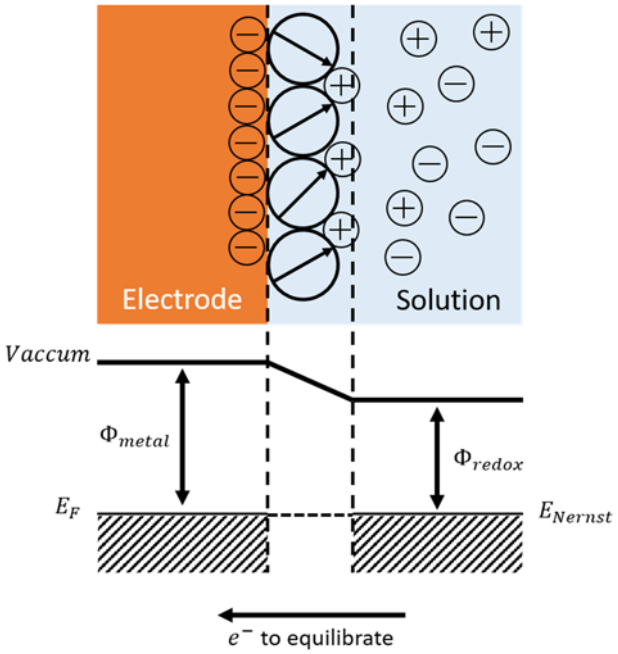

Figure 2-3 Scheme of an electrochemical interface between the metal electrode and the electrolyte. Below shows the energy diagram when the metal electrode meets the electrolyte.

2. 2. 2 Principle of Electrodeposition

Electrodeposition is basically following the Eq. 2.12 by reducing A^{z+} ions. Figure 2-4a shows an energy diagram when a metal electrode is in contact with the electrolyte containing deposition ions with the presence of a reference electrode (U_{ref}). As we can see here, the metal electrode and the electrolyte is in an equilibrium state (See the Fermi level). The equilibrium potential of the redox ($U_{redox} = E(A^{z+}/A)$) in the electrolyte is defined by Nernst equation at 298K:

$$U_{redox} = E(A^{z+}/A) = E^0(A^{z+}/A\ ) + \frac{R_{Gas}T}{zF} ln\left(\frac{[a_{A^{z+}}]}{[a_A]}\right) - U_{ref}$$
$$= E^0(A^{z+}/A) + \frac{0.059}{z} log(\frac{[a_{A^{z+}}]}{[a_A]}) \qquad 2.13$$

In Eq.2.13:

- $E^0(A^{z+}/A)$ is the standard redox potential with respect to SHE (standard hydrogen electrode)
- R_{Gas} is the universal gas constant: $R_{Gas} = 8.31\ J\ K^{-1}\ mol^{-1}$.

- T is the absolute temperature.
- F is the Faraday constant, corresponds to $96500\ \mathrm{C\ mol^{-1}}$.
- z is the number of moles of electrons transferred in the cell reaction.
- U_{ref} is the reference potential versus SHE. Since we use the Mercury-mercurous sulfate electrode (MSE), $E(MSE) = E(SHE) + 0.64\mathrm{V}$ in saturated $\mathrm{K_2SO_4}$.
- $[a_{A^{z+}}]$ and $[a_A]$ are the chemical activity of $\mathrm{A^{z+}}$ cation and metal electrode A respectively. $[a_A]$ is conventionally 1.

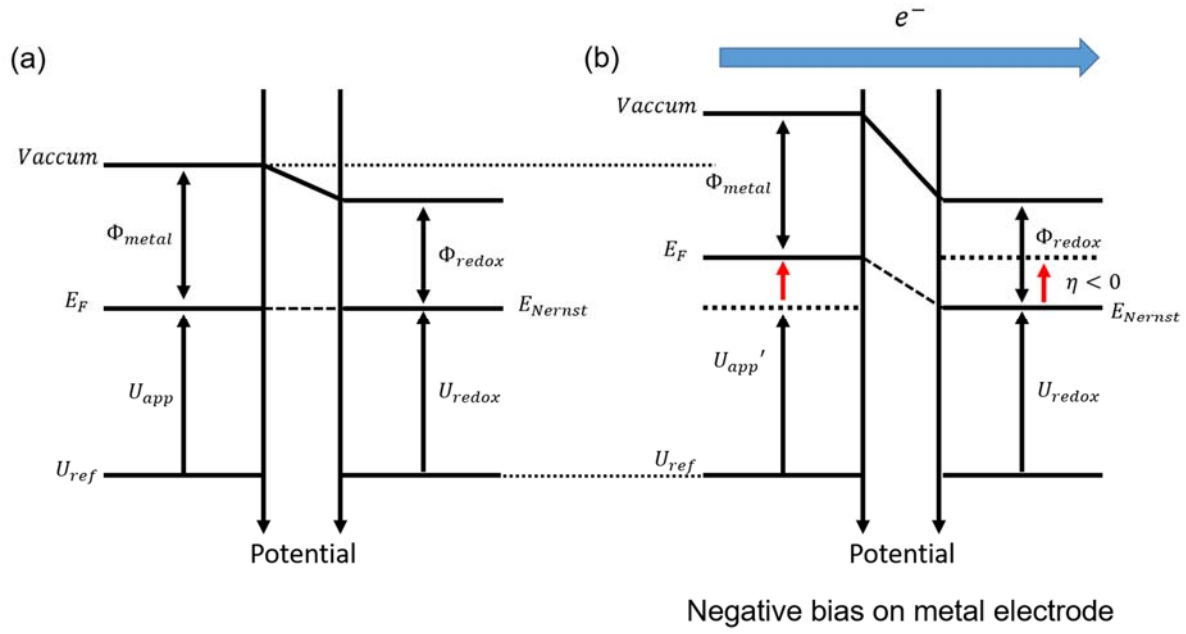

Figure 2-4 (a) Energy band diagram when the metal electrode is in contact with the electrolyte. (b) Applying negative bias on the side of the metal electrode.

However, when we apply negative bias (-) on the metal electrode in Figure 2-4a (applying potential is downward, therefore negative potential is in opposite direction), the energy diagram changes as Figure 2-4b by elevating the energy levels of the metal electrode with respect to the U_{ref} (red arrow on the metal side). To equilibrate the Fermi level between E_F and E_{Nernst}, electrons are transferred from the metal electrode to the electrolyte which induces the reduction of $\mathrm{A^{z+}}$ cations. When we apply positive bias (+) on the metal, the direction of the electron transfer is the opposite. Induced current by transferring electron is expressed as:

$$I = zFKN(E_F)C_{surf} \qquad 2.14$$

where K is the kinetic constant, $N(E_F)$ is the density of state at the Fermi level of the metal, and C_{surf} is the concentration of reactive at the metal surface. Usually, $N(E_F)$ is independent of the applied potential. The kinetic current is the sum of reduction current and oxidation current and it is expressed following the Butler-Volmer equation Eq.2.15 [51].

$$i = i_0 \left[exp\left(\frac{-\alpha z F \eta}{RT}\right) - exp\left(\frac{(1-\alpha) z F \eta}{RT}\right)\right] \quad 2.15$$

where η is the overpotential expressed as $\eta = U_{app} - E_{Nernst}$ when we apply a potential. i_0 is the exchange current density and α is a charge transfer constant. This equation indicates that the current increases exponentially with $|\eta|$. The rate of the electrochemical deposition (current), on the other hand, is influenced not only by charge exchange kinetics but also by ion diffusion to the electrode surface. With a sufficiently large overpotential η, it depletes the electrolyte in A^{z+} if the consumption rate of A^{z+} is faster than diffusion. Therefore, the current density is limited by the diffusion of M^{z+}. This limited current density (j_{diff}) follows the Fick's law [53]:

$$j_{diff} = zFD_0\left(\frac{[A^{z+}]_{surf} - [A^{z+}]_{\infty}}{d}\right) \quad 2.16$$

where d is the diffusion layer thickness, and D_0 is the diffusion coefficient of A^{z+} in the electrolyte ($\sim 10^{-5} cm^{-2}s^{-1}$ for metallic ions and $10^{-4} cm^{-2}s^{-1}$ for protons). $[A^{z+}]_{surf}$ and $[A^{z+}]_{\infty}$ are ion concentrations at the electrode surface and the electrolyte bulk respectively.

In conclusion, electrodeposition near a metal electrode takes place following the above relations. Deposition of nuclei (I) is exponentially influenced by overpotential η however limited by diffusion current (I_{diff}). Therefore, the metallic cation discharge step may become site-selective and influence the nucleation and growth with the small η. In other words, the growth mode and morphology of the sample are influenced by overpotential therefore it may affect the magnetic property of the deposited sample [54].

2. 3. Hydrogen evolution reaction (HER)

The hydrogen evolution reaction (HER) corresponds to the electrochemical reaction of proton reduction to form H_2. In literature, the HER has been described by the set of equations

below:

$$H^+ + e^- + * \rightarrow H^* \quad 2.17$$

$$\mathbf{2H^* \rightarrow H_2} \quad 2.18$$

$$\mathbf{H^+ + e^- + H^* \rightarrow H_2} \quad 2.19$$

where the $*$ denotes a site on the surface and H^* indicates a hydrogen atom adsorbed on the electrode surface to form a M-H chemical bond. The electron is provided by the metal electrode.

Figure 2-5 shows each reaction step. After the initial stage of H-absorption, two pathways are generally considered [55]. One, postulated by Volmer-Tafel, is the chemical combination of two surface H^*. The second, postulated by Volmer-Heyrovsky, is an electrochemical reaction between a proton and one H^*. Both reactions lead to the formation of molecular H_2. A similar reaction set may be written when water is decomposed ($2H_2O \rightarrow H_2 + OH^-$).

The last reaction relevant to this work is the *absorption* of surface atomic H within the metal [56]–[58].

$$H^* \rightarrow H_{abs} \quad 2.20$$

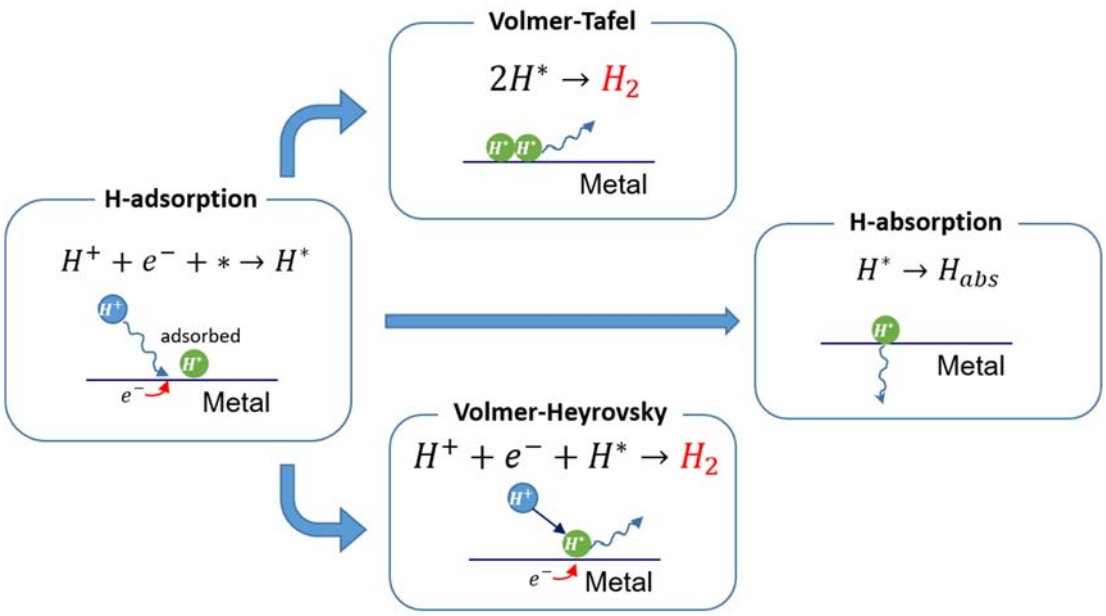

Figure 2-5 Decomposition of the hydrogen evolution reaction at the surface of the metal electrode.

The kinetics of above reactions depend on the strength of the M-H bonds. The HER is often

characterized by its exchange current density (j_0) - the pre-factor of the usual expression of the HER current $j = j_0 \ exp(\left(\frac{E^0 - U}{kT}\right))$ where E^0 is the standard potential of HER [55], [59]. The $\log(j_0)$ depends on the M-H (metal-hydrogen) bond strength as shown in Figure 2-6. This 'Volcano curve' was introduced by Trasatti et al [60] and has been revisited in recent works [59], [61]. It shows that the best HER catalyst are metals for which the M-H bond strength is "just right". If too strong, the desorption steps (2.18 and 2.19) are becoming slow. When too weak the first step becomes slow. According to this plot, the most active metals for the HER are platinum group metals (Pt, Re, Rh, Ir) while (Au, Ni, Co, Fe…) are much less active [55], [62]–[66].

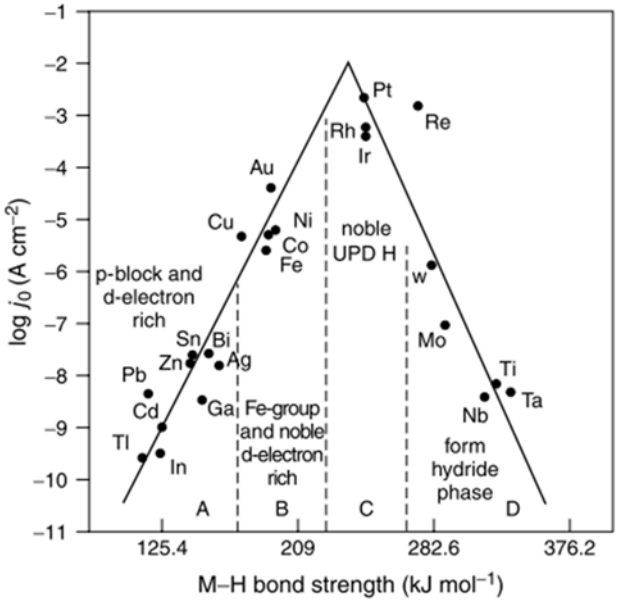

Figure 2-6 Volcano plot of the exchange current density ($\log j_0$) as a function of M-H bond energy for different metals (adapted from [59], [61]).

2. 4. Magnetic domain theory

All materials tend to minimize their energy, and so are magnetic materials. Inside the magnetic material, there are several energy competing with each other to reduce the total energy ($E_{total} = E_z + E_{ex} + E_{ms} + E_{MAE}$). A domain wall (DW or MDW) can be defined as an interface that separates two regions where magnetized in different directions. In case of the exchange energy (E_{ex}), spins should be aligned in parallel to have lower energy ($cos\varphi = 0$). Therefore, E_{ex} try to make the domain wall as wide as possible. However, in terms of the

magnetostatic energy (E_{ms}), domain wall width tends to decrease, and try to make domain walls as much as possible to reduce its energy. Another contribution to create MDW is the anisotropy energy (E_{MAE}). E_{MAE} reduces its energy when spins are aligned along with the easy axis, therefore, E_K tends to have narrow domain wall width. By competing all energy contributions described above, magnetic domains are created in the magnetic material [67].

In terms of the MDW structure, it can be divided into two mainly discussed types: Néel type and Bloch type. They are separated by the rotation of magnetic moments from one neighboring domain to the other neighboring domain. If the rotation is out-of-plane, the domain wall is called as Bloch-type domain wall (Figure 2-7 left). If this rotation is in-plane, it is called as Néel type domain wall (Figure 2-7 right).

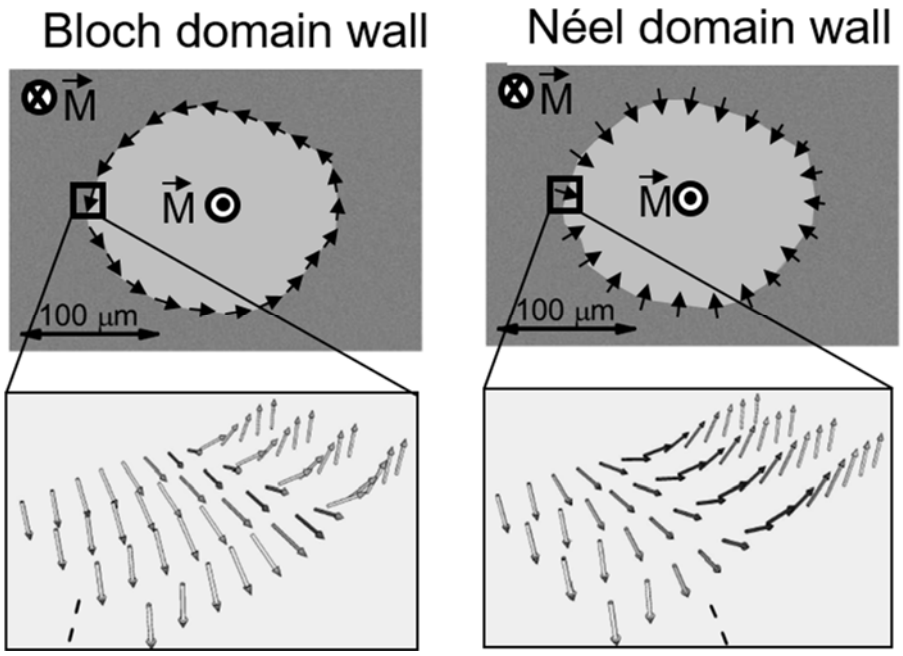

Figure 2-7 Types of domain wall and magnetic spin alignment in each domain wall: Bloch type domain wall (left) and Néel type domain wall (right).

2. 4. 1. Domain wall dynamics in the presence of pinning (creep regime)

Magnetic domain walls interact with defects as elastic interfaces. The elasticity of the magnetic domain wall competes with pinning energy to find the lowest energy arrangement by attempting to flatten the interface. There are fine works to understand the dynamics of MDW depending on the driving force and the thermal effects (Figure 2-8) [68], [69].

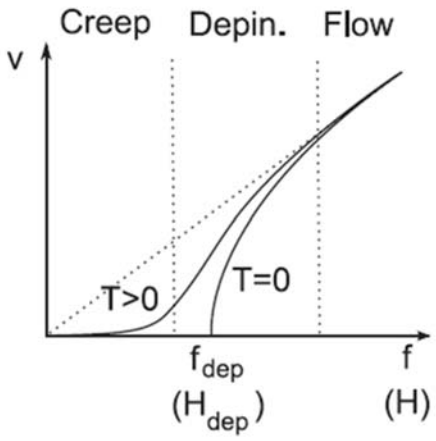

Figure 2-8 (a) Theoretical variation of the velocity v, of a 1D interface in a 2D weakly disordered medium submitted to a driving force, f, at zero and finite temperature, *T*. The creep, depinning, and flow regimes are labeled. (Figure from Metaxas et al. [68]).

DW motion in thin films is regarded as an elastic 1D interface moving in a 2D disordered medium. In this system, DW is collectively pinned before reaching critical force (f_{dep} or H_{dep}) at $T = 0$K (see Figure 2-8a). Elastic energy (E_{el}) and pinning energy (E_{pin}) compete to minimize the free energy of the 1D interface. When the driving force (f or H) reaches to critical force f_{dep} (or H_{dep}), DW interface starts to move. The free energy of the system is given by [69]:

$$F(u,L) = \varepsilon_{el}\frac{u^2}{L} - (\Delta\xi^2 L)^{\frac{1}{2}} - M_s H d_{film} L u \qquad 2.21$$

where ε_{el} is the MDW energy density per unit length, $\Delta = f_{pin}^2 n_i \xi_i$ scales the pinning strength of the disorder (n_i is the pinning center density, f_{pin} is the local pinning force, and ξ_i is the characteristic length of the pinning potential). u is the DW displacement and L is the length of a segment of the DW (see Figure 2-9). The first term of Eq. 2.21 is the elastic energy (E_{el}), the second term is the pinning energy (E_{pin}), and the final term corresponds to Zeeman energy (d_{film} is film thickness). In reference [69], the authors approximated n_i as $n_i \approx 1/\xi_i^2$ for numerical estimations.

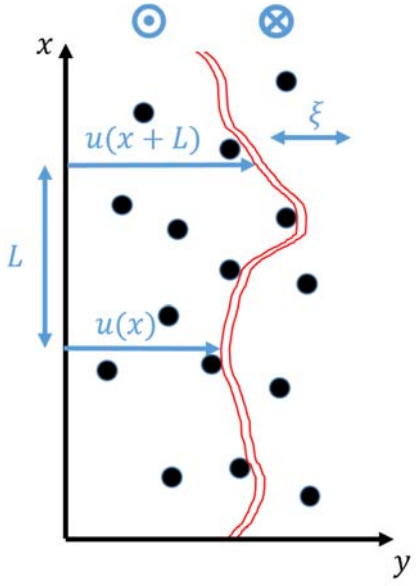

Figure 2-9 Elastic DW in a pinning potential. By applying out of the plane magnetic field H (up), magnetic domain wall (red lines) is propagating towards the y-direction. Black dots represent pinning centers. $u(x)$ is the DW displacement, ξ is the disorder correlation length, and L is the length of a segment of the DW.

We can derive the Larkin length (L_c) and the depinning field H_{dep} from the Eq. 2.21 related to the pinning. At the depinning point (H_{dep}), the displacement of DW $u(x)$ is expected to be same as the average distance of the disorder $\xi \cong u$. The Larkin length (L_c) is determined by the maximum length that DW moves without deformation when the elastic energy (E_{el}) and the pining energy (E_{pin}) are equal. L_c can be derived as:

$$L_c = \xi \left(\frac{\varepsilon_{el}}{f_{pin}} \right)^{2/3} \qquad 2.22$$

In the case of the Bloch type DW, $\varepsilon_{el} = 4(AK)^{1/2}t$, where A is the exchange stiffness and K the anisotropy constant (surface DW energy is $\sigma_{DW} = 4\sqrt{AK}$ and average wall thickness is $\delta_{DW} = \sqrt{A/K}$).

In terms of the H_{dep}, we can correlate with the Zeeman energy term since it is needed to depin a DW. Therefore, we deduce from $E_{pin} = Zeeman\ \ energy$ and Eq.2.21 [70]:

$$H_{dep} = \left(\frac{\varepsilon_{el}\xi}{M_s t} \right) \frac{1}{L_c^2} \ \ at \ \ T = 0K \qquad 2.23$$

However, at finite temperature, there is a DW displacement with $H < H_{dep}$ which is a thermally activated creep regime (see Figure 2-8a). In the creep regime, DW motion is sensitive

to the pinning centers (now, $L > L_c$). Therefore, we should rescale parameters to take into account the roughness into DW displacement arises from pinning centers. Rescaling is done by $L' = aL$ and $u' = a^{-\zeta}u$ [71], [72]. With this rescaling, we obtain a statistically equivalent DW $u'(L')$ where a and ζ are a scaling constant and exponent $u(aL) \sim a^{\zeta}u(L)$.

The geometrical roughness of the interface is characterized by using the spatially and the thermally averaged correlation function $\ll [u(x+L) - u(x)]^2 \gg$. At a static equilibrium, the disorder is relevant the elastic interface string is in a pinned phase characterized by a wandering exponent ζ:

$$\ll [u(x+L) - u(x)]^2 \gg \propto u_c^2 \left(\frac{L}{L_c}\right)^{2\zeta} \tag{2.24}$$

where u_c is a transverse scaling parameter. Assuming parameter scaling law for the displacements from Eq. 2.24, $u(L) \propto u_c(L/L_c)^{\zeta}$, the typical energy barrier E then scales as $E(L) \propto U_c(L/L_c)^{2\zeta-1}$ where U_c is scaling energy constant. Then the free energy becomes:

$$F(u,L) = U_c(L/L_c)^{2\zeta-1} - 2M_s H t_{film} L_c u_c \left(\frac{L}{L_c}\right)^{\zeta+1} \tag{2.25}$$

The first term tends to reduce L while the second term tends to increase. The minimization of Eq. 2.25 with respect to L gives the optimal length $L_{opt} \approx L_c(H_c/H)^{\frac{1}{2-\zeta}}$ to overcome the energy barrier. The energy barrier here can be written as:

$$\Delta E_B = k_B T_d \left[\left(\frac{H}{H_{dep}}\right)^{-\mu}\right] \tag{2.26}$$

where H_{dep} is the depinning threshold magnetic field, μ is the creep exponent and T_d is the depinning temperature. From the Eq.2.25 and Eq. 2.26, the scaling relation between ζ and μ is generalized for any dimension d:

$$\mu = \frac{d + 2\zeta - 2}{2 - \zeta} \tag{2.27}$$

In the case where $1d$ DW surface in 2D media can be expressed as $\mu = (2\zeta - 1)/(2 - \zeta)$. Since DW velocity in the creep regime ($H < H_{dep}$) is following an Arrhenius law, DW velocity regarding the energy barrier ΔE_B is given by [69]:

$$v \propto exp\left(-\frac{\Delta E_B}{k_B T}\right) = exp\left[-\frac{U_c}{k_B T}\left(\frac{H}{H_{dep}}\right)^{-\mu}\right] \quad 2.28$$

In the work of P. Chauve [73], domain wall velocity is also derived as:

$$v = v_0 \exp\left[-\left(\frac{T_d}{T}\right)\left(\frac{H}{H_{dep}}\right)^{-\mu}\right] = v_0 \exp\left[-\frac{U_c}{k_B T}\left(\frac{H}{H_{dep}}\right)^{-\mu}\right] \quad 2.29$$

where v_0 is a numerical prefactor. This expression is valid where $H \ll H_{dep}$. Mostly, FM thin films with PMA have $\mu = 1/4$ [74].

Above the Creep regime, a thermally-assisted flux flow regime (between the creep regime and the depinning regime in Figure 2-8a) and the flow regime is followed. However, since we don't reach the driving force (magnetic field) to the flow regime in this system, we do not show theoretical backgrounds in these regimes.

2. 5. Voltage control magnetism

Voltage control magnetism in ferromagnetic metal films is a promising technology for the designing of low-power consumption memory devices. The electric field effect on magnetic can be due to several effects. One is coming from the charge accumulation/depletion effect on the surface of the ferromagnetic material or an ion migration effect. In this part, the electric field effect will be described based on these effects.

2. 5. 1. Charge accumulation/depletion effect

After the observation of the magnetic phase transition from ferromagnetic to paramagnetic upon application of the electric field [2], voltage-controlled magnetization started to be investigated in various ways [2], [75], [76]. The mechanism of the electric field effect can be divided into two materials. In the case of the ferromagnetic semiconductors, the magnetism is mediated by the presence of a hole (h^+) carrier upon application of the electric field [77], [78]. Therefore, the variation of the hole concentration upon the application of the electric field results in the variation of the ferromagnetic exchange interaction. However, in ferromagnetic metals, magnetic moments and the charge carriers are non-localized. Furthermore, the charge carrier density is higher than ferromagnetic semiconductors, therefore it has a relatively large screening of the electric field effect. After observing the electric field effect in the coercive field in semiconductor material [79], the pioneering work of the M. Weisheit et al. opens the study of the electric field dependence of the magnetic anisotropy energy in ferromagnetic

metals [2]. In the work of M. Weisheit et al., the material's intrinsic magnetic properties are determined by unpaired d electrons with energies close to the Fermi level E_F.

2. 5. 2. Ion migration effect

There were various studies to enhance the electric field effect using high-k dielectric material or ionic solid or electrolyte [2], [14], [28], [42], [80]–[82]. Especially in the metal/oxide interface, interfacial chemistry is crucial which determines the electronic, chemical, and magnetic properties. In this sense, the voltage-controlled magneto-ionic effect is introduced to control magnetic properties by migrating oxygen ions in the oxide layer [83], [84]. The origin of this effect is based on the surface reduction and oxidation by migrated oxygen ions upon application of the electric field. Results of the magneto-ionic effect are shown in different ways: DW pinning [85], magnetic anisotropy, saturation magnetization [86], etc. The major challenge of the magneto-ionic effect upon application of the electric field is its reversibility. Since the electric field can drive oxygen deep into the ferromagnetic material, the magnetic property can't be recovered by reversing the electric field. The suggested mechanism of this irreversibility is proposed by the previous work [87]. In this mechanism, it describes that the applied electric field drives oxygen ion defects bound to the surface of the crystalline grain from an oxide layer to a ferromagnetic material. Then once oxygen defects react with a ferromagnetic material, the oxygen can't be back through reversing the electric field resulting in a permanent magnetic property change in the ferromagnetic layer.

2. 5. 3. Electric field effect in the magnetic anisotropy energy

The performance of the electric field effect on magnetic anisotropy can be defined by using β:

$$\beta = \frac{\Delta K_s}{\Delta E} \ [\mathrm{fJ/Vm}] \qquad 2.30$$

where E is the applied electric field and K_s is the surface anisotropy. In the case of accumulation/depletion induced electric field effect in Co and CoFeB layers, β has the range of $10\sim50$ $\mathrm{fJ/Vm}$ [42], [80], [84], [88]–[90]. In the case of the $\mathrm{HfO_2/MgO/Co/Pt}$ with the ion migration effect with a chemical process, it shows a very large β value as $\sim150\mathrm{fJ/Vm}$ [91]. As we can see in the Eq.2.30, β affects the surface anisotropy. Therefore, the total magnetic anisotropy (K_{MAE} or K_{eff}) from Eq. 2.8 can be re-written as:

$$K_{MAE}(\mathrm{V}) = K_V + \frac{K_S^{Total} + \beta E(\mathrm{V})}{d} \qquad 2.31$$

2. 6. *In situ* magnetic characterization

2. 6. 1. Principle of Magneto-Optical Kerr Effect (MOKE)

When light meets a material, light interacts with the material. There are two main effects that come from this interaction. When a polarized light penetrates through a material, the polarization of the incident light is changed which is known as the Faraday effect. The other one is a linear polarization state of incident light that is transformed into an elliptic light when the light is reflected from the surface of a magnetized material. This is called the Magneto-Optical Kerr Effect (MOKE). Microscopically, magneto-optic effects are caused by the spin-orbit interaction, which happens when the electrical field of light interacts with the electron spin within a magnetic medium. The antisymmetric, off-diagonal elements in the dielectric tensor, on the other hand, cause these magneto-optic effects macroscopically. Magneto-optical Kerr Effect is widely used in studying magnetic materials since MOKE measurement provides a non-destructive means to measure the magnetization of the thin film [92]. Details of the MOKE technique are found in various reviews [93], [94].

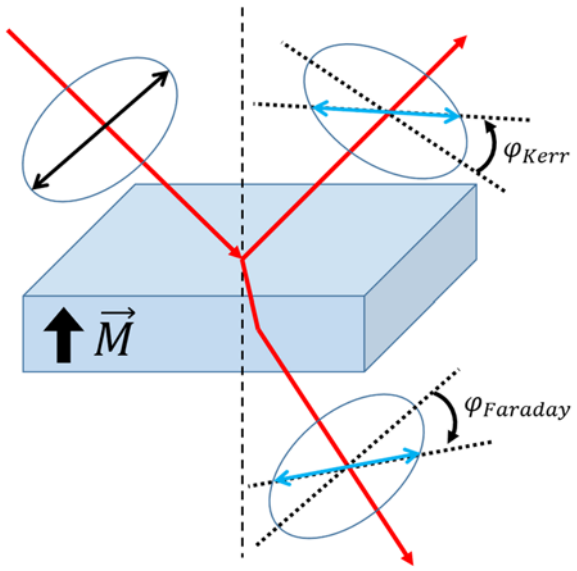

Figure 2-10 Scheme of the Faraday and Kerr effects. A plane-polarized incident light change after reflection/penetration resulting in Kerr rotation angle (φ_{Kerr}) and Faraday angle ($\varphi_{Faraday}$).

There are three different optical and magnetic geometries of the Kerr effect: longitudinal, transverse, and polar. In this thesis work, polar MOKE is used to obtain a magnetic state of the thin film. The polar MOKE has a magnetic field orientation parallel to the plane of incidence and normal to the sample surface. Plane polarized incident light becomes elliptically polarized with its major axis rotated from the initial incident polarization state after the reflection from the magnetized sample surface. The rotation angle of the major axis is known as Kerr rotation (φ_{Kerr} in Figure 2-10). In the case of ultrathin films, the Kerr rotation angle is proportional to the film total magnetization.

2. 6. 2. *In situ* PMOKE experimental setup

By using the principle of the PMOKE, a home-built *in situ* PMOKE setup is used to measure magnetic properties. Figure 2-11 shows the scheme of the *in situ* PMOKE setup. The sample is mounted not only for the air condition but also for the electrochemical flow mounting system (see Figure 2-13).

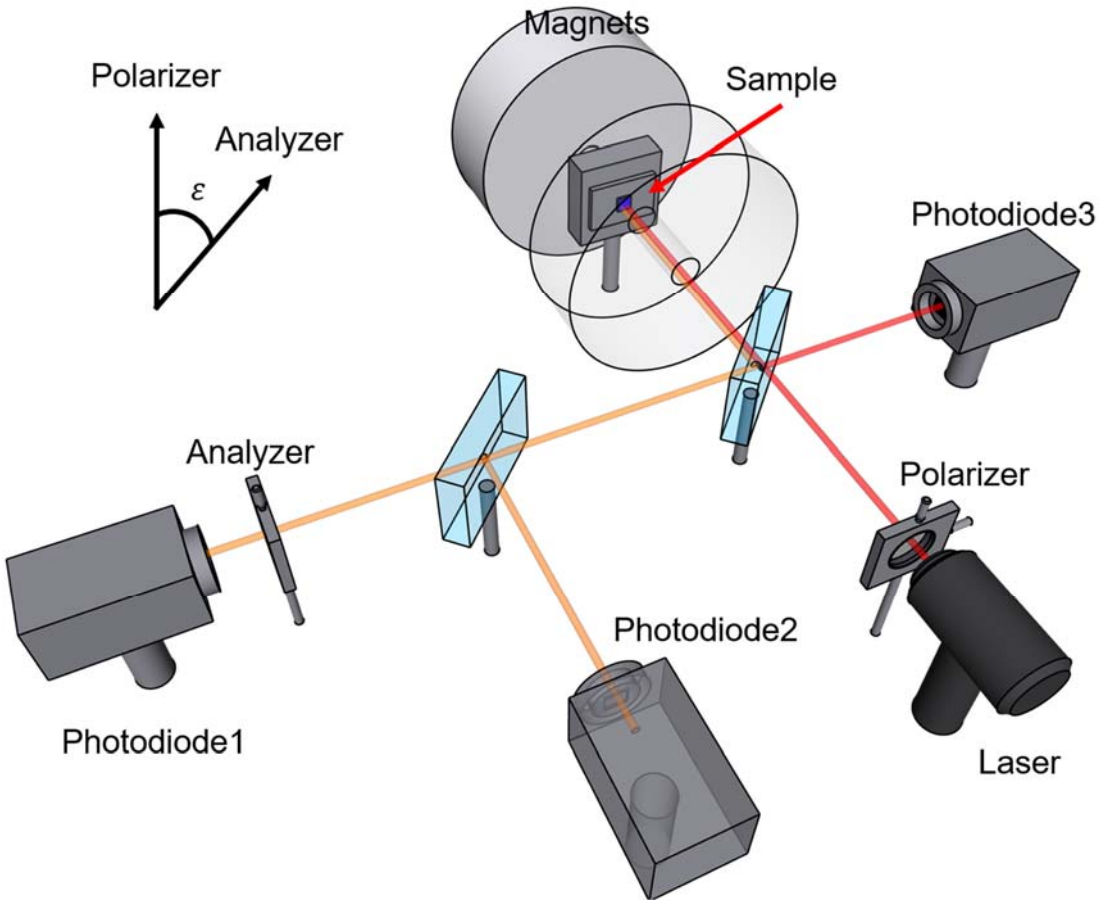

Figure 2-11 Scheme of the *in situ* PMOKE setup.

The initial laser (I_0, measured by photodiode 3) which is generated by the source with a wavelength of $\lambda = 630$ nm goes through a vertical polarizer (see red laser line coming out from the Laser in Figure 2-11). The surface of a sample reflects this vertically polarized laser. The first beam splitter reflects this beam, which is then separated by the second splitter. One passes through the analyzer and makes angle ε with the incident polarized beam then goes into Photodiode 1 in Figure 2-11 to measure I_1. I_1 is proportional to the reflectivity ($|r_{ss}|^2$) and depends on the Kerr rotation angle (φ). The other goes into Photodiode 2 to measure the current I_2 which is proportional to the reflectivity ($|r_{ss}|^2$) [49]. These relations are expressed as:

$$I_1 \propto \frac{1}{2} I_0 |r_{ss}|^2 [(1 + cos2\varepsilon) + 2\varphi sin2\varepsilon] \quad 2.32$$

$$\boldsymbol{I_2 \propto I_0 |r_{ss}|^2} \quad 2.33$$

By dividing Eq. 2.32 with Eq.**2.33**, we obtain:

$$I = \frac{I_1}{I_2} \propto \frac{1}{2} [(1 + cos2\varepsilon) + 2\varphi sin2\varepsilon] \quad 2.34$$

In Eq. 2.34, we set $\varepsilon = 83.5°$ [13]. Intensity (I) depends on φ and doesn't depend on the reflectivity anymore. Therefore, any changes in the sample reflectivity are cancelled out.

In situ PMOKE experimental setup is to measure the hysteresis loop by applying the magnetic field back and forth using electromagnets (see magnets in Figure 2-11). Magnetic hysteresis acquisition rate varies (1M-H / 2M-H) cycles per second depending on interest.

a. Electrochemical cell preparation

In the case of the sample which is prepared by the collaborator (we call it a sputter-deposited sample), the ferromagnetic layer (Co) is passivated by the oxide layer (AlOx or MgO). Therefore, a sputter-deposited sample should be treated to connect electrically the working electrode (WE) at the sample edge. This work is done by eliminating the passivation layer and Co layer.

Firstly, several drops of the electrolyte having pH 1 (0.1M H_2SO_4) are done by using the micropipette on the side of the sample. After 10~20 minutes, these drops are rinsed using distilled water. Then, this sample is placed on the support as shown in Figure 2-12 middle picture to connect WE (Cu plate) using aluminum foil. The cross-section of the connection is shown on the right of the scheme.

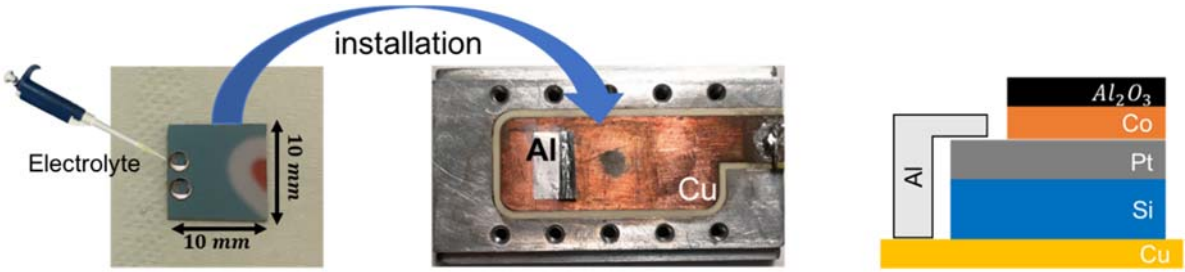

Figure 2-12 Preparation of the sputter-deposited sample for the electrochemical flow mounting system

After that, the electrochemical flow system is assembled using other compartments. Figure 2-13 shows the scheme of the electrochemical flow system after mounting the sample. This system has a dimension of $40\text{mm} \times 22\text{mm}$. The electrolyte thickness is $\sim$ 5mm and the volume of this cell is around 1ml. The electrolyte flows through the inlet by gravitational force and is pumped through the outlet by a peristaltic pump with a flux of $\sim 1.0\text{mL/min}$. As a result, the electrolyte inside of the cell is maintained at the same composition even though there is some reaction between the electrolyte and the sample.

In addition to the working electrode (WE) as we indicated in Figure 2-12, Pt wires (red lines in Figure 2-13) are used as counter electrodes (CE). The reference electrode is the mercury-mercurous sulfate electrode (MSE, $E = +0.64V$ in saturated K_2SO_4) and is connected to the cell with a tube filled with $0.1M$ K_2SO_4. The potentiostat provides target potentials to electrodes.

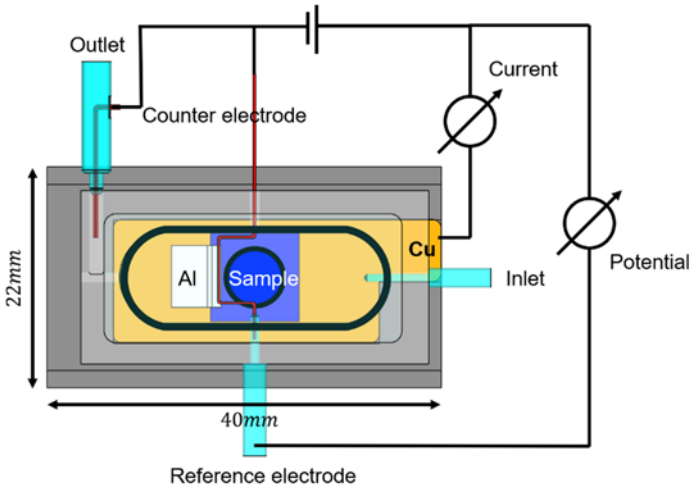

Figure 2-13 Scheme of the electrochemical flow system with the potentiostat connection diagram

2. 6. 3. MOKE microscopy

MOKE microscopy is a technology that uses spatially resolved information to measure magnetic characteristics, i.e. magnetic domains are observed by MOKE microscopy. The spatial information is obtained by using the charge-coupled device (CCD) camera [95].

Figure 2-14 shows the MOKE microscopy setup. The laser passes through the polarizer which induces linear polarization. Linearly polarized light passes through a beam splitter which makes normal incidence on the sample surface. After being reflected from the magnetized sample surface (Kerr rotation takes place), the laser passes the beam splitter again and is collected by a CCD camera behind the analyzer. As compared with the *in situ* PMOKE setup, it contains two electromagnets: BC (i.e. Big Coil) allows to apply large enough magnetic fields ($> 100\mathrm{mT}$) to saturate the sample. This electromagnet is rotatable to apply an in-plane magnetic field. SC (i.e. Small Coil), attached to the cell holder, can apply a relatively small magnetic field (up to ~50mT).

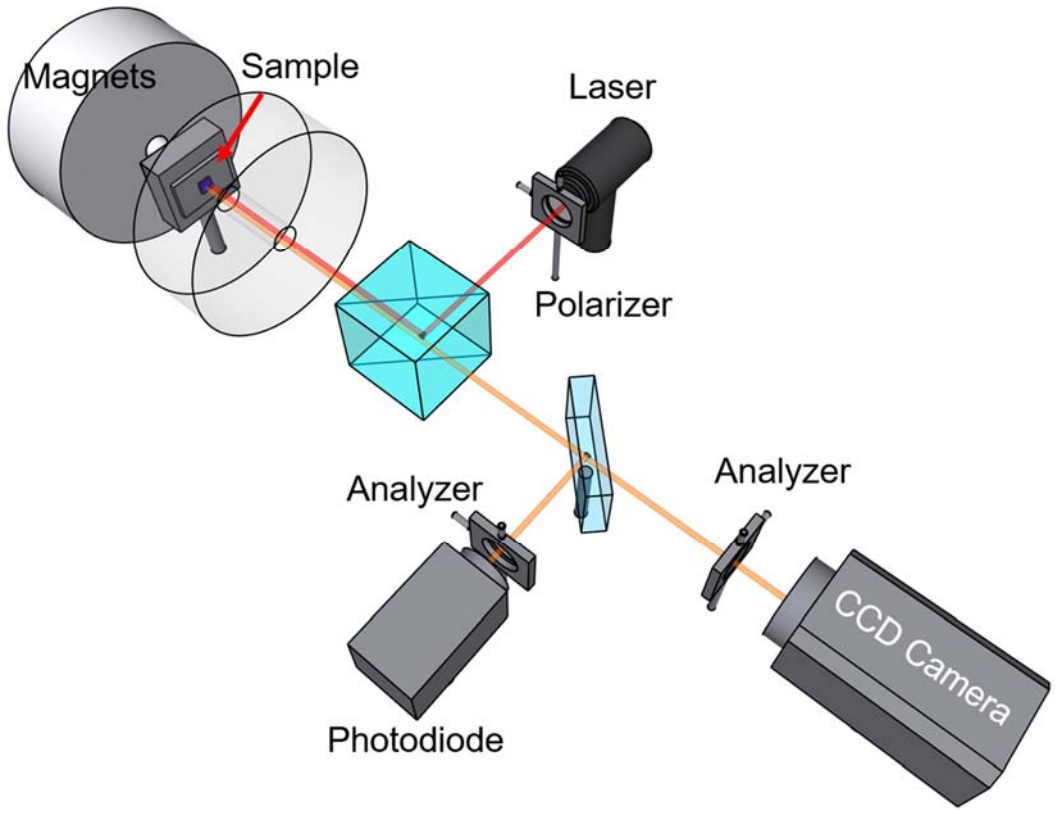

Figure 2-14 *In situ* MOKE microscopy setup

To observe the magnetic domain wall propagation, it requires several steps described in Figure 2-15. Ferromagnetic layer at the initial state has a random-oriented spin state (Step.1 in Figure 2-15a). Then the relatively high intensity of the magnetic field induces saturation (H_{sat}), i.e. alignment of all spins along the magnetic field (Step 2). A magnetic field with the opposite direction is applied to nucleate magnetic domains (Step 3). By applying a lower magnetic field than the nucleation field (H_{nuc}), magnetic domain wall propagation is observed.

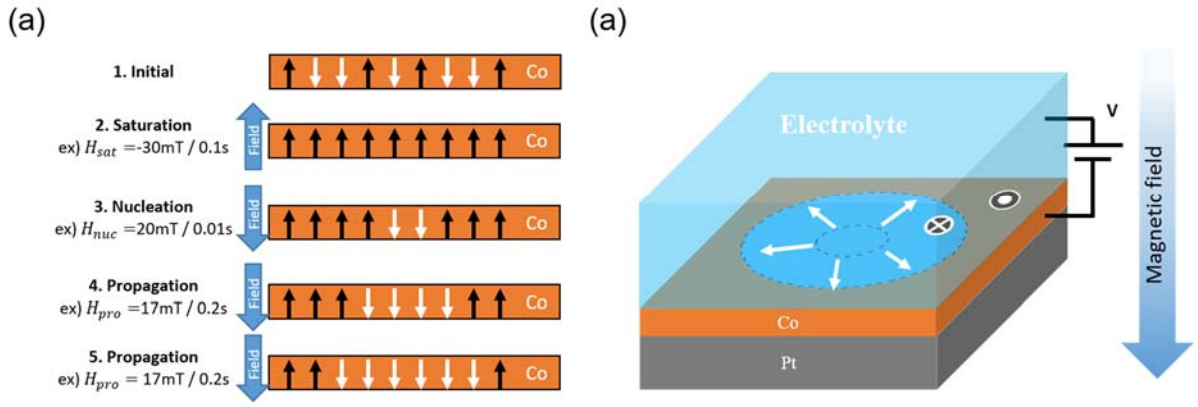

Figure 2-15 (a) Magnetic domain wall propagation procedure and (b) *in situ* MOKE microscopy interface

Chapter 3. Electrodeposition of Co on Pt substrate and influence of hydrogen evolution on the magnetic properties

3. 1. Introduction

As an alternative method to deposit a magnetic thin film layer with the molecular beam epitaxy (MBE), the electrodeposition of the magnetic thin film has been studied for decades because of its cost and convenience [96]–[98]. The principle of the electrodeposition is described in Chapter 2. 2 as well as in the work of P. Allongue et al [99]. Briefly, Electrodeposition is promoting the reduction of the target cations ($A^{z+} + ze^- \rightarrow A$) at the electrode surface by applying more negative than Nernst potential of the redox couple (A^{z+}/A). Experimentally, various kinds of magnetic materials such as Ni, Fe, and Co thin films have been investigated with the electrodeposition on Au(111), Ag(111) substrates [100]–[102] as well as on Pt substrate [98], [103], [104]. In the case of the thin magnetic material, neighbor layers in contact with the magnetic material have a crucial influence on the magnetic properties. As already described in Eq. 2.8, surface anisotropy $K_s = K_s^{down} + K_s^{up}$ determines perpendicular magnetic anisotropy (PMA) through the hybridization (e.g. spin orbital coupling) in the ultrathin film. In the case of Co layers which will be discussed throughout the thesis, when deposited on Au(111) substrate, their magnetic properties vary with the capping layer [49], [100], [105], [106]. For instance, spin reorientation transition thickness (d^*, see Chapter 2. 1) varies since K_s varies with the chemical nature of the capping layer on top of the Co. In addition, surface chemistry tailoring with adsorbates also changes magnetic anisotropy energy as well as the electric field effect [13], [14], [41], [107], [108]. Gaseous adsorption on the surface mostly induces PMA by reducing the absolute value of K_s which favors in-plane magnetization [107]. D. Matsumura et al. showed SRT of Co/Pd(111) by inducing CO adsorption by XMCD and XPS [109], [110]. In the case of the electrodeposited Co on Au(111), N. Tournerie et al. investigated with the *in situ* MOKE measurement that the surface magnetic anisotropy energy is largely enhanced (around a factor of 4) after CO adsorption [14]. In addition to that, CO adsorption induces enhancement of electric field effect compared to the H adsorption on the Co/Au(111) films (from $(\Delta H_c/H_c^0)/\Delta U = -45\%/\mathrm{V}$ to $-60\%/\mathrm{V}$) [13]. Even though previous studies on Co on Au or Pd substrates have progressed, studies Co on Pt still have a long way to go.

In this chapter, electrodeposition of Co on Pt will be optimized and performed aiming for having PMA after adsorption of CO layer while monitoring magnetic properties through *in-situ* PMOKE measurement. Then, hydrogen evolution reaction (HER) pulses are systematically applied on the electrodeposited Co film on Pt substrate since irreversible variations of magnetic properties occur when the applied potential is in the potential of HER ($U < -1.0V$). Additionally, HER pulses are applied on bare Pt covered with CO to understand the origin of the HER effects.

3. 2. Electrodeposition of Co layers on Pt substrate

Electrodeposition of Cobalt (Co) on $Si(111)/SiO_x/Ta(3nm)/Pt(3nm)$ substrate is done in the solution of composition 1 to 5mM $CoCl_2$ in 0.1M K_2SO_4 + 1mM H_2SO_4 + 1mM KCl (pH 3.5). The substrate is prepared by dc magnetron sputtering on thermally oxidized silicon wafers from Spintec (Grenoble, France). Figure 3-1a shows a voltammogram (CV) measured in a 2mM $CoCl_2$ solution (top panel, black line). Applied potential (U) is swept from -0.2 V to -1.4V, then back to -0.2 V at a sweep rate of $10mV/s$ (Red arrows indicate sweep direction). Figure 3-1b shows the corresponding variations of the sample relative reflectivity $\Delta R/R_0$ during CV (R_0 : initial value is measured at -0.2 V). R is the sample reflectivity divided by laser intensity to eliminate laser instability. The derivative of R with respect to time is plotted in Figure 3-1a (red curve). During the potential sweep, different electrochemical reactions take place as indicated by the cathodic waves C1 to C3 and anodic waves A1 and A2 [49] but only some of them are visible in $\frac{dR}{dt}(U)$. The cathodic wave (C1) at $U \sim -0.8V$ corresponds to the hydrogen evolution reaction (reduction of protons, see Eq.3.1) and is associated with a weak change in reflectivity. When the applied potential is negative of $U \sim -1.05V$, Co^{2+} reduction starts (C2) and metallic Co is deposited on the Pt surface (See Eq.**3**.**2**). This process is associated with a steep increase of $\Delta R/R_0$. One remarks however that Co deposition nearly stops when water starts to decompose ($U < -1.3V$**,** wave C3, Eq. **3**.**3**). This has been reported by others [111] and is plausibly due to a local pH increase inducing the formation of Co hydroxide species. On the positive-going sweep, as soon as water decomposition stops, Co deposition re-starts but then stops around $-1V$. The anodic peak (A1) around $U \sim -0.85V$ corresponds to the Co dissolution of metallic cobalt (reverse reaction of Eq. **3**.**2**). It is associated with a steep decrease of the sample reflectivity, which returns to its

initial value. The small anodic current wave (A2) at -0.75 V, which overlaps with wave (A1), corresponds to the reverse reaction of Eq. 3.1, i.e. H_2 oxidation. In fact, the derivative of R with respect to the time (red) highlights that Co dissolution is essentially complete above -0.8 V. Coupling the current trace and the derivative of the reflectivity is therefore useful to set the appropriate boundaries of potential for integrating the current and convert the electrochemical charge into an equivalent Co thickness.

$$2H^+ + 2e^- \leftrightarrow H_2\ (g) \qquad 3.1$$

$$\mathbf{Co^{2+} + 2e^- \leftrightarrow Co} \qquad 3.2$$

$$\mathbf{2H_2O \rightarrow H_2\ (g) + 2OH^-} \qquad 3.3$$

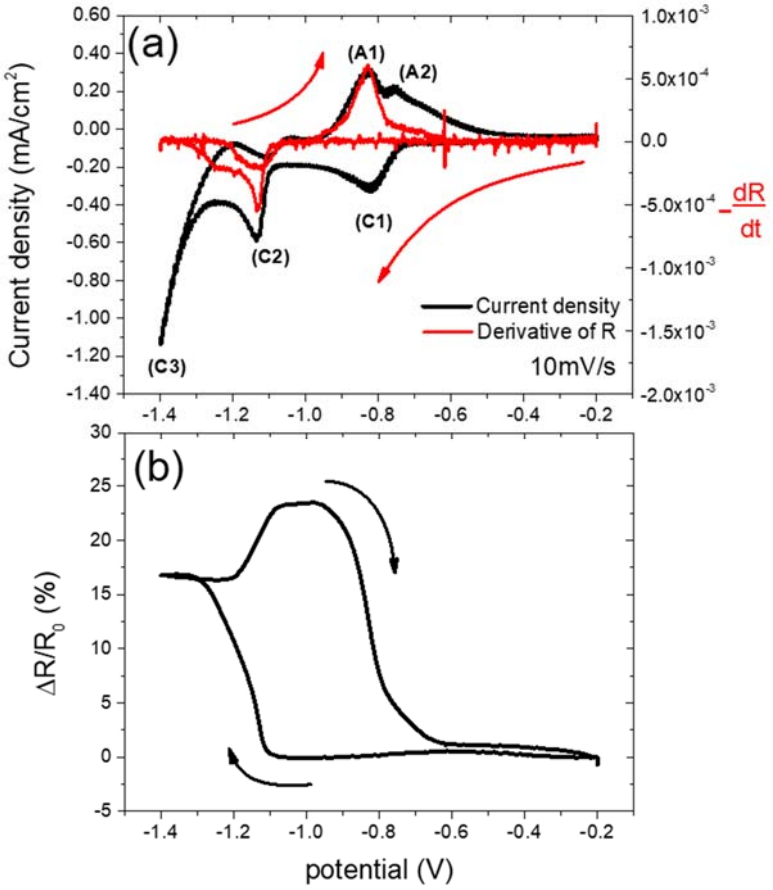

Figure 3-1 (a) Deposition current-voltage (CV) curve in the $2mM\ CoCl_2$ standard solution (pH 3.5) on Pt 3/Ta 3/SiOx/Si (numbers are thickness in nm) substrate (black) with the derivative of R with respect to time (red). Arrows indicate the direction of potential sweep with the rate of $10mV/s$. Featured electrochemical reactions during the potential sweep are marked as C1~C3 and A1~A2. (b) Corresponding variation of the sample relative reflectivity $\Delta R/R_0$.

3. 3. Magnetic properties of electrodeposited Co/Pt layers

Electrodeposition of cobalt is performed by applying a constant potential (U_{dep}) to control the nucleation stage. U_{dep} is chosen in the range from $-1.1\mathrm{V}$ to $-1.25\mathrm{V}$ from Figure 3-1.

Figure 3-2a shows current density (black line) and applied potential (blue line) as a function of time during the Co deposition and dissolution. Figure 3-2b shows the relative reflectivity $\Delta R/R_0$ (black line) and the derivative of R as a function of time. R_0 is the initial reflectivity before deposition of Co (i.e. the reflectivity of the substrate with the applied potential $-0.2\mathrm{V}$). Co deposition/stripping procedure is composed of three phases as indicated in Figure 3-2a (i)~(iii) separated with red arrows. Before Co deposition begins, constant potential $-0.2\mathrm{V}$ is applied for 5 seconds. The light gray shaded region (i) corresponds to the deposition: The potential is stepped from $-0.2\mathrm{V}$ to $U_{dep} = -1.2\mathrm{V}$ for a deposition time (t_{dep}). During this phase, $\Delta R/R_0$ increases as shown in Figure 3-2b. (ii) Then, applied potential is switched to $-1.02\mathrm{V}$ to stabilize the deposited layer (in this time range, $\Delta R/R_0$ remains constant). The dark gray shaded region corresponds to the Co dissolution phase (iii): A ramp of potential ramp between -1.02 V and -0.2V is applied to dissolve the Co layer (sweep rate 10mV/s). The anodic current is accompanied by a drop of $\Delta R/R_0$. The derivative of R (red dots in Figure 3-2b) clarifies the onset of the Co dissolution. The dissolution potential ramp is used to estimate the thickness of deposited Co layer (see below). In addition, Figure 3-2c shows magnetization at the maximum field (black) with the remanence (red) derived from magnetic hysteresis recorded at a rate of $1\ \mathrm{plot/s}$ during the deposition-dissolution procedure. Magnetization plots are given in inset at selected times during the procedure.

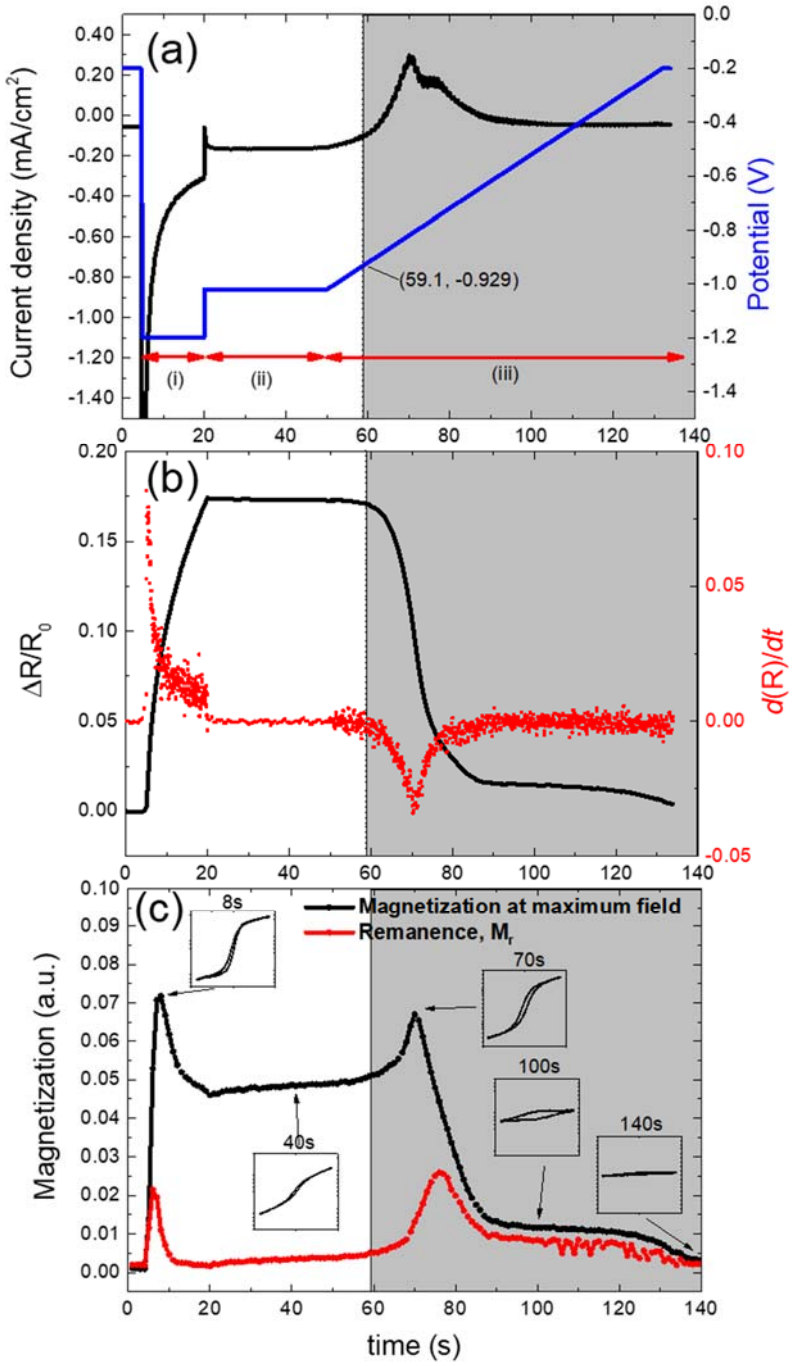

Figure 3-2 (a) Applied potential variation (blue line) and measured current density (black) as a function of the time during the Co deposit-dissolution step. Each step is indicated as (i) deposition (ii) stabilization (iii) dissolution with red arrows. (b) Corresponding relative reflectivity (black, $\Delta R/R_0$) with its derivative (red, $\frac{d(\Delta R/R_0)}{dt}$). (c) Magnetization at the maximum field (black) and the remanence (red) from magnetic hysteresis. Insets show magnetic hysteresis at each point. The Gray region is selected dissolution range regarding optical variation.

a. Variation of the deposition time (t_{dep}) and the estimation of Co thickness

To establish a relation between deposition time (t_{dep}) and Co thickness (d_{Co}), we deposit/dissolve Co layer for increasing t_{dep}. The procedure is that described in the previous section. The solution used in the experiment is $2\text{mM } CoCl_2 + 0.1\text{M } K_2SO_4 + 1\text{mM } H_2SO_4 + 1\text{mM KCl}$ and $U_{dep} = -1.2\text{V}$ (before deposition $U = -0.2\text{V}$). Figure 3-3a shows reflectivity variations ($\Delta R/R_0$) during the deposition and stabilization (at -1.02 V) phases. The three plots correspond to t_{dep} = 4s, 8s, and 12s. Figure 3-3b shows corresponding variations of the magnetization at the maximum field (symbols) with the remanence (lines). Figure 3-3c shows the variations of the coercive field as a function of time. Magnetic parameters are derived from magnetization plots (recorded at a rate of 1 plot/s).

As we can see in Figure 3-3, deposition is very reproducible since all plots overlay well in their common time intervals. For the longest deposition time, the magnetization at the maximum field goes through a maximum around 7s of deposition. Similar behavior was observed upon Co deposition on Au(111) [41]: It indicates that the magnetization of the sample starts to orient towards the in-plane direction when the Co thickness increases. The phenomenon is known as spin reorientation transition (SRT). This is also visible on magnetization plots after deposition in the inset of Figure 3-3a, which becomes more reversible as the Co layer grows.

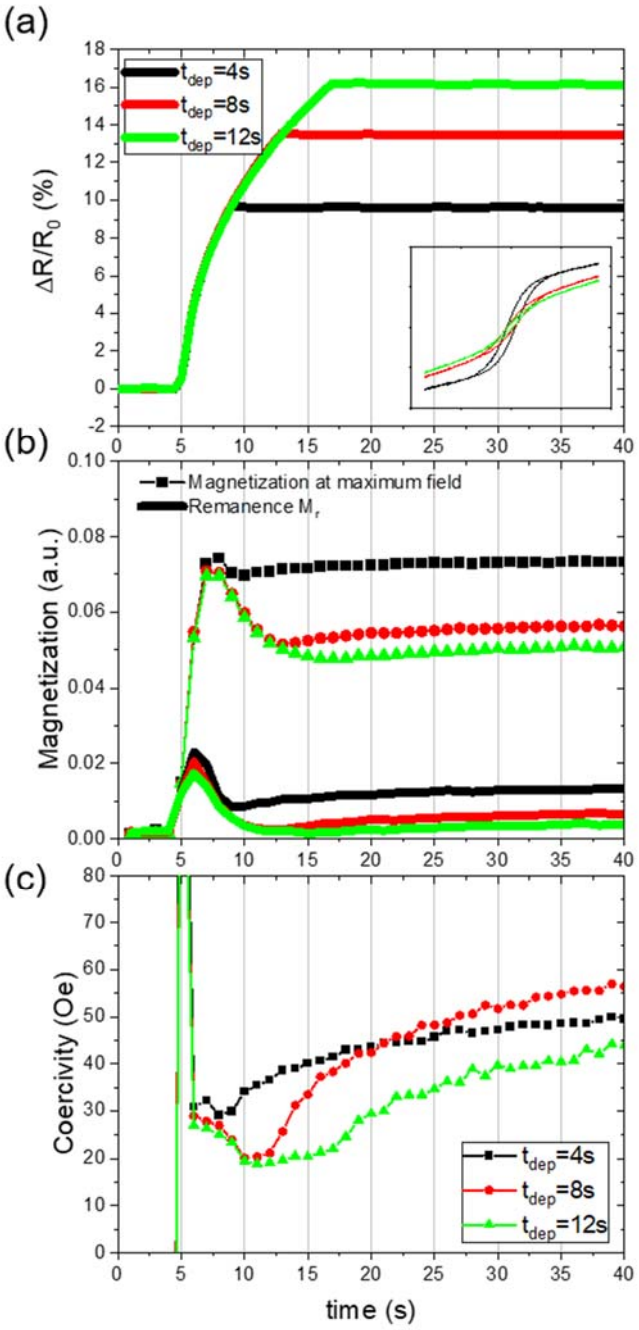

Figure 3-3 (a) Relative reflectivity ($\Delta R/R_0$) with respect to its initial value as a function of time in different deposition times (t_{dep}). Inset shows hysteresis variation at 40s. (b) Magnetization at the maximum field (symbol) with the remanence (simple line) and (c) coercive field variations derived from magnetic hysteresis. The solution used in the experiment is 2mM $CoCl_2$ + pH 3.5 solution. Deposition of Co is achieved by applying potential as $U_{dep} = -1.2$V. R_{max} is the reflectivity where the deposition is stopped.

To estimate the thickness of the Co layer one cannot use the cathodic current because the reduction of protons occurs in parallel to Co deposition (Reaction 3.1). With some precaution, one may use the dissolution current. The difficulty, is indeed that two anodic waves are measured during the stripping phase. These correspond to waves A1 and A2 in the CV of Figure 3-1a. Figure 3-4a shows one example how one may safely estimate the Co thickness. All substrates used in this experiment are Pt 3nm/Ta 3nm/SiO_x/Si and the base electrolyte is 0.1M K_2SO_4 + 1mM H_2SO_4 + 1mM KCl solution. The red line in Figure 3-4a is the voltammogram of the Pt electrode between 0V and −1V (10mV/s) with no $CoCl_2$ in the electrolyte. The two waves correspond to H^+ reduction (at ∼ − 0.75V) and to oxidation of H_2 (at −0.9V). The black line shows the dissolution phase after Co deposition (U_{dep} = −1.2 V, 5s, 2mM $CoCl_2$). The sweep rate is the same as for the CV (10 mV/s). The green line shows corresponding relative reflectivity variation with respect to its initial reflectivity (substrate) while the Co is dissolving (see right y-axis). Arrows in color are directions of the potential sweep.

The gray shaded region in Figure 3-4a corresponds to the actual charge associated with Co dissolution. The remaining charge, mainly under peak A2 is related to hydrogen oxidation. In this example, the gray area corresponds to a charge of 1.76 mC/cm^2. Therefore, the estimated Co thickness is 2.98 ML with the corresponding total relative reflectivity change as $\Delta R_{max}/R_0$ ∼ 11%. Repeating this procedure for different deposition times allow plotting in Figure 3-4b the correlation between the Co thickness and $\Delta R_{max}/R_0$. This figure shows that reflectivity is essentially linear with the thickness of Co. The offset of the linear-fitted curve (red line) may be due to an overestimation of the reflectivity since the reflectivity remains ~2% right after Co dissolution (see the reflectivity ~ -0.6V in Figure 3-4a). The remained reflectivity returns to 0% when the applied potential is more positive than −0.2V along with the disappearance of the magnetic signal (see Appendix 3. 6). This may arise from the alloy between Co-Pt.

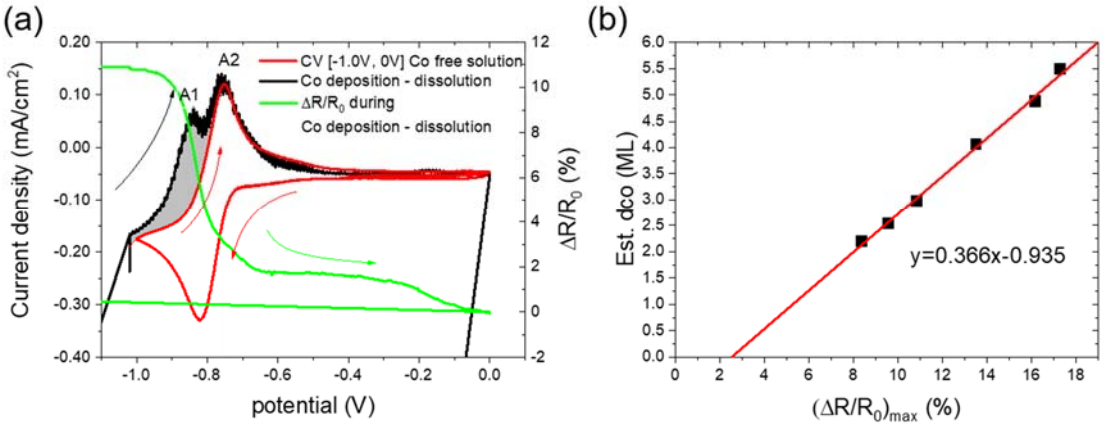

Figure 3-4 (a) Cyclic voltammetry (CV) by sweeping potential from 0V to -1V then back to 0V with the sweep rate of 10mV/s (red line and arrows in the same color show direction of the sweep). The black line shows one example of Co deposition/dissolution current density variation as a function of applied potential. The green line shows corresponding relative reflectivity with respect to initial reflectivity ($\Delta R/R_0$, green line with right y-axis). The Gray region is the region of interest to evaluate deposited Co thickness. (b) The estimated thickness of Co as a function of $\Delta R_{max}/R_0$. R_{max} is the reflectivity where the deposition is stopped.

b. Influence of CO post adsorption on magnetic properties

We describe below a procedure to adsorb CO on a deposited Co layer. As explained above, the deposition may be stopped by applying a potential of -1.02V (see Figure 3-2) where no deposition or dissolution occurs. The deposit is said stabilized. Keeping the sample at this potential, one may exchange the electrolyte (used for deposition) with a CO saturated solution that does not contain Co^{2+} cations ($0.1M\ K_2SO_4 + 1mM\ H_2SO_4 + 1mM\ KCl$). The reflectivity is monitored to check that no Co dissolution occurs. At the end of the procedure, a monolayer of CO covers the Co layer.

Figure 3-5a shows applied potential (black line) and the corresponding current density (red line) during the procedure. The cobalt layer was deposited in a 2mM $CoCl_2$ solution with $U_{dep} = -1.2V$ for 4s. The next two panels show the corresponding time dependence of magnetization at the maximum field with the remanence (Figure 3-5b, black and red respectively), and coercive field (Figure 3-5c). The inset of Figure 3-5c shows the hysteresis loop before (black) and after CO adsorption (red).

As we can see in Figure 3-5b and Figure 3-5c, the introduction of the CO saturated solution promotes progressive modification of the Co magnetic state. Initially, the magnetization easy

axis is in-plane since H_c is nearly 0 and M_r/M_s is close to zero. Upon CO adsorption there is a progressive increase of M_s, M_r and H_c. A steady state is reached after 200s where the Co layer is perpendicularly magnetized since $M_s = M_r$. The coercive field H_c value saturates to ~ 320 Oe. Applying -0.8 V is useful here because no H_2 evolution takes place at this potential.

The above demonstrates that CO adsorption promotes a reorientation of the magnetization easy axis from in-plane to out-of-plane direction. The adsorption of CO enhances the MAE, as was observed for Co/Pd(111) layers in the UHV [112] and also with Co/Au(111) layers in the electrochemical environment [41] and Pd(111). When the applied potential is swept from -1.02V to -0.8V at a rate of 10mV/s, to minimize HER, the magnetic state stays essentially unchanged. There is only a small decrease of H_c from $\sim$320 Oe to $\sim$295 Oe. We will see that this decrease is real. Furthermore, one sees that the Co layer is stable at -0.8 V after CO adsorption while bare Co layer starts dissolving at -0.9V as we can see in Figure 3-1a and Figure 3-2a. The presence of the CO monolayer is able to protect the sample from dissolution in agreement with previous studies of Co layers electrodeposited on Au(111) [41]. The effect is not a simple barrier effect (the CO molecule is too small) but rather stems from a modification of the redox properties of the cobalt at its surface.

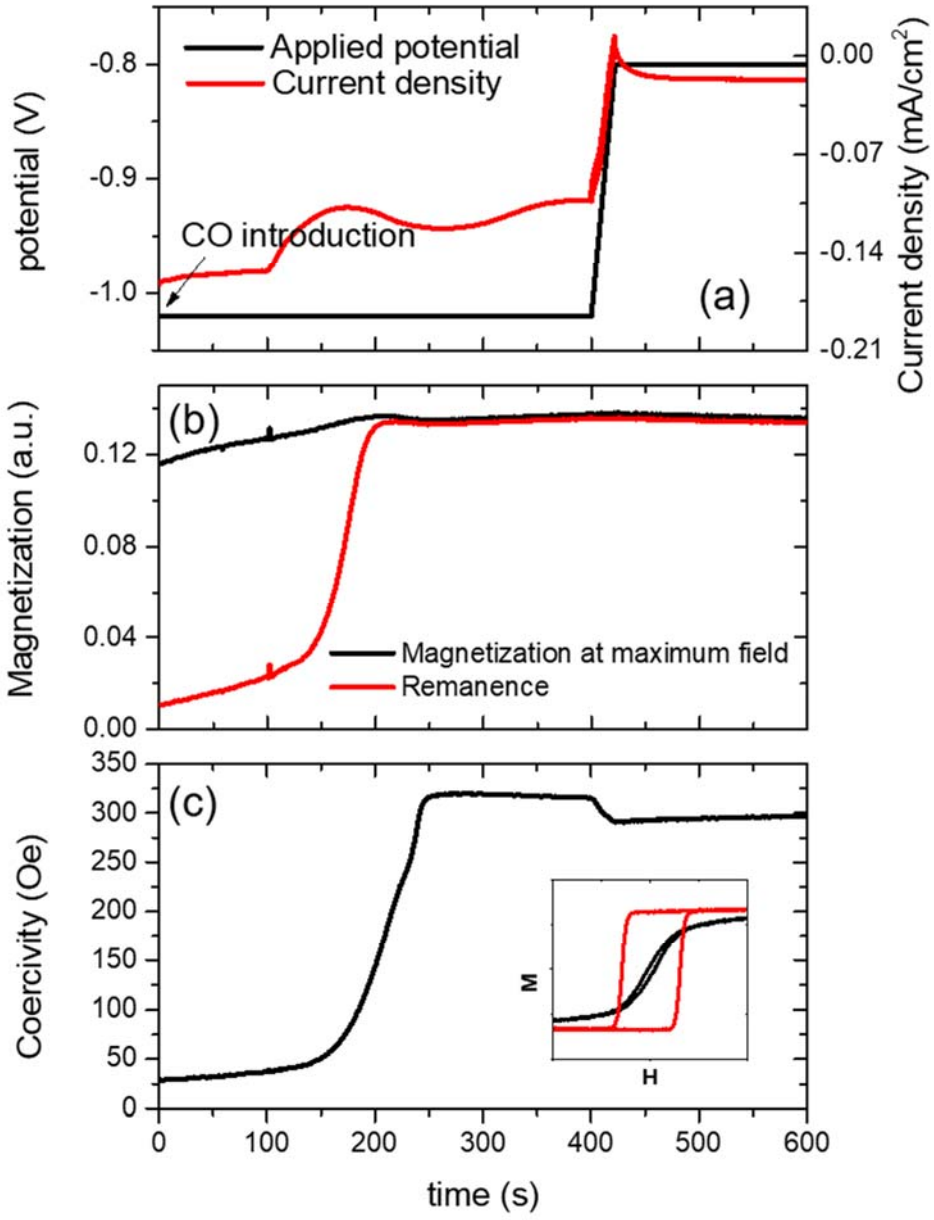

Figure 3-5 (a) Applied potential (black line) and current density variation (red line) after replacing the deposition solution with carbon monoxide (CO) saturated $0.1\text{M } K_2SO_4 + 1\text{mM } H_2SO_4 + 1\text{mM KCl}$ solution. Applied potential is swept from -1.02V to -0.8V at a rate of 10mV/s at 400s. (b) Corresponding variations of magnetization at the maximum field (black) with the remanence (red, M_r) and (c) coercive field. Inset in (c) shows hysteresis variation from the initial state (black) to the final state (red).

3. 4. Potential dependence of magnetic properties of CO-covered Co/Pt layers:

In this section, the initial magnetic state of the sample is that measured after CO is fully adsorbed and the sample was stabilized at $U = -0.8\text{V}$ for around 30 minutes.

a. Influence of potential sweep in the range [-1V, -0.7 V]

In this potential range, the influence of HER is negligible since HER onset potential is -1.0 V on cobalt. Figure 3-6 shows the influence of sweeping the potential as -0.8V → -1.0V → -0.7V → -0.8V (10mV/s). Inset in the first panel shows the right part of the magnetization loop during this CV. A common color is used for the symbols on the CV and each plot (from -1.0V to -0.7V with the interval of 0.1V). The coercive field varies at a rate of -82 Oe/V. Panels (b) and (c) show corresponding relative variations $\Delta H_c/H_c^0$, with H_c^0 measured at -0.8 V and relative variation of saturation magnetization ($\Delta M_s/M_s^0$) respectively. The two magnetic parameters show quasi-linear and reversible (3 times) dependences on the applied potential. The slope $\Gamma = \frac{\Delta H_c/H_c}{\Delta U} = -0.30\ \text{V}^{-1}$. As discussed in the previous work [41], the linear dependence of $\Delta H_c/H_c^0$ with applied potential may be assigned to surface charging. In fact, the CO-dosed surface keeps the same chemical composition as no HER occurs. Only its surface charge is affected. The effect is also called electric field effect (EFE). The value $\Gamma = -0.30\ \text{V}^{-1}$ measured here is nearly consistent with the case of Co $\sim$0.8nm/Pd ($\Gamma \sim -0.25\text{V}^{-1}$) and Co $\sim$0.96nm/Au interface ($\Gamma \sim -0.4\text{V}^{-1}$) in the CO-saturated pH 3.5 solution [13], [14], [42].

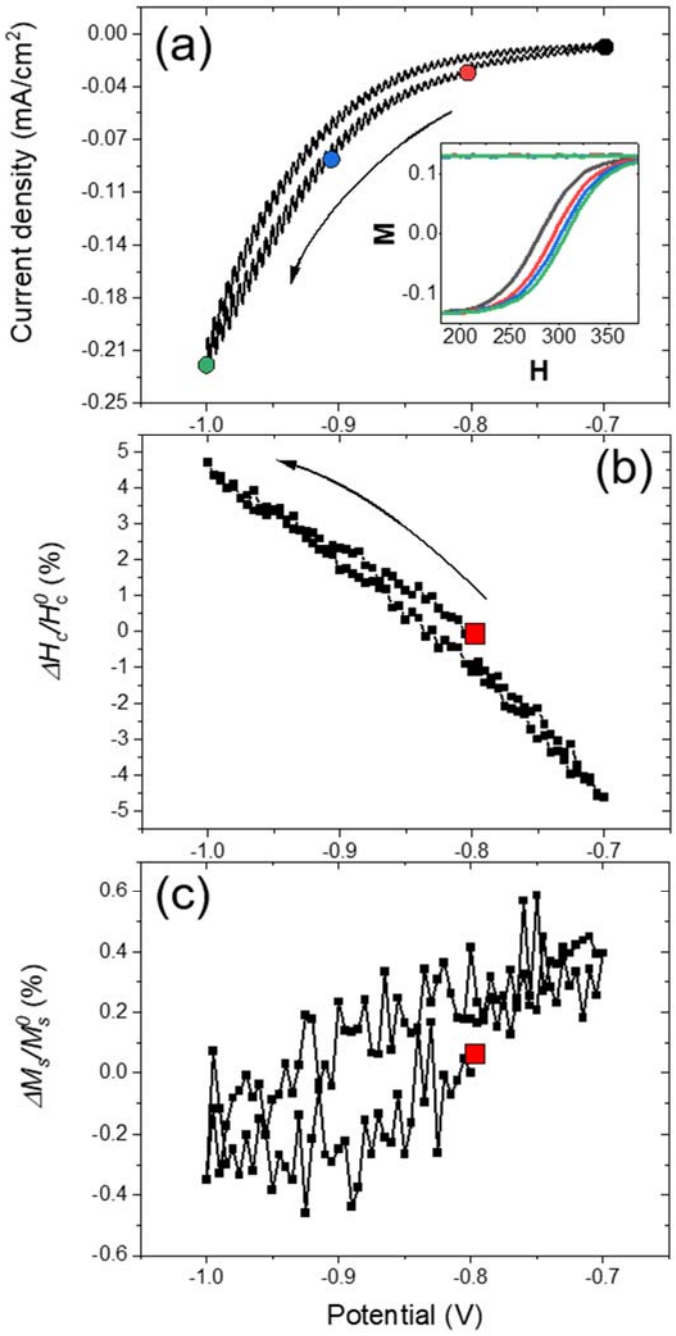

Figure 3-6 (a) Current density as a function of applied potential during the potential sweep $[-1.0\text{V}, -0.7\text{V}]$ with the sweep rate of 10mV/s. Inset of the first panel shows each hysteresis state marked with colors. (b) Relative variation of the coercive field with respect to the initial value ($\Delta H_c/H_c^0$) and (c) the relative saturation magnetization variation ($\Delta M_s/M_s^0$) during the potential sweep.

b. Influence of the application of potential pulses in HER regime.

To control the possible effect of HER on magnetic properties potential pulses were applied. Specifically, pulses (0.1 s long) are applied between $U = -0.8\text{V}$ (this is the rest potential of

the sample, where no HER occurs) and $U_{HER} < -1.0\text{V}$. Whenever consecutive pulses are applied, they are separated by an off time of 6s at -0.8 V.

Figure 3-7a shows the effect of applying 2 HER pulses at $U_{HER} = -1.5\text{V}$ (black) together with the measured current density (red line). The bottom panels show the corresponding variations of coercive field (Figure 3-7b) and the saturation and remanence magnetization (M_s,black line; M_r, red line in Figure 3-7c). The main observation is an irreversible decrease in H_c, M_s and M_r after application of pulses while M_r/M_s stays ~1. In other words, the easy axis of the sample remains out of the plane.

Looking at the figure in more details evidences that the first H_c data point, i.e. measured right after the application of U_{HER}, is systematically higher with respect to that measured just before at -0.8 V. This is in not an artifact. We infer that the system *transiently* follows the trend observed in Figure 3-6, where H_c increases at potentials more negative than -0.8 V. Accounting for $H_C^0 = 284\ \text{Oe}$ at -0.8 V, measured before the pulse, and for the slope of $-82\ \text{Oe/V}$ measured in Figure 3-6b, H_c should be $\sim 340\ \text{Oe}$ at -1.5V. This is significantly larger than measured ($292\ \text{Oe}$): the discrepancy may be assigned to a competition between two effects during the pulse at U_{HER}, (an increase due to the electric field effect and a decrease due to HER effect) and the measurement protocol. During the 0.1 s HER pulse, H_c is expected to increase because of the electric field effect ($-82\ \text{Oe/V} * -0.7\text{V} = 56\ \text{Oe}$) and decrease because of the HER effect ($\sim 10\ \text{Oe}$). Thus the expected value if 330 Oe during the pulse. However, in this experiment, the acquisition time of one hysteresis loop is 0.5s. Therefore, the measured value of H_c ($292\ \text{Oe}$) is an average of the one at -0.8V during 0.4 s and that during the HER pulse of 0.1 s. Since the hysteresis loop acquisition time overlaps over the time before and after the pulse, we will use an average value of 279 Oe for H_c at -0.8V. We then obtain for H_c measured during the pulse $(330 * 0.1 + 279 * 0.4)/0.5 = 289$ which is very close to the measured $292\ \text{Oe}$.

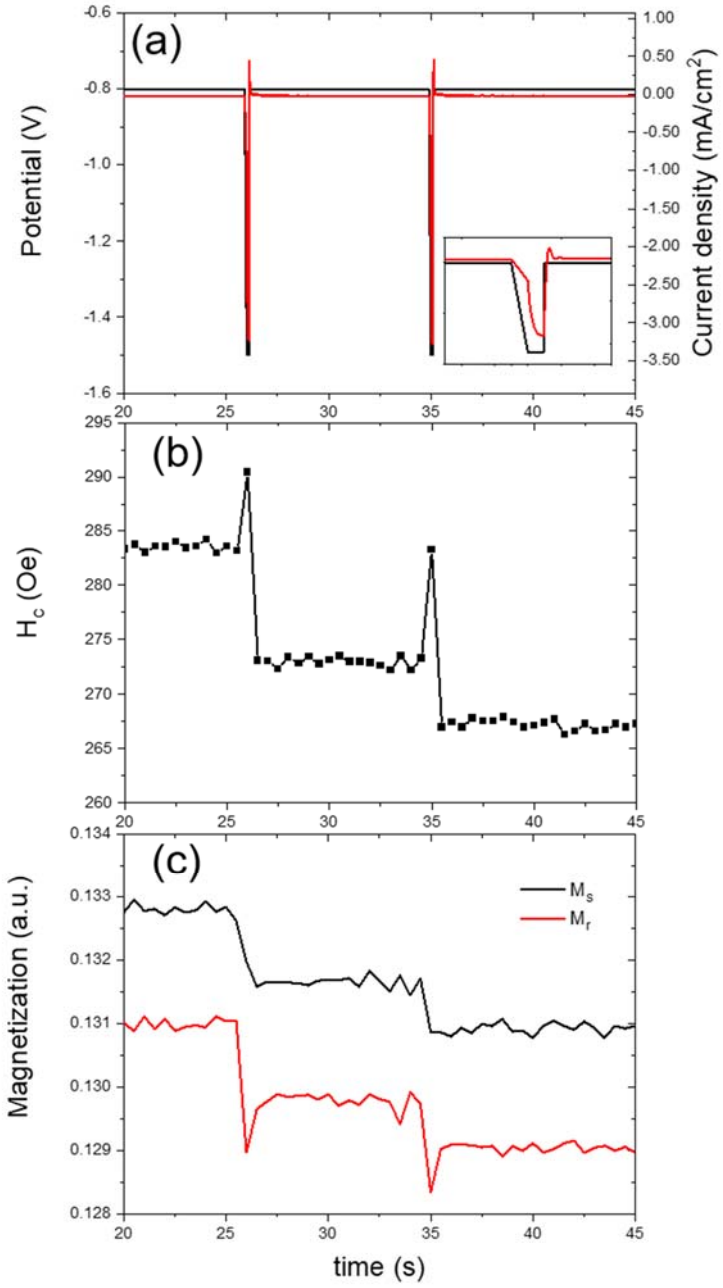

Figure 3-7 (a) Potential profile (black line) and induced current density (red line) by applying 2 hydrogen evolution reaction pulses ($U_{HER} = -1.5$V) for 0.1 seconds. Inset shows magnified potential pulse and current density variations during the pulse. (b) Corresponding coercive field (H_c), (c) saturation magnetization and remanence variations as a function of time derived from hysteresis.

The measurements of Figure 3-7a were repeated with different pulse amplitudes (U_{dep}), each time using freshly electrodeposited Co layers of a comparable thickness. The initial magnetic

parameters right after CO adsorption are listed in Table 3-1. Estimated thicknesses of Co are obtained by using linear relation from Figure 3-4b. Figure 3-9a-d solid lines show the hysteresis curves of the Co layer at -0.8 V after CO adsorption and before application of any potential pulses. These plots show that all Co layers covered with CO monolayer are perpendicularly magnetized ($M_r/M_s \sim 1$) and that all layers have similar thicknesses since M_s values are close to each other. Upon application of HER pulses (as indicated in the different panels) the magnetic hysteresis plot changes. Dash lines are the intermediate state and dotted lines are the final state of each sample (the number of pulses is indicated in each legend). As we can see through hysteresis variations upon HER pulse accumulations, hysteresis loops keep their initial shape with $\frac{M_r}{M_s} \sim 1$. Only H_c and M_s are decreasing.

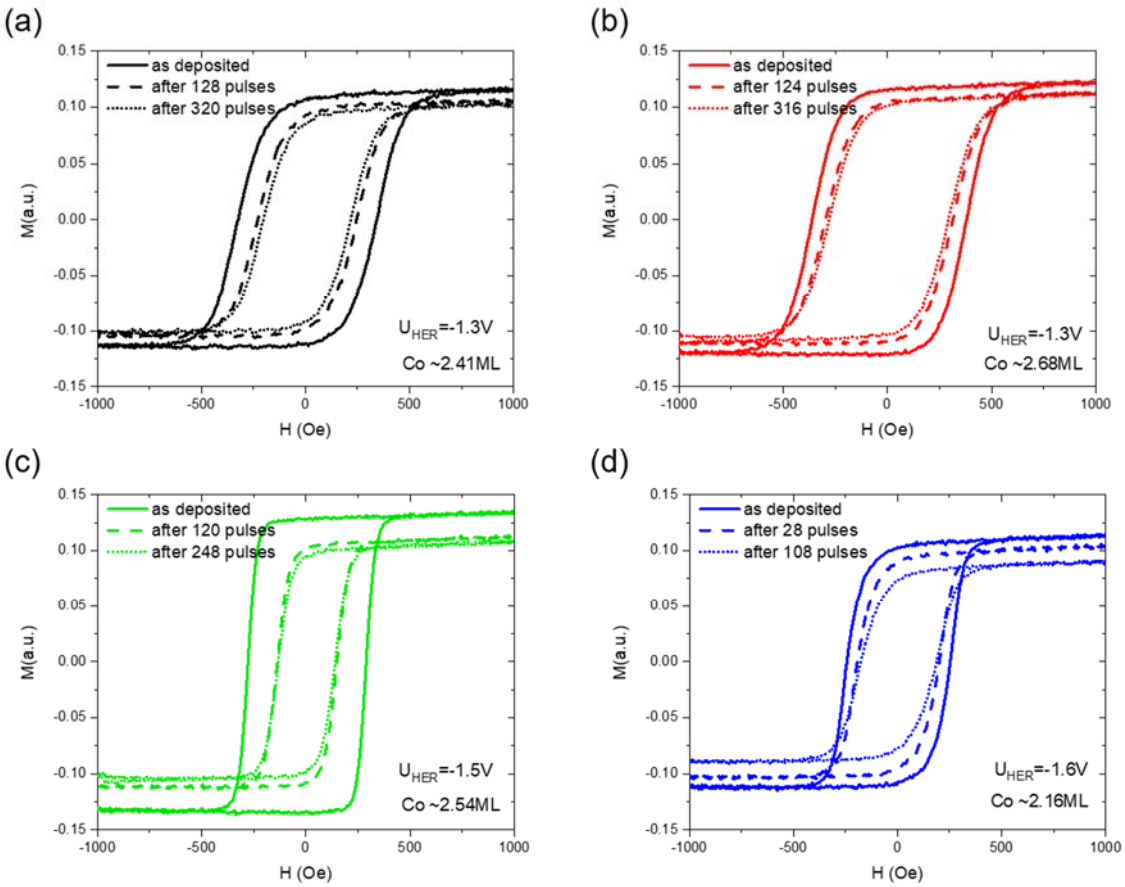

Figure 3-8 *M-H* plot variations upon HER pulses in each state: as-deposited covered by CO (solid line), intermediate states of HER pulses (dash line), and final states before dissolution (dot line). Deposited Co layer thickness (d_{Co}) and HER pulse amplitude (U_{HER}) in each plot are (a) $d_{Co} \approx 2.41$ML, $U_{HER} = -1.3V$. (b) $d_{Co} \approx 2.68$ML, $U_{HER} = -1.3V$, (c) $d_{Co} \approx 2.16$ML, $U_{HER} = -1.5$V, and (d) $d_{Co} \approx 2.16$ML, $U_{HER} = -1.6$V. Accumulated pulses in each state are indicated in each legend.

Table 3-1 Derived initial magnetic parameters of the electrodeposited samples

No.	Data Color	Estimated Co thickness (ML)	H_c^0 (Oe)	M_s^0	Γ (V^{-1})
1	Black	2.41	331.8	0.111	-0.18
2	Red	2.68	369.1	0.119	-0.23
3	Green	2.54	283.7	0.131	-0.31
4	Blue	2.16	298.8	0.113	-0.30

Figure 3-9a-d show the variations of $\Delta H_c/H_c^0$, $\Delta M_s/M_s^0$, the slope $\Gamma = \frac{\Delta H_c/H_c^0}{\Delta V}$ (measured between -0.7 and -1.0 V), and $\Delta R/R_0$ as a function of the number of potential pulses. For any $U_{HER} \leq -1.3\text{V}$, $\Delta H_c/H_c^0$, $\Delta M_s/M_s^0$, and $\Delta R/R_0$ decay with the number of pulses while M_r/M_s remains close to ~1. The amplitude of the decay $\Delta H_c/H_c^0$ which is the range of a few tens of % increases with more negative U_{HER}.

By contrast, slope Γ (panel c) shows different behavior. When $U_{HER} = -1.3\text{V}$, the electric field effect (EFE) is amplified and then it stabilizes while H_c and M_s are decreasing continuously. By contrast, when $U_{HER} = -1.5\text{V}$ and -1.6V, the EFE decrease after an initial increase during the first 10 pulses. In other words, the evolution of the EFE with the application of potential pulses depends on whether water is decomposed (-1.5 V and -1.6 V) or protons are reduced (-1.3 V) during the pulses.

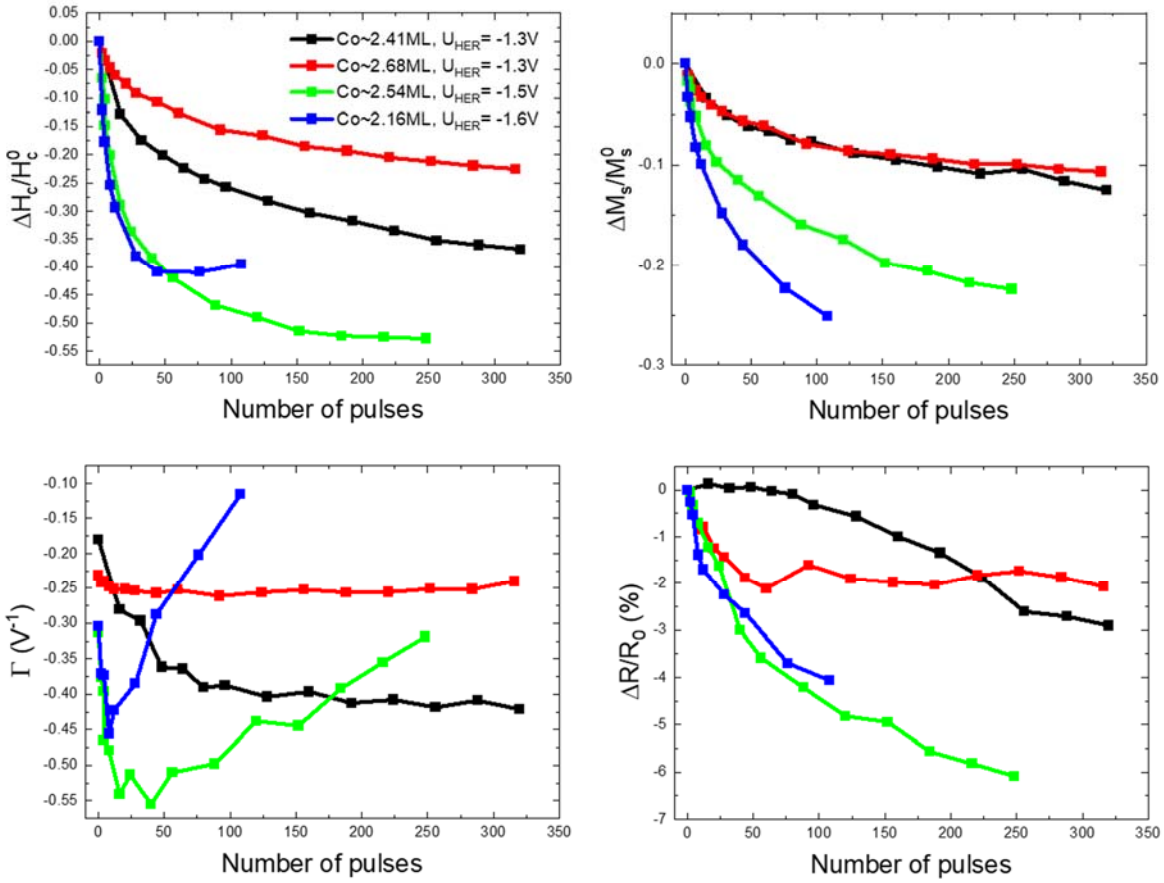

Figure 3-9 Influence of pulse amplitude on the magnetic properties of electrodeposited Co layer covered with a CO monolayer. (a) Influence of potential pulses on the relative coercive field with respect to its initial value $\Delta H_c/H_c^0$, (b) $\Delta M_s/M_s^0$, (c) value of EFE slope Γ, and (d) $\Delta R/R_0$. Each plot corresponds to a different pulse potential U_{HER}.

3. 5. Influence of HER pulse on Pt reflectivity

Because H is known to incorporate into Pt [113]–[115], we investigate here the influence of HER on Pt reflectivity. Figure 3-10 shows two CVs recorded with Pt 3/Ta 3/SiOx/Si electrodes in (a) CO-free / (b) CO-saturated standard solution (pH 3.5). The sample relative reflectivity ($\Delta R/R_0$) is measured simultaneously (red lines).

Figure 3-10a corresponds to the CO-free solution, i.e. the Pt surface is bare. The CV (10mV/s) starting from -0.2V to -1.4V, then 0V to -0.2V resembles published CVs [116] and presents all expected cathodic and anodic current waves. In the negative-going sweep of

potential, the Pt reflectivity starts decreasing shortly before the beginning of proton reduction (HER, $U < -0.7\text{V}$) which corresponds to the H adsorption potential range on Pt. Pt reflectivity continues decreasing in the entire HER range and is restored upon the positive-going sweep. In the CO-saturated solution, the Pt surface is covered by a CO monolayer. The corresponding CV is shown in Figure 3-10b. Rest potential in Figure 3-10b is fixed at -0.4V. The proton reduction onset potential is shifted to $U < \sim -0.8\text{V}$ in the presence of CO. Here the reflectivity change during the potential sweep is significantly larger than in the absence of CO. After completion of the two potential sweeps, the irreversible decrease $\Delta R/R_0$ is $\sim -0.1\%$ (Figure 3-10a) and $\sim -1.5\%$ in Figure 3-10b. Recovery of the reflectivity without CO takes place along with the H_2 oxidation (from -0.75V). Compared to Figure 3-10a, anodic current starting from $\sim 0.3\text{V}$ is observed in the presence of CO with a relatively large reflectivity recovery (~1%). This anodic current arises from the oxidation of H-absorbed in the Pt since the H-adsorption is not expected in the presence of CO. Both concomitant observations suggest that the H species are incorporated into the Pt electrode are not released upon reversing the potential in a region where no HER occurs. Similar behavior was reported with Pd electrodes: incorporated H is trapped when the surface is covered with CO [117]. The release of absorbed H-species requires applying a much more positive potential (Appendix 3. 6, Figure 3-13).

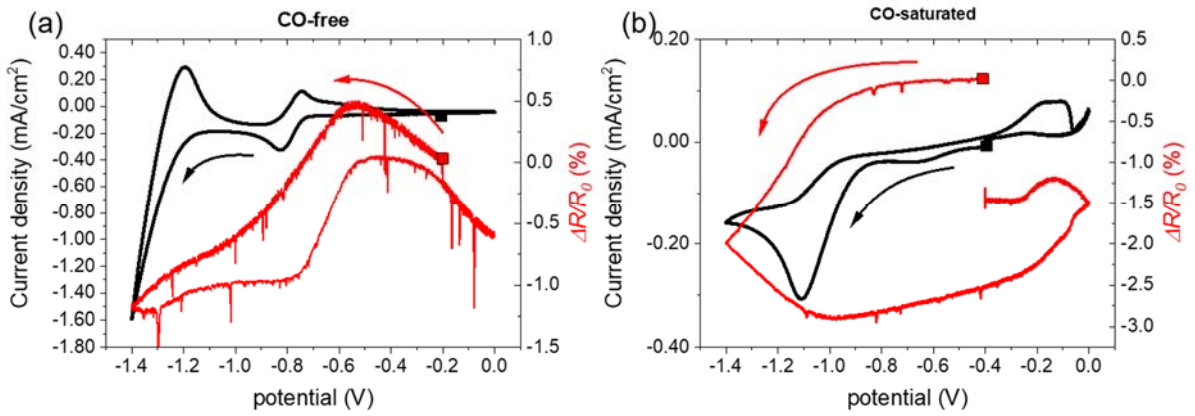

Figure 3-10 CVs on Pt3/Ta3/SiOx/Si substrate in (a) CO-free / (b) CO-saturated standard solution (pH 3.5). (a) CV starts from -0.2V to -1.4V, then 0V to -0.2V with the sweep rate of 10mV/s. Rest potential in the CO-saturated standard solution is $U = -0.2\text{V}$ regarding Pt oxidation current. Red lines show corresponding relative reflectivity during the CV.

Figure 3-11 shows the relative reflectivity changes induced by the application of potential pulses, starting with a fresh Pt 3/Ta 3/SiOx/Si electrode. Black symbols correspond to the CO-

free electrolyte. Red symbols correspond to CO-saturated solution (pH 3.5). The applied pulses are those shown in Figure 3-7. U_{HER} is -1.6V and the rest potential is $U_{rest} = -0.8V$. In the case of Pt electrode immersed in CO-free solution, relative reflectivity reduces -0.5% after 184 HER pulses ($\approx -18\text{mC}$). Since $U_{rest} = -0.8V$ is in the middle of H reduction/oxidation potential (see Figure 3-10), reduced H during pulses is not fully oxidized. However, relative reflectivity continuously decreases when CO is adsorbed on the Pt surface. Since the rest potential is not inducing any oxidation of H (see Figure 3-10), induced H after HER pulses accumulates continuously. After the application of 322 HER pulses ($\approx -45\text{mC}$), relative reflectivity reduces -6%.

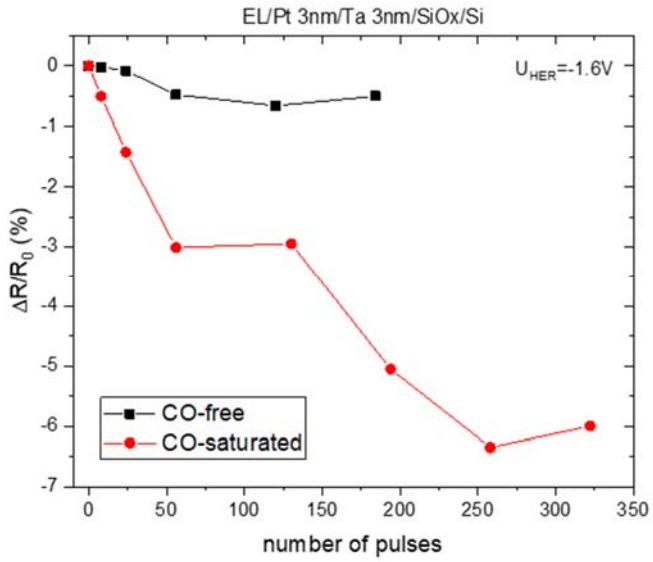

Figure 3-11 Relative reflectivity $\Delta R/R_0$ variation upon HER pulses on Pt 3nm/ Ta 3nm/SiOx/Si substrate in CO-free (black) / CO-saturated (red) standard solution. Applied HER pulse amplitude is $U_{HER} = -1.6\text{V}$.

The results presented in this chapter will be discussed together with those of Chapters 4 and 5, in a separate Chapter 6.

3. 6. Appendix

Co dissolution behavior

Figure 3-12a shows variations of the applied potential (black), normalized R by its initial value at 0s (red, R/R_0), and the magnetization at the maximum field (blue) during the Co deposition for 15s at -1.2V. Figure 3-12b shows the magnetic hysteresis at each time. The black hysteresis (0s) is overlaid with the blue hysteresis (150s). As we can see from ~90s, there is a remained reflectivity after Co dissolution (~1.5%) as well as the magnetic signal (see green hysteresis in Figure 3-12b). Then it returns to its initial value after reaching -0.2V while magnetic hysteresis returns to its initial state.

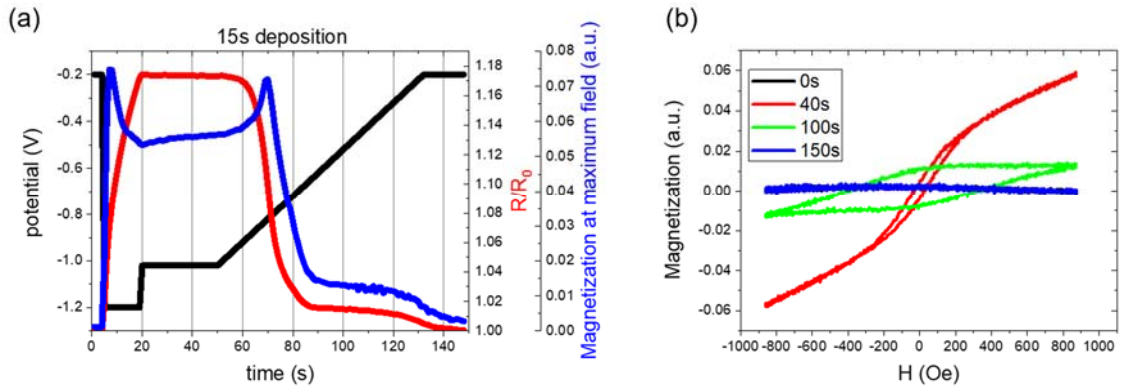

Figure 3-12 (a) Variations of the applied potential (black), R/R_0 (red), and the magnetization at the maximum field (blue) during the electrodeposition of Co for 15s. (b) Magnetic hysteresis at each time.

Reflectivity recovery after Pt Ox/Reduction process

After HER on CO adsorbed Pt, reduction of the reflectivity has been shown. Furthermore, the reduction of the reflectivity is continuous upon HER pulses (Figure 3-11). To recover reduced reflectivity, the potential is swept on Pt with CO. Figure 3-13a shows the current density (black) and the relative reflectivity with respect to its initial value (red, $\Delta R/R_0$). Applied potential is swept from -0.2V to 0.5V, then -0.75V to 0V and returns to -0.2V. The sweep rate is 10mV/s. First of all, Pt oxidation ($\text{Pt} \rightarrow \text{Pt}^{2+} + 2\text{e}^-$) starts around 0.1V. Meanwhile, reflectivity starts to drop. Following current density drop after Pt oxidation corresponds to Pt reduction ($\text{Pt}^{2+} + 2\text{e}^- \rightarrow \text{Pt}$) [118]. After finishing Pt reduction reaction, $\Delta R/R_0$ increases over its initial value (~1%). Figure 3-13b shows consecutive CVs after Figure 3-13a showing reflectivity only (the first CV is the same as Figure 3-13a). As we can see in Figure 3-13b, reflectivity recovers continuously after Pt oxidation and reduction. This may be

due to the structural reorganization during the oxidation/reduction process of Pt [119] which may release accumulated hydrogen.

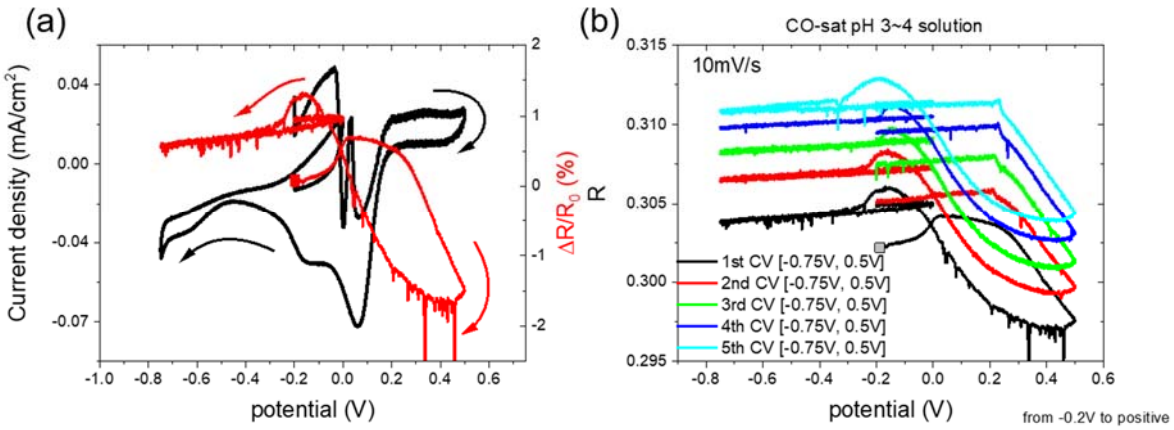

Figure 3-13 (a) Potential sweep on CO adsorbed Pt after accumulation of HER pulses. Potential sweeps from $-0.2\mathrm{V}$ to $0.6\mathrm{V}$, then $-0.75\mathrm{V}$ to $0\mathrm{V}$, returns to $-0.2\mathrm{V}$ with the sweep rate of $10\mathrm{mV/s}$. The black line shows the current density variation during the potential sweep and the red line shows the relative reflectivity with respect to its initial value ($\Delta R/R_0$). (b) Consecutive reflectivity R variations of Pt oxidation/reduction processes.

Chapter 4. Influence of hydrogen evolution reaction on the magnetic properties of sputter-deposited Co on Pt

4. 1. Introduction

In this chapter, we use sputter-deposited Co layers on Pt $3nm$/Ta $3nm$/SiO_x/Si(111). Samples are prepared by collaborator SPINTEC (Grenoble, FRANCE). Co layer on top of the Pt surface is deposited by magnetron sputtering on a thermally oxidized Si wafer. Co layer thickness varies from 0.5 nm (2.5 ML) to $1nm$ (5 ML) as a wedge-shaped. Then an Al layer is deposited and oxidized by oxygen plasma at room temperature. The Co layer is therefore capped with a layer (AlO_x). Figure 4-1 left with the AlOx layer is the scheme of the sample prepared by SPINTEC. Therefore, to study the influence of HER on magnetic properties, it will be necessary to remove the oxide without dissolving the Co layer. This step is presented in section 4. 3. Then we will study hydrogen-induced magnetic property variations with different thicknesses as in Chapter 3. Post-mortem energy-dispersive X-ray spectroscopy is introduced to supplement the HER study.

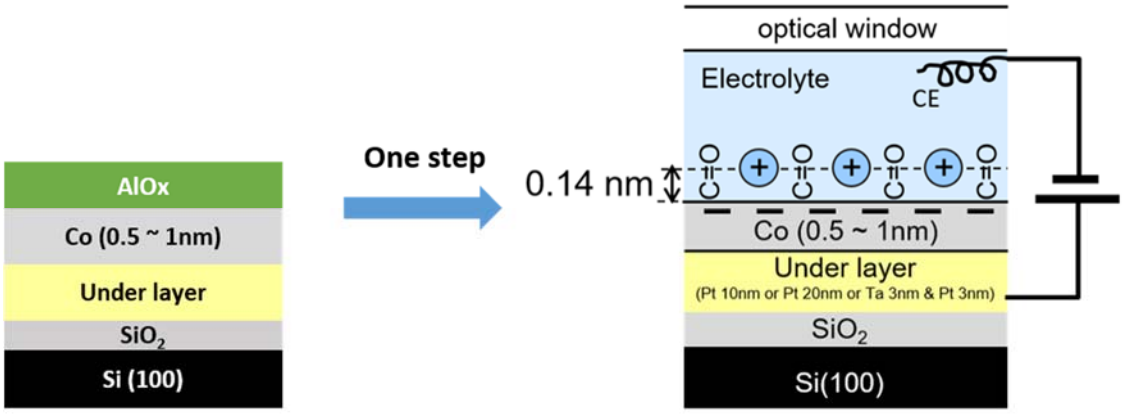

Figure 4-1 Schematic representations of the sample structure before (left) and after (right) immersion into the electrolyte (adapted from [42]).

4. 2. Magnetic characterizations of samples in air

As received samples were first characterized in air. Figure 4-2a shows magnetic hysteresis plots of samples with different thicknesses. For thicknesses up to 3.75 ML, plots are strictly square, i.e., the transition between the two magnetization orientations (up and down) is abrupt

with no tails. This indicates a strong perpendicular magnetization. The M-H plot is a bit different for films thicker than 4 ML, with a tail suggesting the presence of pinning centers blocking the DW propagation. Figure 4-2b, c show plots of the coercive field (H_c) and saturation magnetization (M_s) as a function of the nominal Co thickness. Data point correspond to two batches: AR99-19-4 (black) and AR99-19-6 (red). The coercive field passes through a maximum around 3.5 ML (~0.7 nm) as was observed in previous works [120]. Meanwhile, saturation magnetization shows linear to Co thickness in this thickness range. M_s increase in this range is mainly due to whole magnetic moment increases as Co thickness increases. However, extrapolated linear relations (black and red solid lines in Figure 4-2c) do not pass through 0. Instead, x-intercepts show 0.86 ML and 0.63 ML respectively. These shifts may come from an alloy between Pt − Co or an oxidation of Co (Co − O) layer adjacent to AlO_x layer [121], [122].

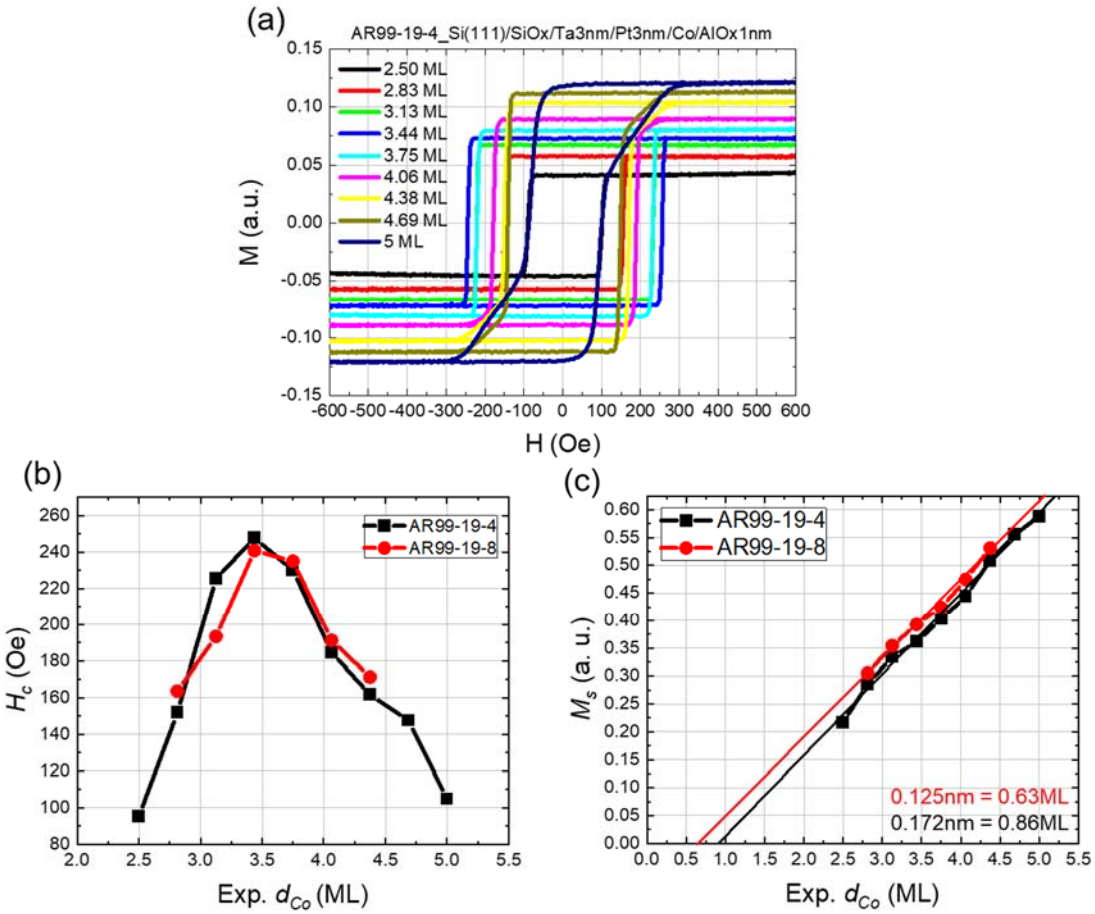

Figure 4-2 (a) Hysteresis in different Co thicknesses measured in air with the presence of the capping layer. (b) Derived coercive field variations as a function of estimated Co thickness (Exp. d_{Co}) in two batches: AR99-19-4 and AR99-19-8. (c) Saturation magnetization variations as a function of Exp.d_{Co}. Solid lines are linear fitted curves and x-intercepts are indicated in the same colors.

4. 3. Immersing sample in the electrolyte

a. Immersion procedure

Following the Appendix 4. 6, a CO-saturated solution of pH 1 is used for dissolving AlO_x layer homogeneously and potential of -0.75 V is applied to the sample. This potential is chosen to minimize as much as possible the formation of H_2 bubbles when the cobalt surface will become in contact with the electrolyte. The use of a CO saturated solution ensures that the cobalt surface does not dissolve at this potential if it is immediately covered with CO while the

AlOx layer is dissolved (see 3. 3.b). After ~60 min, the solution is exchanged with the CO-saturated pH 3.5 solution to reduce the HER rate to nearly zero at -0.75 V. During this procedure, the characteristic parameters of the sample are monitored (see Figure 4-3a-c where the gray shaded region corresponds to the sample in the solution of pH 3.5). As anticipated the electrochemical current decreases and stabilizes around $-30\mu A/cm^2$ at pH 3.5. The other plots show that the sample goes through transient magnetic states and we present in panel (d) selected magnetization plots extracted from a complete set. It is beyond the scope of the work to discuss the magnetic state at intermediate stages because the sample surface might be partly covered by AlOx (~1700s in Figure 4-3a-c).

The main point is the comparison of the magnetic states in air, right after immersion (i.e. the AlOx layer is still present and is in contact with the electrolyte) and complete removal of the AlOx layer. Figure 4-3d shows three magnetic hysteresis loops at each point. Magnetic state in air and just after immersion are supposed to be the same. However, there are electrolyte and glass window in front of the sample after immersion which induce the increase of M_s. After AlOx is fully dissolved, Co in contact with CO-saturated electrolyte is perpendicularly magnetized and M_s and H_c reduce -5%.

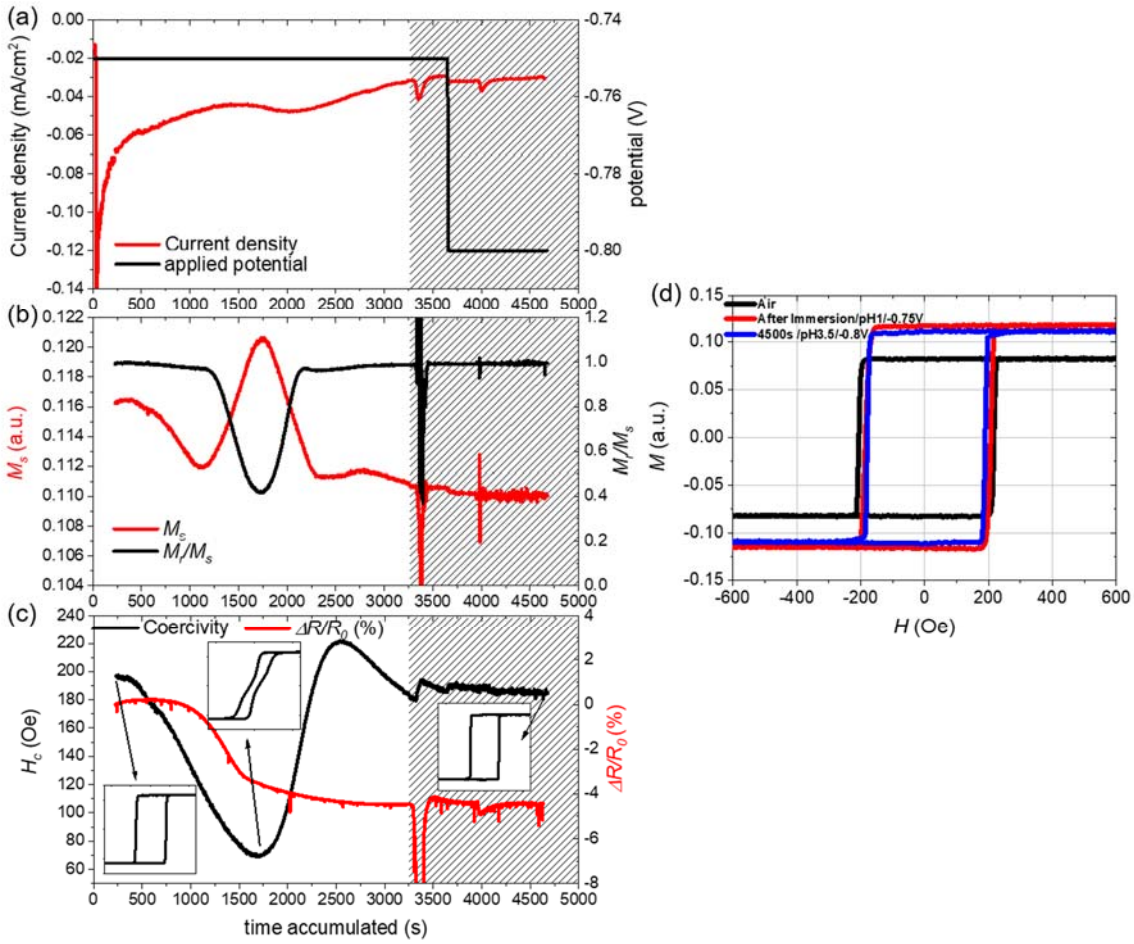

Figure 4-3 (a) Current density variation (red) with applied potential (black), (b) saturation magnetization M_S (red) with M_r/M_S (black), and (c) coercive field (black) with $\Delta R/R_0$ as a function of immersion time. Insets in (c) are magnetic hysteresis at a given time. The Gray region indicates that the solution is changed from pH 1 to pH 3.5 (~3250s). (d) Hysteresis variation at each condition: in Air (black), after immersion in CO-saturated pH 1 solution (red), and 4500 seconds after immersion in CO-saturated pH 3.5 solution (blue).

To further ensure whether the capping layer is dissolved, one potential pulse (0.1 s with $U_{HER} = -1.3$V) is applied. The result is shown in Figure 4-4a where the red line is the transient current measured during the pulse. For comparison, the black line is that measured with an electrodeposited Co layer. Both plots overlay well, which confirms that the AlOx was indeed fully dissolved. In case the AlOx layer is not fully dissolved, a smaller current is measured (green line).

Another criterion for the complete dissolution of the AlOx layer is measuring the magnitude and sign of the electric field effect. To this end, M-H plots are measured upon application of a

potential sweep in the range [-0.7V : -1.0V] where no HER occurs. As expected the plot (red symbols) is linear and its slope $\frac{\Delta H_c/H_c}{\Delta V} < 0$ is close to that of the electrodeposited layer of similar thickness (black symbols),: Note that when the AlOx is not fully dissolved, an ill-defined behavior is observed (green plot): the plot presents generally a hysteresis between the negative and positive going sweeps of potential.

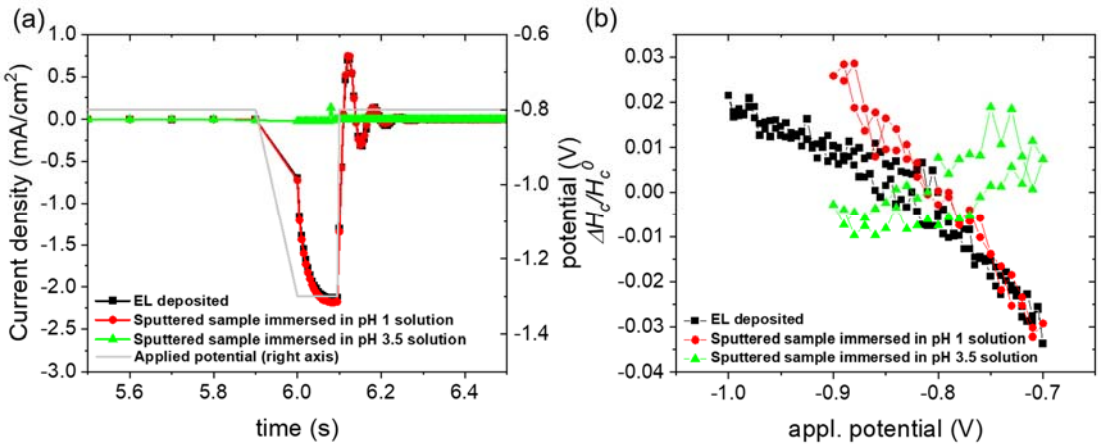

Figure 4-4 (a) Current density variations during one HER pulse ($U_{HER} = -1.3V$) in CO-saturated standard solution (pH 3.5) for different samples: electrodeposited sample (black), sputtered sample after dissolving capping layer by immersing the sample in pH 1 solution (red, the solution is switched to pH 3.5 solution after stabilization) and sputter-deposited sample stabilized in CO-saturated standard solution from the beginning(green). (b) Corresponding relative coercive field variations with respect to its initial value ($\Delta H_c/H_c^0$) by sweeping potential from -1.0V to -0.7V (sputter-deposited sample CV range starts from -0.9V). The slope is derived from here to estimate the electric field effect.

b. Initial magnetic parameters of samples after removal of the oxide layer

Figure 4-5 compares the magnetic parameters of as immersed samples at -0.8 V (green symbols) with those measured when the sample is covered with the AlOx layer in the air (black symbols) or in the electrolyte (red symbols). Figure 4-5a shows that the saturation magnetization M_s varies linearly with the nominal thickness d_{Co}. The straight line is however not going through the origin. The intercept is ~ 0.80 ML when the AlOx covers the Co layer and increases to 1.22 ML after the complete dissolution of the oxide. The intercepts with AlOx suggest that the Co film is partially oxidized upon deposition of the AlOx capping layer. Upon complete dissolution of the AlOx layer about 1.2 ML of cobalt has been dissolved. In the following, the nominal Co thickness, i.e. as-deposited before AlOx deposition, is

mentioned to describe the samples.

The slopes of the straight-line increased from 0.027 to 0.037 / 0.039 after immersing in the electrolyte. This increase may originate from the larger MOKE sensitivity in the presence of the electrolyte.

The corresponding thickness dependence of the coercive field is shown in panel (b). H_c with the presence of AlOx shows its maximum value around 3.5 ML and decreases when Co thickness is thicker which corresponds to the work of T. Ueno et al. (2015). On the other hand, after the dissolution of AlO_x, d_{Co} the maximum of H_c is shifted to ~0.45ML.

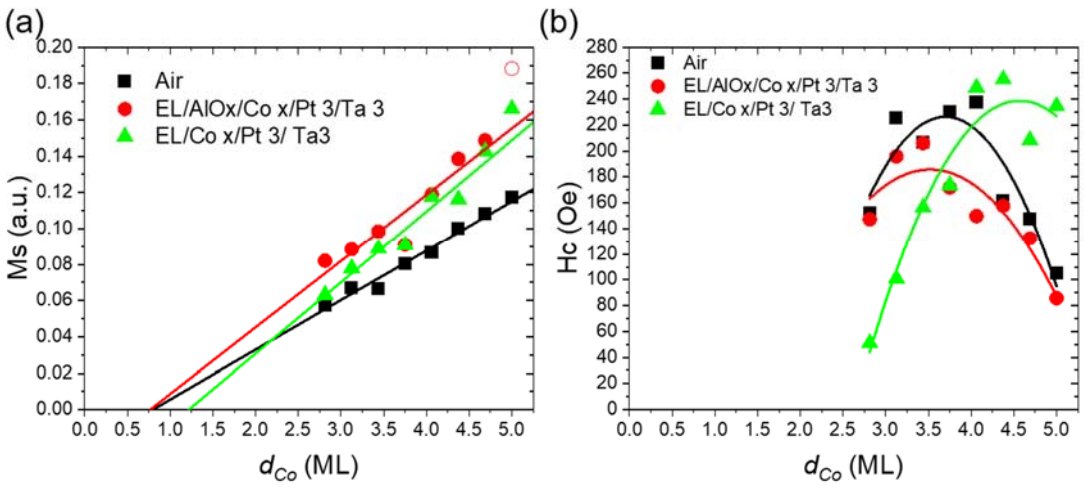

Figure 4-5 (a) Saturation magnetization variations in the air (black), right after immersing in CO saturated standard solution (red, AlO_x in contact with the electrolyte) and after the dissolution of AlO_x (green). Solid lines are linear fitted curves. (b) Corresponding coercive field variations as a function of Co thickness (d_{Co}). Applied potential in the electrolyte is $U_{HER} = -0.8V$. Quadratic fitted curves are along with each data.

Additionally, the electric field effect (Γ) derived from CV by sweeping potential from -0.9V to -0.7V (as in Figure 4-4b) is obtained after the dissolution of the entire AlOx layer and before the application of HER pulses (Figure 4-6). Except for the data having a thickness of 3.13ML, derived slopes are independent of the Co thickness in the range 2.81ML - 5ML. Derived slopes (Γ) in this Co thickness range varies around $-0.3V^{-1}$ with some scatter.

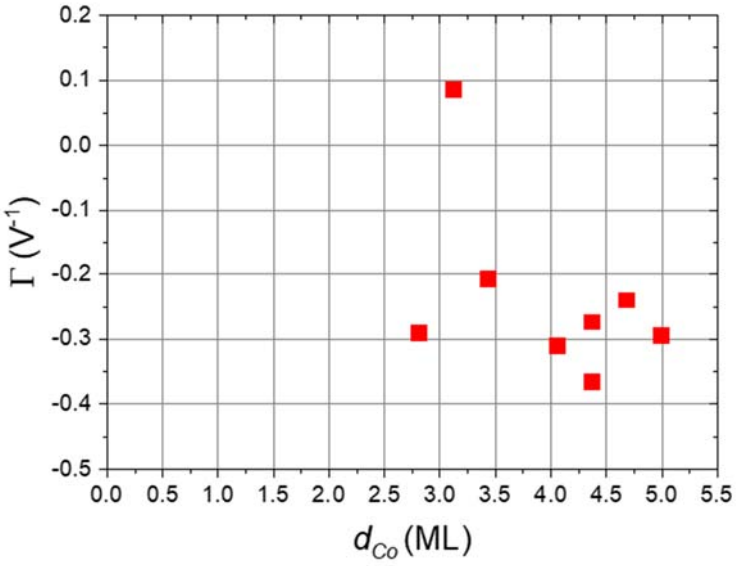

Figure 4-6 Derived electric field effect slope (Γ) variation as a function of Co thickness before application of HER pulses. CV is swept from -0.9V to -0.7V with a sweep rate of 10mV/s.

4. 4. Influence of applying potential pulses on magnetic properties

As in the previous chapter, short potential pulses are applied for better control on the modification of the magnetic properties. The procedure is the same and we show the below results for Co layers of variable thicknesses. The immersion procedure is that described above. The Co thickness is the nominal value given by Spintec.

Table 4-1 gives the initial magnetic parameters, i.e. after the dissolution of the AlOx capping layer and before applying potential pulses.

Table 4-1 Magnetic parameters of samples after immersion in the electrolyte according to the procedure described in section 4. 3.a.

Estimated d_{Co} (ML)	Batch	H_c (Oe)	M_s (a.u.)	EFE slope (V^{-1})
2.8	AR99-19-4	52.20	0.063	-0.30
3.1	AR99-19-4	101.07	0.078	+0.08
3.4	AR99-19-5	156.59	0.089	-0.21
4.1	AR99-19-6	180.06	0.110	-0.31
4.4	AR99-19-4	255.26	0.116	-0.37
4.4	AR99-19-5	198.16	0.122	-0.27
4.7	AR99-19-5	181.26	0.136	-0.24
5.0	AR99-19-4	234.77	0.166	-0.29

Figure 4-7 shows magnetic hysteresis variations from before the application of HER pulses (a-a2), after 10 HER pulses (b-b2), and after 30 pulses (c) or several 100 pulses (c1-c2). The amplitude of HER pulse is $U_{HER} = -1.6$V. In the case of the thinnest sample (2.81ML), H_c decreases down to zero and the magnetization becomes in-plane. In the case of the two other samples, the magnetization remains perpendicular and the main change is the decrease of H_c. In the case of 5ML, the shape of the hysteresis loop suggests the presence of pining centers with a distribution of energies. (see red circles in Figure 4-7a2, b2). These seem to disappear after the application of a sufficient number of pulses because the magnetization plot becomes strictly perpendicular (Figure 4-7c2) while the H_c value keeps the same.

.

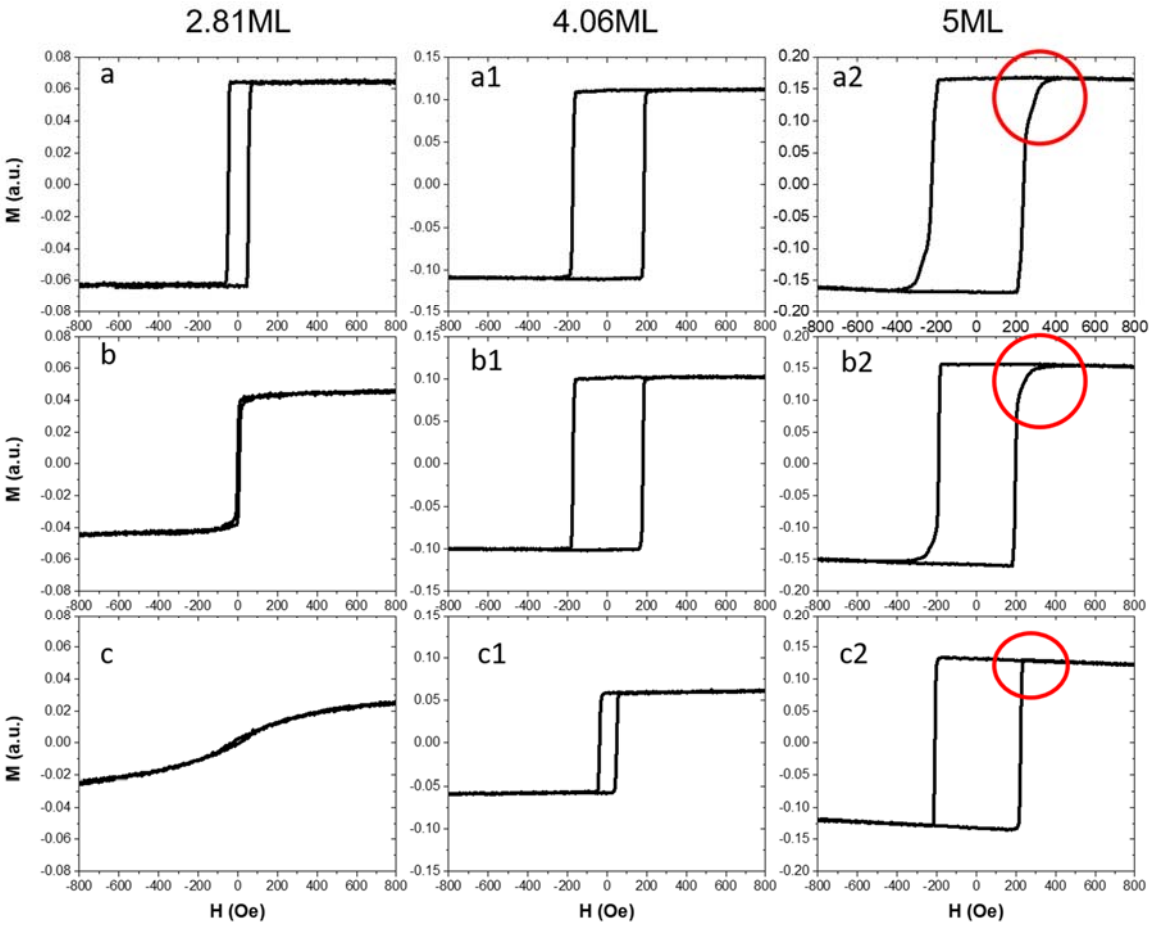

Figure 4-7 Magnetic hysteresis variations upon HER pulses for different Co thicknesses: (a-c) 2.81ML, (a1-c1) 4.06ML, and (a2-c2) 5ML. The first row is the state before the application of HER pulses, the second is after 10 HER pulses with $U_{HER} = -1.6$V, the last row is after 30 pulse (c) or several 100 pulses (c1-c2).

Figure 4-8a shows relative saturation magnetization variations $\Delta M_s/M_s^0$ as a function of the number of pulses ($U_{HER} = -1.6$V, $U_{HER} = -1.3$V for unfilled brown colored data having $d_{Co} = 4.4$ ML). The thinnest sample (black, 2.81 ML) shows a reduction in M_s as 75% under 40 HER pulses (Figure 4-8a). The next two samples (3.13 ML and 3.44 ML) stop their reduction by around 45% since H_c drops already more than 90% (see Figure 4-8b). To investigate HER pulse amplitude dependence, $U_{HER} = -1.3$V pulses are accumulated on another 4.38ML sample (unfilled brown colored data). Except for the case with $U_{HER} = -1.3$V in Figure 4-8a, M_s reduces around 10~20% after 100 pulses even thick samples having more than 4.69 ML. M_s reduction having a thickness of more than 4.06 ML can be relatively generalized. In other words, M_s reduction has vulnerable dependence on Co thickness except for thin samples (2.81 ML to 3.44 ML).

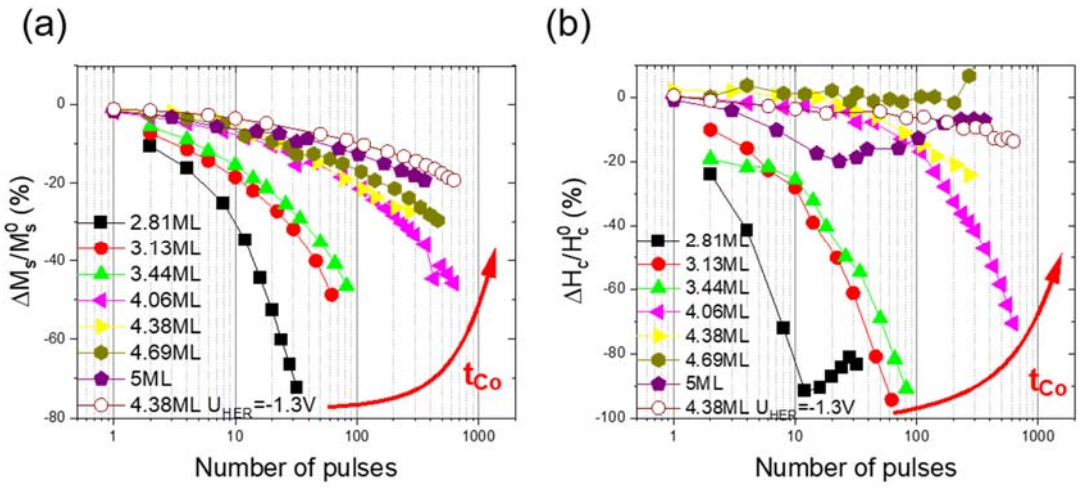

Figure 4-8 The relative variations of M_s (a) and H_c (b) with respect to their initial values as a function of accumulated HER pulses in different d_{co} range. Applied HER pulse amplitude is -1.6V except for the sample having 4.38ML with unfilled data ($U_{HER} = -1.3$V).

The next magnetic parameter variation upon HER pulses is $\Delta H_c/H_c^0$ (Figure 4-8b). Coercive fields in d_{Co} range from 2.81ML to 3.44ML reduce more than 80% after applying less than 100 HER pulses. Samples having $d_{Co} > 4.06$ ML are more resistant to HER pulses as Co thickness increases. When HER pulses of -1.3V are applied (unfilled brown), the decrease of H_c is comparatively smaller than at -1.6V (yellow).

To investigate Co thickness (d_{Co}) dependence on magnetic properties after applying 10 HER pulses, relative variations of M_s and H_c as a function of d_{Co} is obtained in Figure 4-9. Decrease of M_s and H_c show similar behaviors: the thinner Co thickness, the more reduced. H_c. For the thinnest sample (2.81ML) shows a steep reduction -90% while M_s reduces -30%.

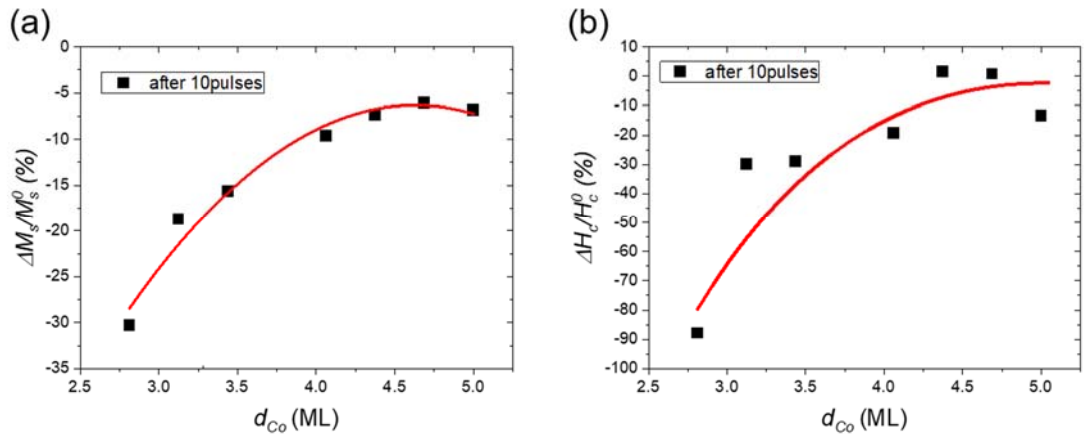

Figure 4-9 Derived (a) $\Delta M_s/M_s^0$ and $\Delta H_c/H_c^0$ as a function of Co thickness after application of 10 HER pulses ($U_{HER} = -1.6\text{V}$). Data is derived from Figure 4-8.

Apart from the above magnetic parameters, the sample reflectivity upon HER pulses is shown in Figure 4-10. Figure 4-10a shows the relative variation reflectivity with respect to its initial value ($\Delta R/R^0$) as a function of accumulated HER pulses. The behaviors of $\Delta R/R^0$ reduction upon HER pulses for different d_{Co} is similar to that of H_c and M_s. To compare the result of Figure 4-10 with the result of Figure 3-11, the reflectivity is plotted as a function of the cumulated HER charge (q) obtained by integrating induced current upon HER pulses (Figure 3-11 has pre-pulses before applications of $U_{HER} = -1.6\text{V}$). Figure 4-10b shows $\Delta R/R^0$ as a function of negative cumulated charge ($-q$) including the result of Figure 3-11 (dark green, bare Pt with CO-saturated electrolyte). With such X axis normalization, $\Delta R/R^0$ curves better overlap (except for the thinnest film) and are also consistent with that on bare Pt in CO-saturated solution. This resemblance is a strong indication that $\Delta R/R^0$ changes in the presence of Co are caused by modification of the Pt layer induced by HER.

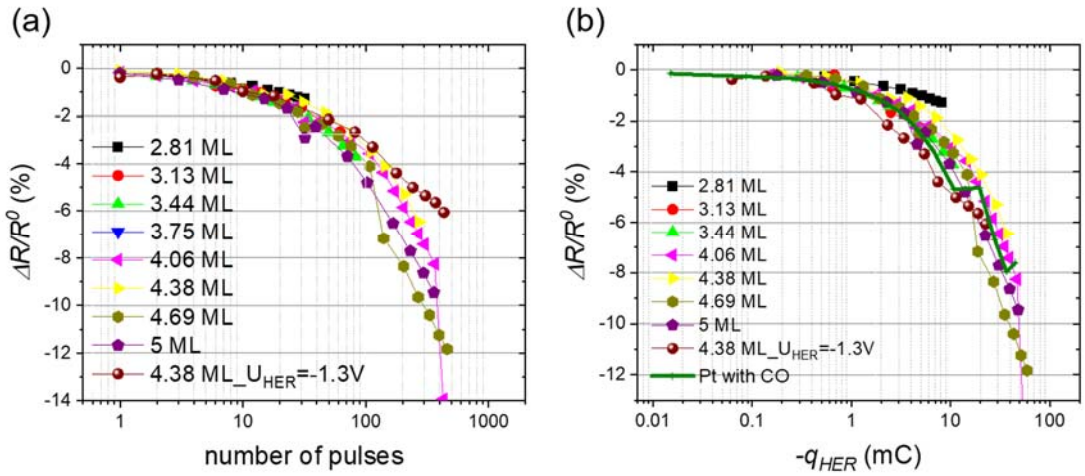

Figure 4-10 (a) The relative variation of the reflectivity with respect to its initial value ($\Delta R/R^0$) as a function of accumulated HER pulses in different thicknesses. (b) The variation of $\Delta R/R^0$ as a function of negative cumulated charge. HER pulses on bare Pt in CO-saturated electrolyte result is added (derived from Figure 3-11). Charge is integrated from induced current during the HER pulse.

Lastly, the electric field effect is evaluated by deriving slope Γ (V^{-1}) from the relation between $\Delta H_c/H_c^0$ and applied potential (U). Figure 4-11 shows slope variation as a function of accumulated HER pulses for different d_{Co}. Samples from 2.81ML to 3.44ML show irregular variations of EFE slope with no clear trend. However, Co films thicker than 4.06ML shows regular behavior. Regardless of Co thickness, EFE slopes are rather constant up to 10-20 pulses and then decrease to zero as a power law. Again we observe the same trend in the electrodeposited sample.

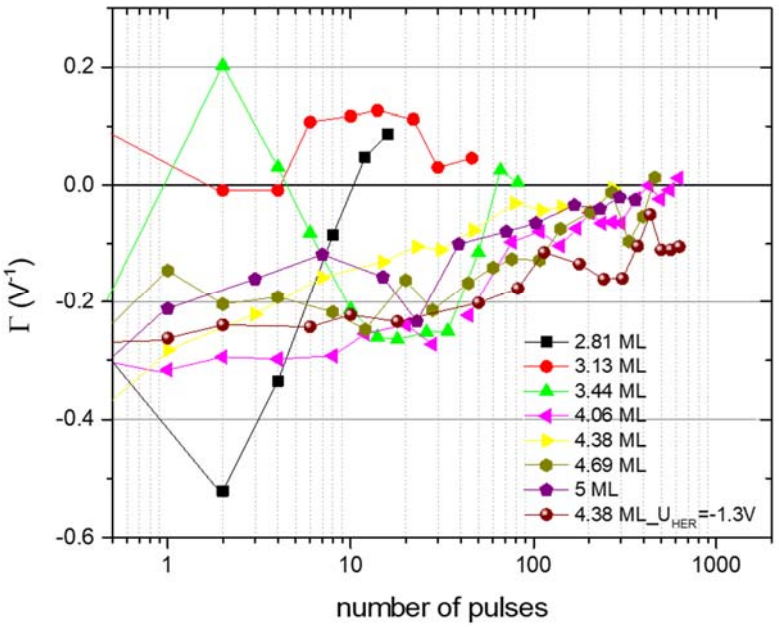

Figure 4-11 Derived electric field effect slope (Γ) variation as au function of accumulated HER pulses in different Co thicknesses.

4. 5. Post-mortem Energy-dispersive X-ray spectroscopy (EDX) characterization

The results above indicate a reduction of M_s and of the relative reflectivity $\Delta R/R^0$. Both observations may suggest that part of the Cobalt layer was dissolved during the application of potential pulses. This point is checked below using post-mortem SEM-EDX (scanning electron microscope-energy dispersive X-ray spectrometer) analysis of the sample. Two different samples are used.

Figure 4-12 shows results for a sample after the immersion procedure as described above (the capping layer is removed). No potential pulses were applied. A schematic of the sample is in the upper-right corner of Figure 4-12a and the SEM image corresponds to the region of interest (ROI) as indicated as a red circle. Figure 4-12b shows the EDX spectrum as a function of X-ray energy acquired in different regions. Spectrums in color correspond to each colored box in Figure 4-12a. As a reference of the sample, we take spectrum (#1) because it corresponds to the region out of the electrolyte exposed area, where the original Co layer is intact: it shows

Co peaks (~0.65 keV and ~0.8 keV) and Al peak (~1.5 keV). In contrast, Co and Al peaks are not observed in the electrical contact regions (red box) as shown in spectrum #2. Here both the capping layer and Co layer were completely dissolved by applying a drop of solution for ~20 min (see Appendix 4. 6a). In the region where the sample was exposed to the electrolyte (green box) one clearly observes a Co peak at ~0.8 keV and no Al peak (spectrum #3), which confirms the immersion procedure works well to dissolve the capping layer selectively. There is only a slight decrease of the Co signal by 18% compared to spectrum #1.

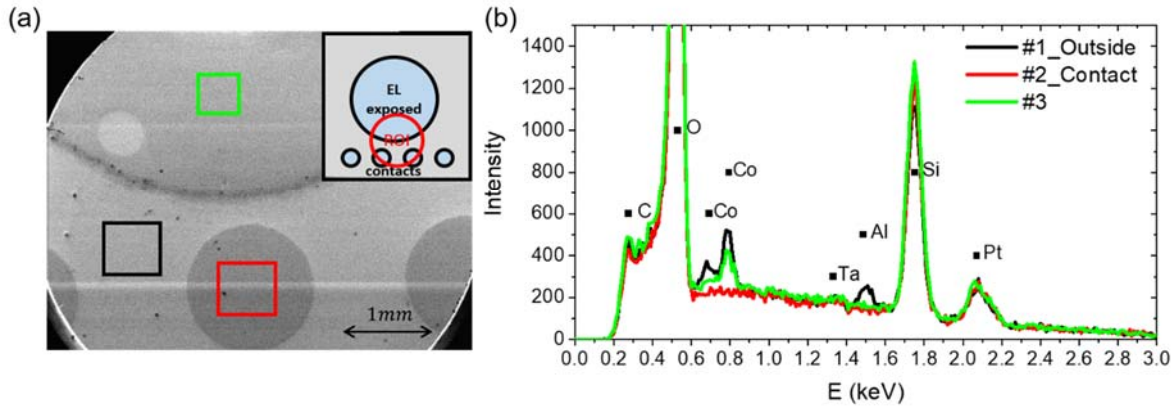

Figure 4-12 EDX-SEM result after stabilization in the electrolyte. The sample didn't undergo HER pulses. (a) SEM image focused on the region as indicated ROI in the scheme. Boxes in different colors represent acquisition boxes. (b) ED spectrums are obtained from corresponding color boxes from (a).

Figure 4-13 concerns a 4.38 ML Co layer to which potential pulses have been applied. The applied pulse had an amplitude of $U_{HER} = -1.6\text{V}$. For this sample H_c decreased by 25.7% and M_s by 26.8% after applying 271 HER pulses (Figure 4-8). Additionally, the EFE slope derived from $\Delta H_c/H_c^0$ vs U starts from $-0.37\ \text{V}^{-1}$ and it ends with nearly 0. Black (#1) and red (#2) data in Figure 4-13 correspond to the unexposed region and the electrical contact region respectively. They show similar behavior to Figure 4-12. Green (#3), blue (#4), and cyan (#5) regions are exposed to the electrolyte. The Co peak around 0.8keV in plots #3 to #5 remains essentially unchanged compared to the peak from the unexposed region (#1). In other words, the reductions in M_s after application of the potential pulses is not coming from the loss of cobalt.

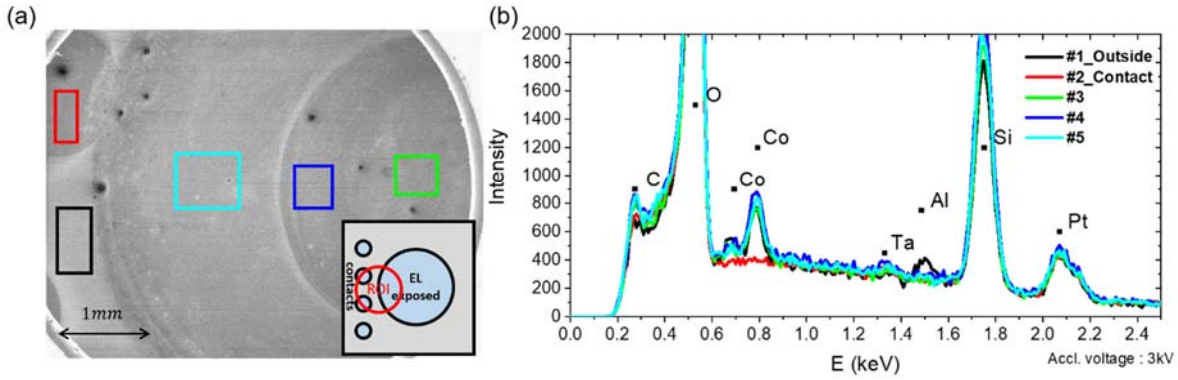

Figure 4-13 EDX-SEM result after applying 271 HER pulses. (a) SEM image focused on the region as in Figure 4-12. Boxes in different colors represent acquisition boxes. (b) EDX spectra are obtained from corresponding color boxes from (a).

4. 6. Appendix

a. Dissolution of capping layer (AlOx)

In our experiments, the sputter-deposited sample will be set in contact with the electrolyte by dissolving the AlO_x capping layer under potential control. Here we briefly investigate the chemical dissolution of the capping layer. As indicated in Figure 4-14, the rate of alumina dissolution depends strongly on pH [123]. Following this plot, the etch rate of alumina is expected to be $\sim 0.25\ \mathrm{nm/h}$ (considering atomic density of AlO_x as $4\ \mathrm{g/cm^3}$) in our standard solution ($0.1M\ K_2SO_4 + 1\mathrm{mM}\ H_2SO_4 + 1\mathrm{mM}\ KCl, \mathrm{pH}\ 3.5$). However, using a solution of $\mathrm{pH}\ 2$ solution increases the etch rate by a factor of 10 ($\sim 25\ \mathrm{nm/h}$). Therefore, it is more efficient to dissolve AlO_x with the more acidic solution first, then switch to the standard solution ($\mathrm{pH}\ 3.5$).

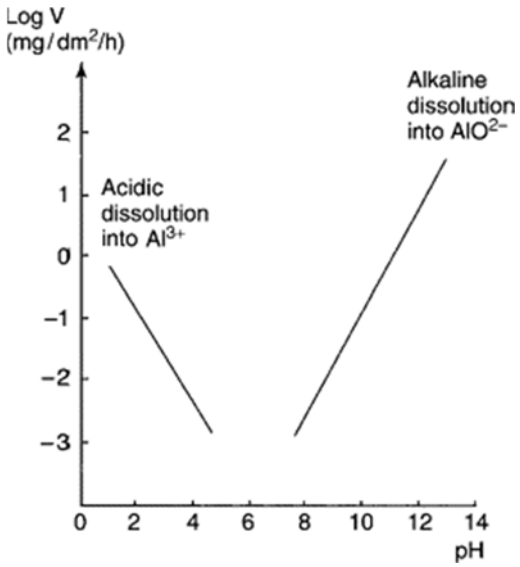

Figure 4-14 Corrosion rate (V) of alumina in aqueous media as a function of pH (adapted from [123])

Figure 4-15 shows optical images of the sample after a drop of the solution has been applied on its surface for 15min. Solutions of $1\mathrm{M}\ K_2SO_4 + 1\mathrm{mM}\ KCl$ with pH adjusted between 3.5 and 1 were used. The sample is rinsed with distilled water and dried before observation. The bright part of the sample was not exposed to the solution and the dark part corresponds to the region that was covered by the drop of solution. All images are normalized by their background (a region with a capping layer). Red arrows inside of images indicate a few locally undissolved areas. The sample exposed to the solution of pH 1 presents a homogenous and darker color. To compare the contrast difference between exposed and unexposed regions, we introduce a

parameter G_{diff}:

$$\boldsymbol{G_{diff} = \frac{G_{unexposed} - G_{exposed}}{G_{unexposed} + G_{exposed}}} \quad 4.1$$

where $G_{unexposed}$ is a gray level of an unexposed region and $G_{exposed}$ is that of a region that was exposed to the electrolyte. G_{diff} values according to their pH and exposure time are in Table 4-2. Gray average values are measured near the border within a square box. In conclusion, pH 1 solution is required to dissolve AlO_x homogeneously and the exposure more than 15 minutes also is required to ensure the surface state.

Table 4-2 Grayscale difference (G_{diff}) dependence on acidity and exposure time

pH	Exposure time (minutes)	G_{diff} (%)
3.5	15	1.52
2	15	2.29
1	15	2.46
1	20	5.02

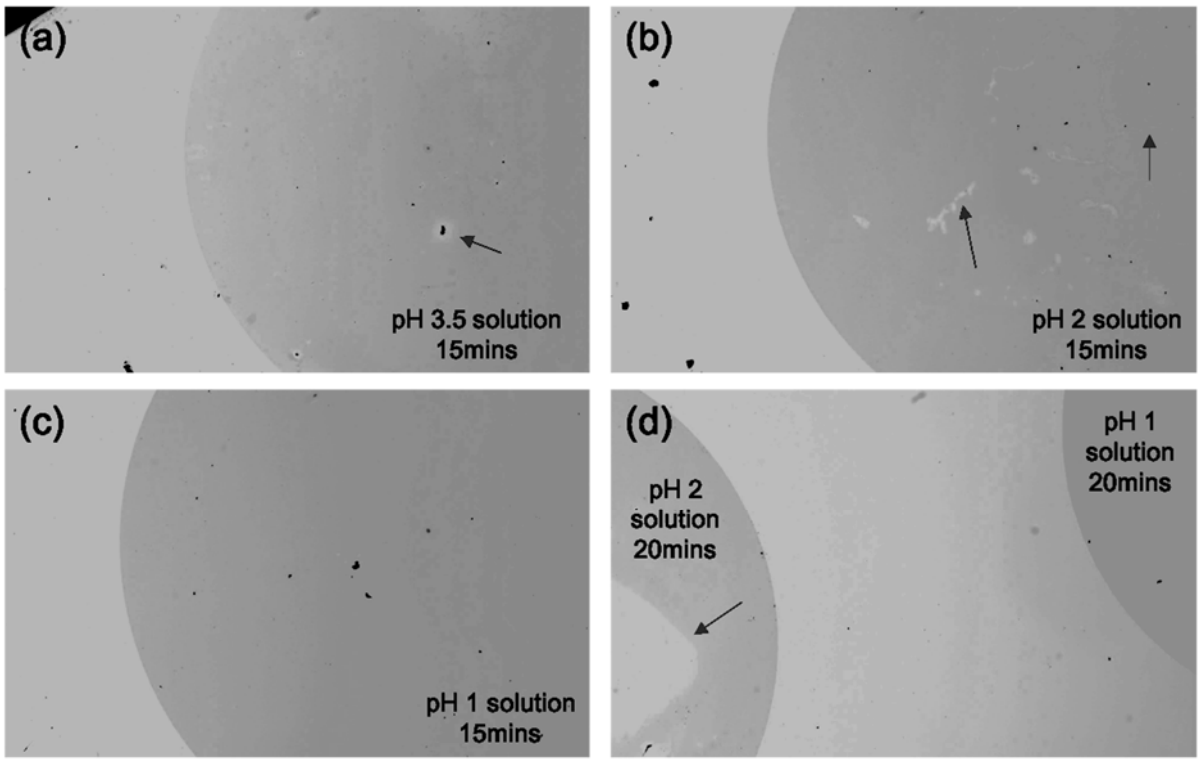

Figure 4-15 Optical microscopy images of the capping layer dissolution varying exposure time and acidity of solution as (a) 15minutes with pH 3.5, (b) 15minutes with pH 2, (c) 15minutes with pH 1 (d) 20minutes with pH 2 (left) and 20minutes with pH 1 (right). A dark area corresponds to a region that was exposed to the electrolyte. Red arrows indicate the undissolved area inside of the exposed zone

b. Influence of potential sweep in the range [-1.7V, -0.7V]

Figure 4-16 shows the variations of the magnetic parameters of a Co 0.7nm/Pt 20nm/SiOx/Si as a function of the applied potential. The electrolyte is the CO-saturated electrolyte of pH 3.5 and the sweep (10 mV/s) is extended to $-1.7\mathrm{V}$ where water decomposition occurs (see Eq. 3.3, $U < \sim -1.6\mathrm{V}$ as CO shifts HER onset potential). Figure 4-16a shows the current density (black) together with the relative reflectivity $\Delta R/R_0$ (red) as a function of applied potential. Figure 4-16b, c show the corresponding variations of $\Delta H_c/H_c^0$ and $\Delta M_s/M_s^0$.

The CV was described before: the wave C1 and exponential current C2 correspond to the reduction of protons and water into H_2. Along with the potential sweep, an irreversible drop of $\Delta R/R_0$ is observed. As will be discussed later, the drop may be assigned to H-incorporation into Pt.

Looking at the magnetic parameters, Figure 4-16b may be decomposed in successive phases:

$\Delta H_c/H_c^0$ increases linearly with applied potential (EFE) down to $-1.0\mathrm{V}$, before it abruptly decreases in the potential range of wave C1; a second linear behavior is observed down to $U = -1.5\mathrm{V}$ as long as the reduction of protons is limited by mass transport. A second nonlinear decay of $\Delta H_c/H_c^0$ occurs while water starts to decompose into H_2 (exponential current C2). On the return scan, the variations of $\Delta H_c/H_c^0$ are quasi linear. Quite noticeable is the *irreversible* drop of $\Delta H_c/H_c^0$ after completion of the potential sweep. There is also an irreversible drop of $\Delta M_s/M_s^0$ along the potential sweep. H_c and M_s after CV stay constant for 10 minutes. Likewise, for electrodeposited layers, these observations confirm that the magnetic properties of the Co/Pt layer are irreversibly altered by HER. This mechanism will be discussed later on.

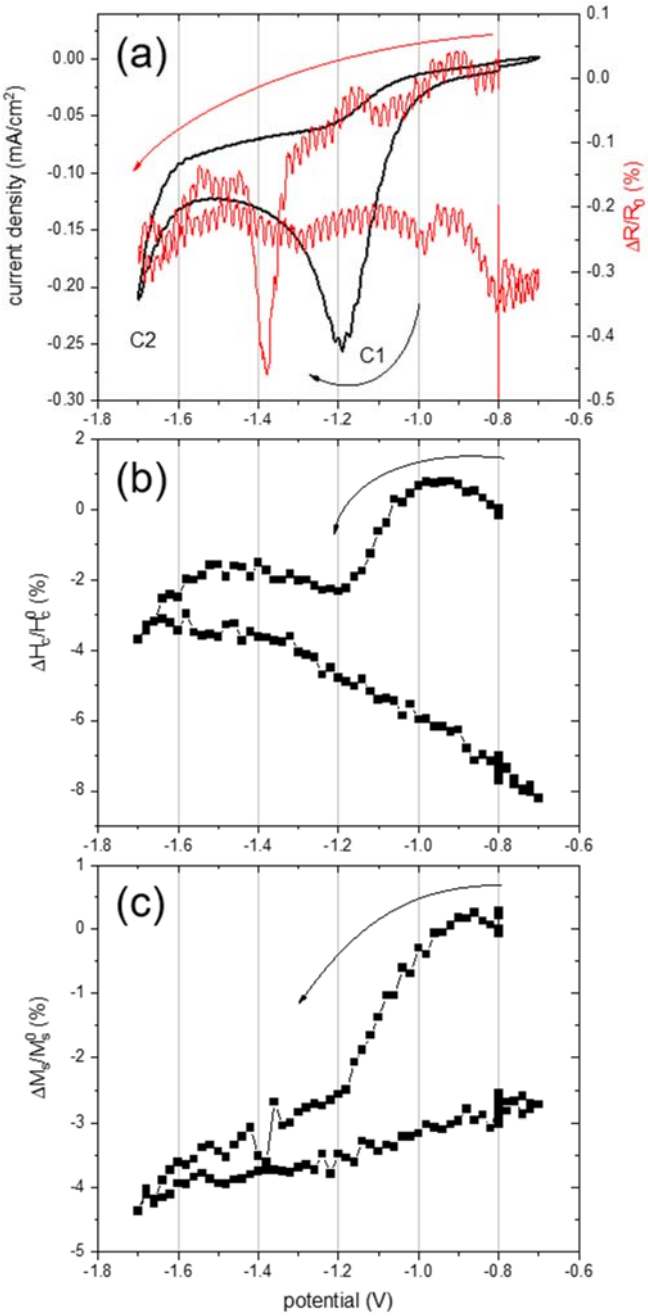

Figure 4-16 (a) Cyclic voltammogram together with the relative reflectivity $\Delta R/R_0$ between -0.7V to -1.7V (sweep rate : 10 mV/s). Wave C1 and exponential current C2 correspond respectively to the reduction of protons and water into molecular H_2. Drop in the relative reflectivity on negative potential sweep at ~ -1.4V is due to H_2 bubbles. (b) Corresponding relative variation of $\Delta H_c/H_c^0$, (c) $\Delta M_s/M_s^0$ as a function of applied potential. Arrows in each panel show the direction of the potential sweep.

Chapter 5. Domain wall propagation study with MOKE microscopy

5. 1. Introduction

As an extension of the previous chapters, a magnetic domain wall propagation study is investigated on the sputter-deposited Co/Pt in contact with the electrolyte by using MOKE microscopy. Since magnetic anisotropy energy (MAE) is closely related to the DW velocity [22], DW velocity dependence on applied potential study would be related to the voltage control of magnetic anisotropy (VCMA). Previous work of our group from A. Lamirand et al. [42] investigated magnetic domain wall propagation study on the Co (~0.8 nm)/Pd/Au/Si(111) sample in the electrolyte which has the PMA. Firstly, this work showed that DW motion is in the creep regime (the principle is described in Chapter 2) and DW velocity varies exponentially with the electric field (i.e., EFE on magnetic anisotropy energy). Sample with the Pd substrate also showed HER effects on H_c. However, HER effects on magnetic properties are reversible unlike the case of Pt substrate which has been shown in the previous chapters. Furthermore, HER effects are suppressed by introducing a short potential pulse. A similar potential program used for Co on Pt substrate in this thesis didn't suppress HER effects.

In this chapter, samples from SPINTEC (same as in Chapter 4) are used. Firstly, magnetic creep behavior in the air (with AlOx) and in the electrolyte will be shown. Then, DW velocity dependence on applied potential including the HER range will be studied. As we have already shown in the previous chapters, HER induces irreversible changes in magnetic properties. Therefore, controlled HER pulses are introduced to investigate effects on DW motion. Additionally, magnetic nucleation density variation after HER will be studied which is related to DW pinning energy distribution.

5. 2. Magnetic domain wall (MDW) propagation regime

Samples were first investigated in the air. Figure 5-1a shows a MOKE image of an AlOx/Co ~0.69nm/Pt 3nm/Ta 3nm/SiOx/Si (111) sample in air. The sample is initially saturated giving a dark gray uniform image by applying $H_{sat} = -30\text{mT}$ for 0.1s. The application of a first pulse of H-field ($N_{nuc} = +17\text{mT}$ for 3ms) induces the nucleation of an inverted magnetic domain (light gray domain #1 in the image). This domain then grows upon the application of

3 successive pulses of *H*-field ($H_{prop} = 15\text{mT}$ for 10ms). The sample is imaged after each pulse and the crowns #2 to #4 around the central spot #1 show the radial expansion of the initial magnetic domain. The domain wall velocity is estimated as $v_{DW} = \frac{\Delta x}{\Delta t}$ where Δt $(10ms)$ is the pulse length and Δx is the average distance travelled by the domain wall during one pulse. Figure 5-1b shows a MOKE image of the sample in contact with the CO-saturated electrolyte (pH 3.5) by applying potential $U_{rest} = -0.8\text{V}$ (AlOx is dissolved, see Figure 5-7 in appendix). $H_{sat} = -30\text{mT}$ for 0.1s, $H_{nuc} = 17\text{mT}$ for 1ms and $H_{prop} = 9\text{mT}$ for 3ms.

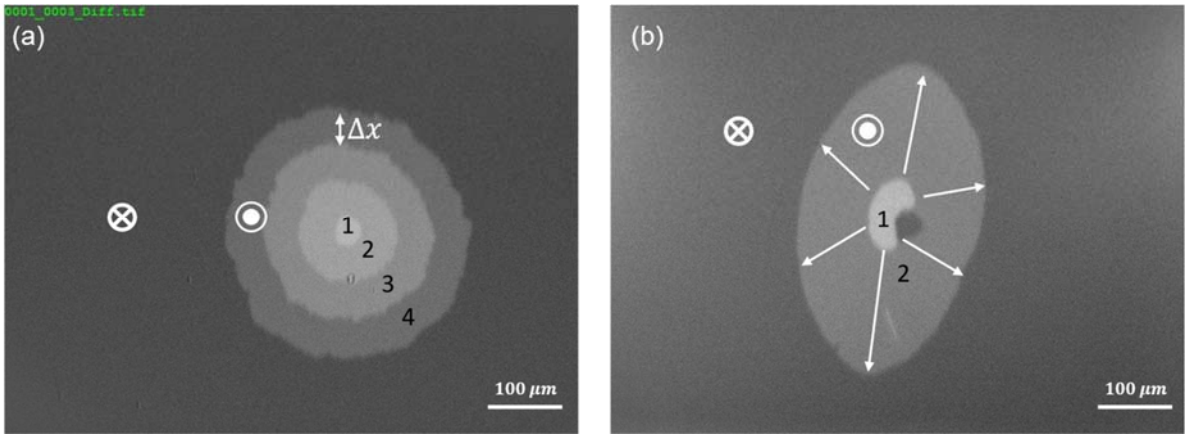

Figure 5-1 (a) MOKE image obtained by overlaying images of magnetic domain propagation (#2-#4) from the nucleation (#1) by gradation (outward propagation from the brightest nucleation spot). Sample is in Air condition (i.e. AlOx/Co ~0.69nm/Pt 3nm/Ta 3nm/SiOx/Si). (b) Same procedure of the sample in contact with the electrolyte (i.e. EL/Co ~0.69nm/Pt 3nm/Ta 3nm/SiOx/Si). The image size is 765.6 μm × 572 μm.

As an extension of Figure 5-1, the logarithms of the MDW propagation velocity are plotted as a function of $H_{prop}^{-1/4}$ in Figure 5-2 in each condition. Straight lines are found, which indicates that DW propagation occurs in the creep regime in these conditions [69], [124]. The creep regime is a thermally activated process where the DW velocity v_{DW} follows the law:

$$\boldsymbol{v_{DW} = v_0 exp\left[-\frac{U_c}{kT}\left(\frac{H_{prop}}{H_{dep}}\right)^{-1/4}\right]}$$

where U_c is related to the height of the disorder-induced pinning energy barrier. H_{dep} is the depinning field. v_0 is a numerical prefactor.

After immersion of the sample into the electrolyte and complete removal of the oxide layer,

v_{DW} remarkably increases for any given value of H_{prop}. For instance $v_{DW} = 0.18\mu m/s$ in air and increases by a factor of 30000 ($5.66 \times 10^3 \mu m/s$) for $H_{prop} = 5mT$ ($H_{prop}^{-1/4} = 0.67$). However, the absolute value of the slope also decreases from 26.94 to 9.47. These changes suggest a primary modification of the energy landscape at the Co/electrolyte interface.

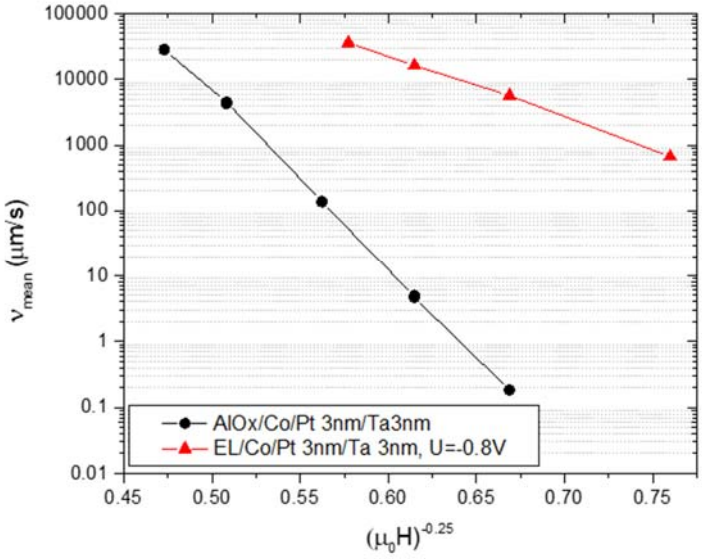

Figure 5-2 Plot of the logarithm of the DW velocity versus $H_{prop}^{-1/4}$ derived from the result of Figure 5-1. The linear relationship shows that the sample having the composition of AlOx/Co ~0.69nm/Pt 3nm/Ta 3nm/SiOx/Si (black) and electrolyte/CO/Co ~0.69nm/Pt 3nm/Ta 3nm/SiOx/Si are in the creep regime (red).

5. 3. Potential dependence of the domain wall propagation

Since the impact of HER on magnetic properties is "cumulative" (see previous chapters), a specific procedure was employed to minimize the influence of the sample history on the potential dependence of v_{DW}. We used the magnetic field and potential pulse profiles depicted in Figure 5-3a. It is important to notice that the sample is always imaged at $U_{rest} = -1.0V$ where the HER rate is not too large and where the CO-covered Co layer does not dissolve. A reference image is first recorded after the application of one nucleation pulse ($H_{nucl} = 33mT$, duration: 10 ms) to create inverted domains. A propagation pulse ($H_{prop} = 28mT$) is then applied and it is synchronized with the potential pulse (from -1.0 V to *U*). Synchronized propagation pulse (field and potential) is applied in different times depending on the evolution

of v_{DW}. The sample is again imaged at -1.0 V. The difference between the two images allows for measuring v_{DW} at the potential *U*. The procedure is repeated for different values of *U* as plotted in Figure 5-3b. The black and red data points correspond to a first and second set of measurements, recorded sequentially. Figures and arrows in the figure explain the sequence of measurements. The first point of each data set is the one at $-1.0\mathrm{V}$. The two plots present a sort of U-shape with a minimum close to -1V. The amplitude of variations is similar – if one considers the common potential range [-0.65 V to -1.3 V]. Nevertheless, there is an irreversible increase of v_{DW} at -1 V from 17.9 μm s^{-1} (data point 1) to 49.5 μm s^{-1} (data point 15) after the first set of measurements. This increase is promoted by measurements at potentials $<$ -1.0 V since it was checked that v_{DW} $(U = -1.0\mathrm{V})$ remains constant as long as the potential remain $U > -1.0$ V. However, one may notice that $v_{DW,14}$ $(-1.3$ V$) \approx$ $v_{DW,15}$ $(-1.0$ V$)$ where the subscript refers to the data point number. This is the first indication that promoting the HER on the Co/Pt sample irreversibly increases v_{DW}. This behavior is clearly different from the one of Co/Pd layers for which no irreversibility was reported [42].

By contrast, the increase of v_{DW} at potentials $U > -1.0$ V is a true potential-induced effect similar to the one reported with Co/Pd layers [42]. The amplitude of the effect is, however, smaller here: it is only ~ 1.12 decades/V i.e. in the potential range -1.0 to -0.6 V (between data points 1 and 8), and ~ 0.80 decades/V (between data points 15 and 19). In the case of Co/Pd, the changes are larger (~ 2.5 decades/V) [42]).

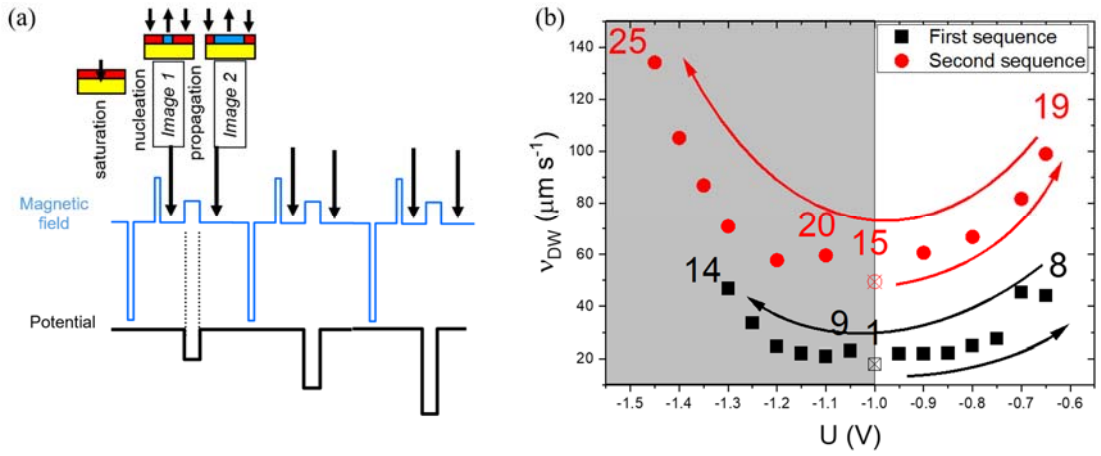

Figure 5-3 (a) Magnetic field (blue) and potential (black) pulse profiles to study potential dependence on MDW propagation. Note that MOKE images are always recorded at the same potential of -1.0 V. A negative pulse of a magnetic field is used to saturate the sample. A positive pulse of H field is applied to nucleate inverted domains. DW propagation is measured at -1.0V after the application of synchronized pulses of H_{prop} and U. (b) Potential dependence of DW velocity. Numbers on each point indicate the order of the measurement. The first experiment sequence (black symbols) starts from -1.0 V to -0.75 V, then from -1.05 V to -1.3 V (see directions of black arrows). The second cycle (red symbols) starts from -1.0 V to -0.65 V, then from -1.1 V to -1.45 V (red arrows). The Gray region indicates the region of HER (< -1.0 V). Initial points are open symbols.

5. 4. Hydrogen evolution reaction effect on magnetic domain wall propagation

To disentangle the influence of applied potential and HER on v_{DW} at potential < -1.0 V, the following experiment has been conducted. In the experiment described in Figure 5-4, we applied 8 potential pulses between -0.8 V and U_{HER} (0.1 s with 5s off time, see the red profile above the MOKE images) and applied a magnetic field pulse to nucleate inverted magnetic domains ($H_{nuc} = 48$mT for 0.04s). A total of 3 pulses of magnetic fields ($H_{prop} = 40$mT ; 0.5s) is applied to propagate the DW (see blue magnetic field profile on top of the figure). A MOKE image is recorded after each pulse. Note that DWs are created and propagated at $U_{rest} = -0.8$V. This procedure is used to ensure that observations are only impacted by the HER. Ideally, we should have used a fresh sample each time, which is not only time-consuming but would also hamper a meaningful comparison of measurements at a different potential.

This is why to reduce as much as possible the influence of sample history, we only show data where HER is not too strong (here U_{HER} is restricted to potential > -1.3V) and apply only 8 voltage pulses.

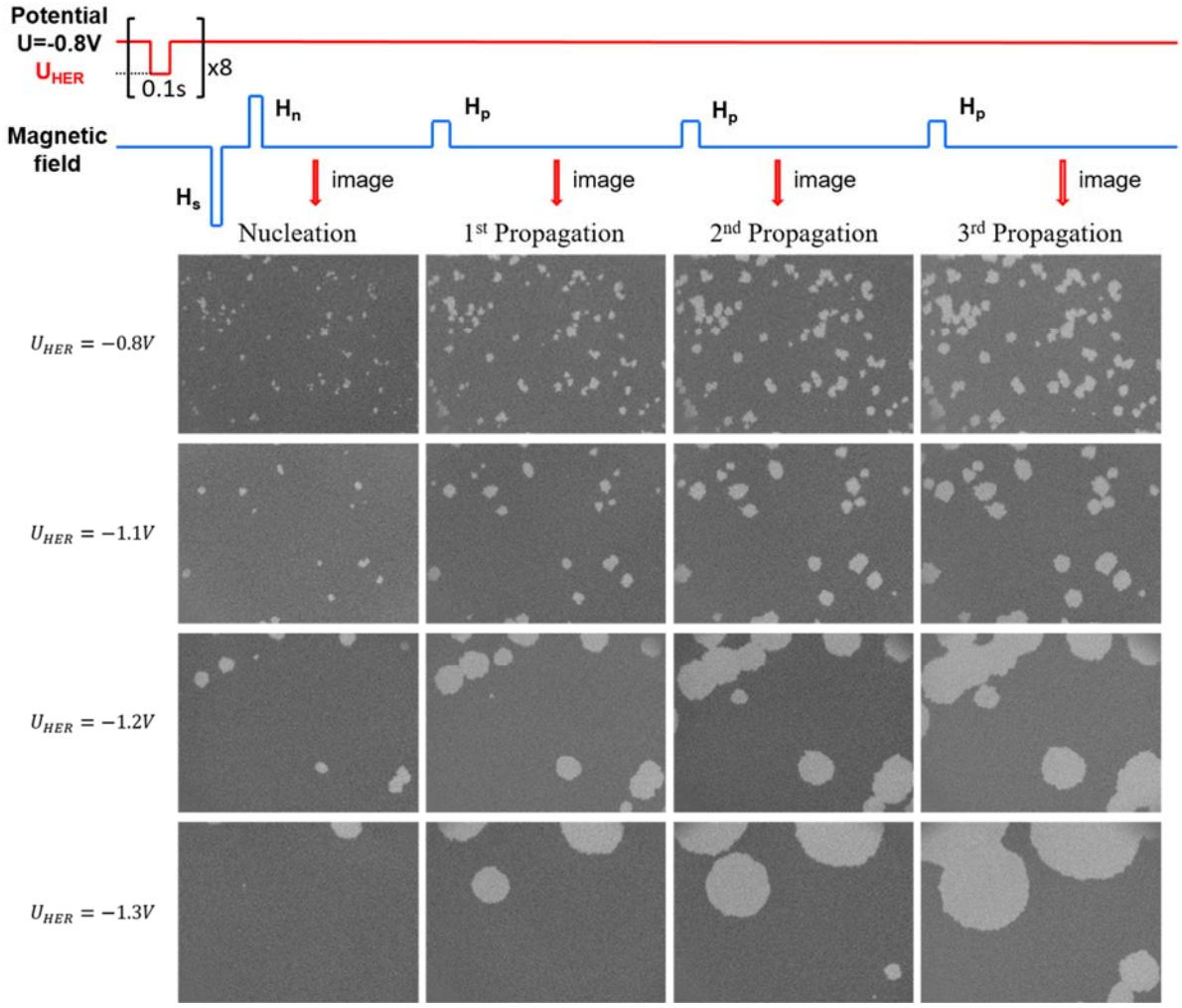

Figure 5-4 MOKE images obtained after applying 8 times of U_{HER} on Co~0.88nm/Pt 20nm/SiOx/Si sample in the CO saturated standard solution. U_{HER} varies from -0.9V to -1.3V with the interval of 0.1V (We present here only results after application by using -0.8V/-1.1V/-1.2V/-1.3V pulse amplitudes U_{HER}). Duration of U_{HER} pulse is 0.1s each. DWs are propagated and MOKE images are acquired at $U_{rest} = -0.8$V (see the potential profile on the right). Parameter: Saturation: $H_{sat} = -48$mT for $0.3s$, Nucleation: $H_{nuc} = 48$mT for $0.04s$, and Propagation: $H_{prop} = 40$mT for 0.5s (see the magnetic field profile on the top).

The MOKE images in Figure 5-4 highlight several effects.

- Looking at the first column, one sees there is a modification of the surface density D of inverted domains (see 1st column). Figure 5-5a shows the variations of D with potential.

There is a large decrease of D when $U_{HER} < -1.1\text{V}$. Data at $U_{HER} = -0.8\text{V}$ is not fully saturated because of the coil magnet heating problem (applied voltage to induce magnetic field reaches the maximum often). Therefore, nucleation density drop occurs after the application of $U_{HER} < -1.1\text{V}$.

- Looking at the next columns, one further notices an increase of the DW velocity as soon as $U_{HER} \leq -1.0$ V as shown in Figure 5-5b. However, v_{DW} stays essentially unaffected if U_{HER} remain above this critical value. $v_{DW} \approx 6$ μm s^{-1} for U_{HER} in the range [-0.8V to -1.0V] while v_{DW} progressively increases up to 91 μm s^{-1} if $U_{HER} \leq -1.3$ V). Note that the modification is *irreversible* since v_{DW} is always measured at -0.8V.

A subtler effect concerns the systematic change of the contrast in images along with the experiment. These are presented in Figure 5-5 where we plot the image contrast ($\Delta\text{Contrast}$) as a function of potential. Firstly, MOKE images are normalized by each saturation image to compensate for light drifts. Then, it is measured by subtracting gray values of two magnetically saturated regions (near magnetic domain walls) in the opposite direction. The plot shows that the average of $\Delta\text{Contrast}$ (3 different magnetic domain walls) starts to decrease dominantly after applying $U_{HER} < -1.3\text{V}$. $\Delta Contrast$ reduces 6% from its initial value.

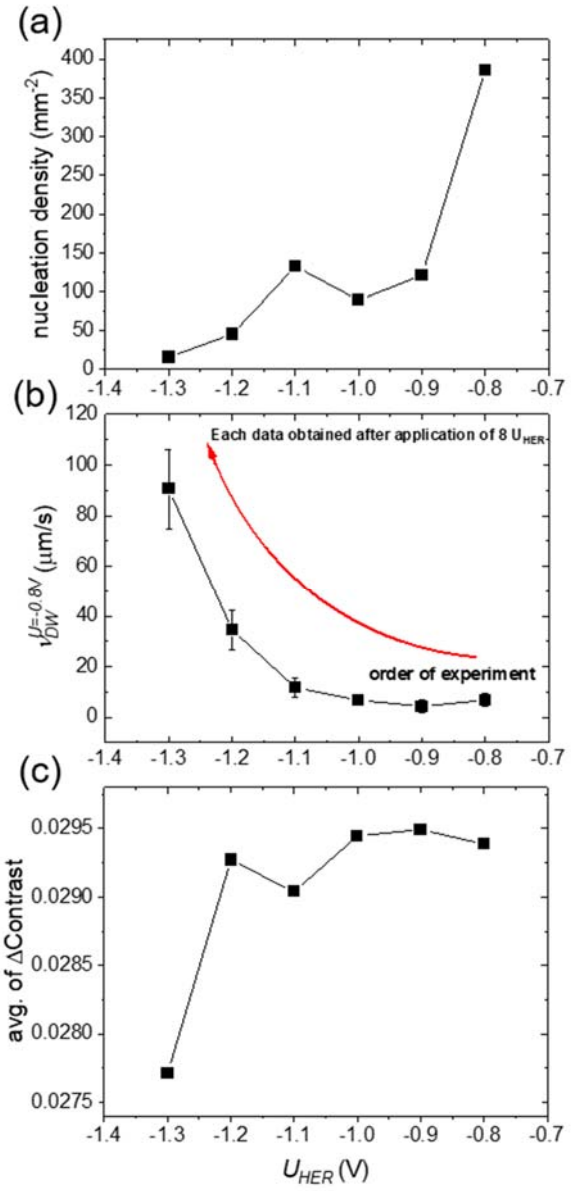

Figure 5-5 Parameters derived from the analysis of MOKE images in Figure 5-4. (a) Nucleation density (mm^{-2}), (b) DW velocity, and (c) the average of ΔContrast acquired from 3 different magnetic domains.

The MOKE microscopy experiment was reproduced using the *in situ* PMOKE setup to measure complementary magnetic parameters. Figure 5-6 shows the variations of magnetic parameters after the application of 8 HER pulses of different amplitudes (U_{HER}). The sequence of data acquisition is the same as in Figure 5-5. Figure 5-6 shows the variations of the saturation magnetization and of the remanence (M_S and M_r, panel a), coercive field (H_c, panel b) and EFE slope (Γ, panel c). We recall that Γ is the slope $\frac{\Delta H_c/H_c^0}{\Delta U}$ measured upon scanning the

potential between -0.9V to -0.7V. Results show that all characteristic parameters stay constant as long as $U_{HER} > -1.0\mathrm{V}$. Below the critical value $U_{HER} = -1.0\mathrm{V}$ they all start to decrease. Note that layer remains strictly perpendicularly magnetized since $M_r/M_s \sim 1$. These behaviors are consistent with the results of previous chapter. The amplitude of variation is only smaller because a small number of pulses were applied. It is particularly remarkable that MOKE imaging reveals important changes (nucleation and propagation of magnetic domains) although the changes of M_S, H_C and Γ remains rather small.

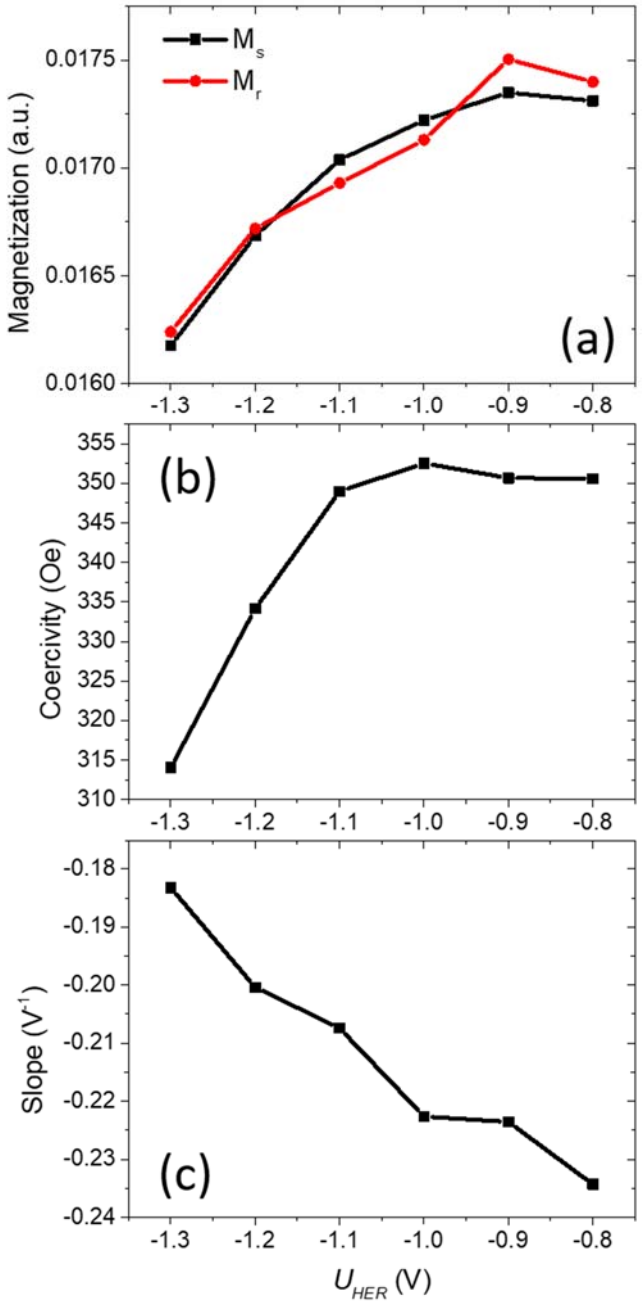

Figure 5-6 Mimic experiment of Figure 5-5 by using *in situ* PMOKE setup. (a) the saturation magnetization (black) with remanence (red), (b) Coercive field, and (c) derived electric field effect (EFE) slope variations after applying 8 HER pulses of different amplitudes. EFE slope is derived from $\Delta H_c/H_c^0$ as a function of the applied potential in the range of [-0.9V, -0.7V]. The sample is a sputter-deposited sample having AlOx/Co 0.69nm/Pt 20nm/SiOx/Si before immersing in the electrolyte.

5. 5. Appendix

Dissolution of the capping layer

The sample is immersed as explained in Chapter 4 and it was verified that the AlOx was dissolved by applying a short pulse of potential (0.1 s with $U_{HER} = -1.3\text{V}$) while the sample is immersed in CO saturated standard solution (pH 3.5). We recall that the rest potential is $U = -0.8\text{V}$. Figure 5-7 shows the transient current density recorded during one pulse. (The pulse is applied from $2s$). The red plot is the current transient measured in the MOKE microscope cell. The current density reaches $-3.7\ \text{mA/cm}^2$ and saturates around $-2.5\ \text{mA/cm}^2$, which is close to that measured on an electrodeposited Co layer. This confirms that the AlOx layer has been dissolved.

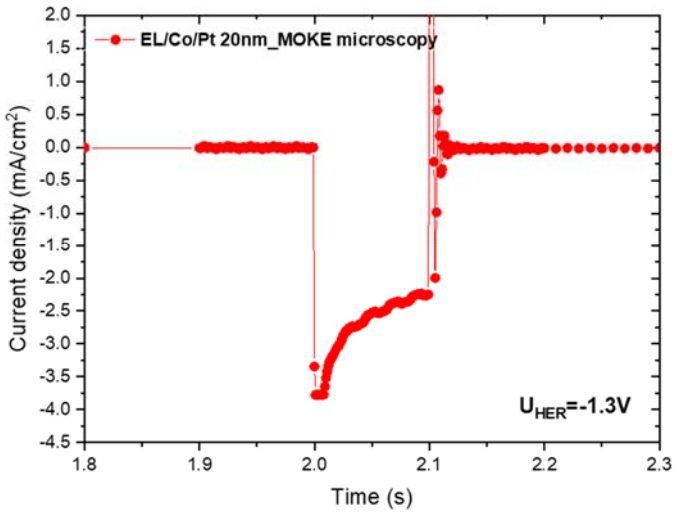

Figure 5-7 Transient current measured during the application of a potential pulse with $U_{HER} = -1.3\text{V}$ for 0.1s (rest potential is -0.8V and the pulse is started from 2s). The sample has the composition of EL/Co ~0.81nm/Pt 20nm/SiOx/Si.

Influence of defects on magnetic domain nucleation

To investigate a possible influence of defects in the film on magnetic domain nucleation (after application of 8 potential pulses in different U_{HER}), magnetic domain saturation-nucleation protocol was repeated 6 times (without applying new potential pulses) and the positions of the domains were correlated between each nucleation and the others. The first image of sequences presented in Figure 5-4 corresponds to the last nucleation step. As above, the nucleation condition is fixed as $H_{nuc} = 48\text{mT}$ for 40ms. Figure 5-8 shows an example of

6-stacked nucleation MOKE images in the case of potential pulse with $U_{HER} = -1.2\text{V}$. The number of domains appearing in the same region is distinguished by the color scale bar next to the plot, i.e. yellow nucleated regions correspond to regions where the domains appeared once in 6 nucleation images. Figure 5-8b shows the regions where nucleation took place more than two times.

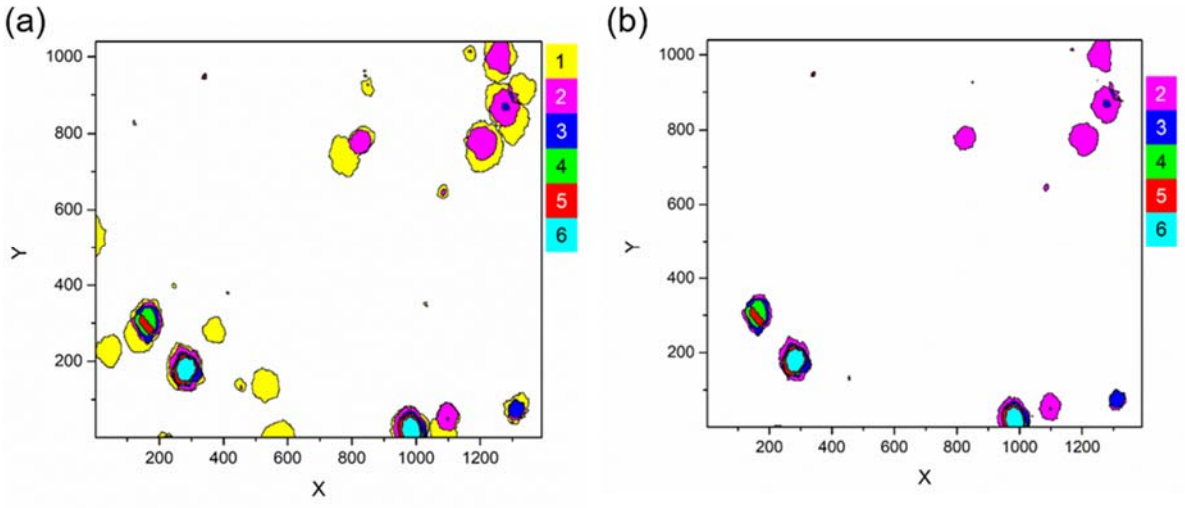

Figure 5-8 Consistency study of magnetic domain nucleation. (a) Overlaid 6 nucleation MOKE images after applying 8 $U_{HER} = -1.2\text{V}$ pulses. Color scale represents the number of appearances in 6 nucleation images, i.e. yellow nucleated domains are shown once in 6 nucleations. (b) Filtered image showing domains that appeared more than twice.

In Figure 5-9, we plot the proportion of regions with one nucleation (red points) and that with 2 nucleations or more (black points). Except for $U_{HER} = -1.3\text{V}$, the proportion of regions where nucleation took place twice or more is significantly larger than that with a single nucleation event. This suggests that nucleation is often dominated by physical defects in the film. At $U_{HER} = -1.3\text{V}$, this tendency seems the opposite as if the probability of nucleating at the film defects decreased upon applying HER pulses at this potential. This might be due to a healing effect or to the general decrease of the film anisotropy which makes nucleation at these high nucleation fields more random.

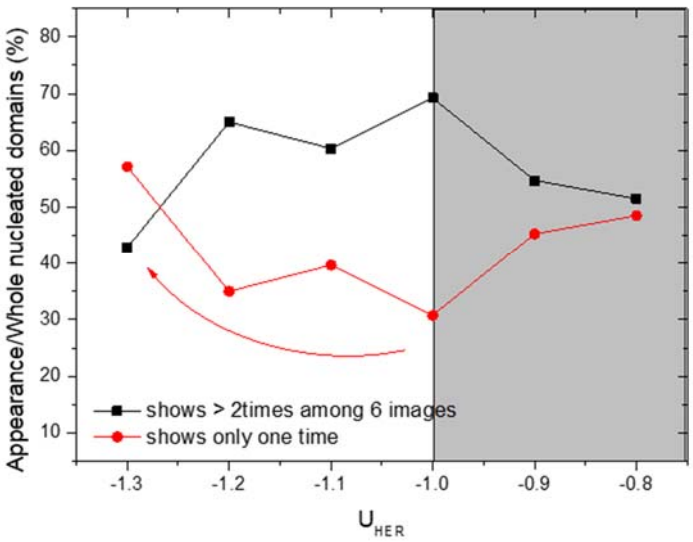

Figure 5-9 Appearance ratio from whole nucleated domains. Black data shows nucleated domains which appear more than 2 times among 6 nucleation images. Red data shows only one time among 6 nucleation images.

Chapter 6. General Discussion

6. 1. Introduction

In this chapter, we aim at conducting a global discussion of the experimental result presented in previous chapters. Because the effects evidenced in these chapters are all related to the reaction of hydrogen evolution (HER), this chapter starts with a survey about the H-incorporation within materials.

The influence of the hydrogen on the sample having Co/M (M= Pt, Pd, Ni, Ru) interfaces was investigated by many groups showing the reduction of its PMA or spin reorientation transition (SRT) [37], [38], [125]–[127]. The PMA was initially thought to be the result of $3d-4d$ or $3d-5d$ interface magnetocrystalline contributions that overcome the classical magnetostatic dipolar energy [128]–[131]. Especially in the works of S. M. Valvidares et al. [37], PMA is suppressed if Co is grown on H covered Pt surface. K. Klyukin et al. [38] did DFT calculations and showed that PMA decreases with increasing H concentration at the interface between Co and Pd.

Even though Co-H bond strength is lower than Pt-H, and HER exchange current density on Co is 100 times lower than on Pt, Co-H bond has a non-negligible probability to form. Furthermore, CO on the surface of Co affects HER reaction suggesting that it affects H adsorption [132], [133]. Therefore, the HER influence on the Co magnetic properties may also originate from the presence of HER induced H inside the Co film. Xinlong Ye et al. and the part of the work of K. Klyukin et al. investigated the H influence on Co magnetic properties. In these works, variations of magnetic parameters (PMA, magnetic moment, M_S…) are similar to the case when the hydrogen is interacting with Pt layer. Xinlong Ye et al. show that reduction of the coercivity is due to the decoration of the grain boundaries with hydrogen atoms [134]. In one work with the Co/Pd alloy films, hydrogen evolution results in the reduction of coercivity as well as the increase of the magnetic domain wall velocity. The increase of the DW velocity is due to the decrease of the activation energy (E_A) for the magnetization reversal with the presence of hydrogen atoms in the grain boundary and atomic interstitial space [135].

In the following, we start by correlating the HER and H absorption into metals. Then, we make a summary of the pristine magnetic state upon forming the EL/Co/Pt interface. The HER study will be discussed in a bottom-top manner to extrapolate the MOKE microscopy result (accumulated charge is up to $\sim -1.3\mathrm{mC}$). Then, magnetic behaviors after HER pulses are

generalized and discussed. The main discussion is to propose the origin/hypothesis of HER effects.

6. 2. H-absorption into metals

The H-absorption reaction (Eq. 2.20) is a side reaction of HER. It is well-known that it occurs at Pd electrodes, where up to 70% of H (with respect to Pd atoms) may be incorporated (β-phase) [136]. More generally it occurs at metals prone to the formation of hydrides, in particular the iron group metals may incorporate atomic H [57], [58]. The process occurs also at Pt electrodes. This has been shown in the first works by permeation studies on Pt membrane [137]. More recent work on Pt nano and microparticles showed that H absorption in Pt is only observed if the particle size is of few nanometers [114].

It should be noted that a priori, a large fraction of electrons are used to reduce H^+ into H_2 molecules and that only a very small fraction leads to H-absorption. For a given metal, the partition between the two pathways is known to depend on the HER conditions (pH, possible adsorbates) [138].

Experimentally, we saw in Chapter 3 that the relative reflectivity $\Delta R/R_0$ of a bare Pt electrode changes for potentials < -1.0 V in a CO-saturated solution (see Figure 3-10**).** The application of voltage pulses ($U_{HER} = -1.6\text{V},\ 0.1\text{s}$) produces a similar effect. These changes may be considered as a manifestation of H-absorption within Pt. Figure 6-1**a** shows that $\Delta R/R_0$ decreases with increasing HER charge q_{HER}. This is most probably due to the change of the refractive index of the Pt layer induced by H absorption. The amplitude of the decrease depends on the presence of the CO-adlayer. In absence of CO, the decay of $\Delta R/R_0$ is rather small (< 1%). In the presence of a CO-adlayer (green data points), $\Delta R/R_0$ decreases continuously upon application of HER pulses up to ~6%. This value is actually not negligible if one considers that the contribution of the Pt layer to the sample reflectivity is about 18%. We assign the amplitude difference to the fact that, in the absence of CO, the inserted H is re-oxidized into protons (inverse of reaction **2.19**) and gets out of the Pt when the potential is above -0.8 V. This is a well-known reaction at bare Pt [116]. The behavior of the CO-covered surface suggests that the absorbed hydrogen is trapped within the Pt with the potential program used in the experiments. To release the inserted atomic H, one needs to apply a potential more positive than the rest potential. The effect of a CO adlayer on H-trapping has been also reported with Pd electrodes [139], [140]. In the case of Pd, a saturation of the reflectivity was clearly observed

when no more H can be accommodated in the Pd layer. We didn't observe any saturation in the case of Pt electrode and it is not clear why.

Figure 6-1b shows that the decay of $\Delta R/R_0$ observed at Co/Pt electrodes is similar to that observed a bare Pt electrode. Obviously, the presence of an ultrathin Co layer has no significant impact on this process. This demonstrates that the decay of $\Delta R/R_0$ observed during the application of HER pulses is mainly related to the presence of the Pt substrate and that it is not corresponding to a sizeable loss of cobalt. As further proof, we note in passing that such decay of $\Delta R/R_0$ upon application of HER pulses was not observed with Co/Au(111) samples [13].

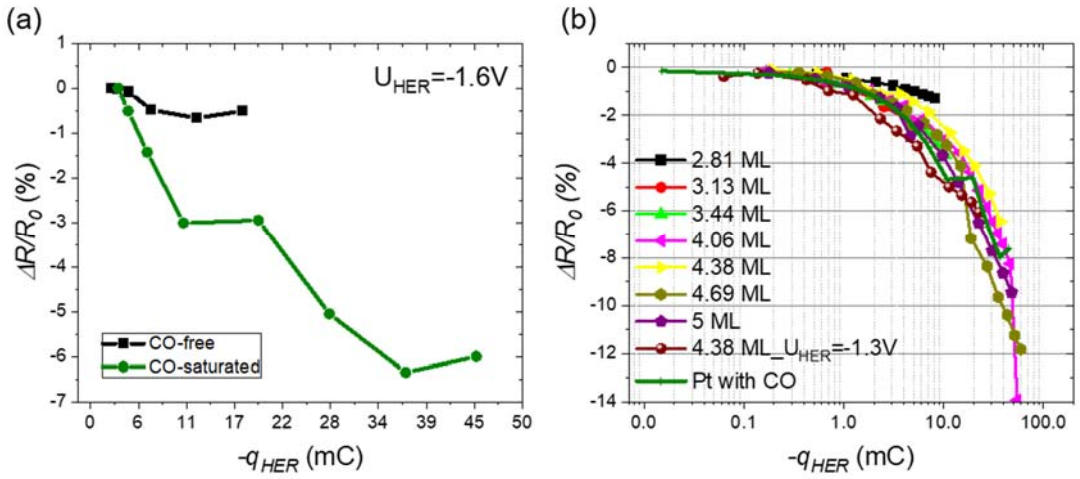

Figure 6-1 Plots of $\Delta R/R_0$ as a function of cumulated HER charge ($-q_{HER}$). (a) Pt electrode in the CO-free (black symbols) and CO-saturated (dark green symbols) solution of pH 3.5 by applying $U_{HER} = -1.6\text{V}$ for 0.1s. (b) Co/Pt electrode in CO-saturated solution of pH 3.5. The different symbols correspond to different Co thicknesses in the range 2.6-5 ML. The dark green line corresponds to a Pt electrode in the same conditions (same as the left figure).

6. 3. Magnetic changes

From the previous chapters, we have seen that all types of samples, with a Co thickness in the range of 1.6 to 3.8 ML, are perpendicularly magnetized after CO-adsorption. Note that we now refer to the *corrected* thickness for sputtered layers, because we have seen that about 1.2 ML of Co have been lost (magnetically speaking) between the sputtering step and the immersion step of the sample (Figure 4-5). This Co that does not contribute to the film magnetization may be at the interface with Pt and/or at the interface with AlOx where the Co

atom may be partly oxidized and dissolve upon immersion in the electrolyte. Table 6-1 shows the magnetic property of electrodeposited and sputtered samples which will be mainly discussed in this Chapter. They have similar magnetic properties.

Table 6-1 Magnetic property of electrodeposited and sputtered samples before application of HER pulses (sample substrates are Pt 3nm/Ta 3nm). The thickness of the later is the nominal value corrected for 1.2 ML.

Sample	Thickness (ML)	M_s	H_c (Oe)	Γ (V^{-1})
ED	2.2 ~ 2.7	0.11 - 0.13	280 - 370	-0.2 ~ -0.3
Sputtered	2.9 ~ 3.2	0.11	180 - 250	-0.3 ~ -0.36

6. 3. 1. Influence of applied potential (-1 V $< U < -0.7$ V)

This section is restricted to the discussion of the influence of the applied potential outside the HER regime (i.e. $U > -1$ V) and for pristine samples covered with a CO-adlayer (i.e. prior to application of any HER pulse), either right after electrodeposition for *in situ* prepared Co layers or after immersion for sputtered samples.

As long as $U >$ -1.0 V, the variations of $\Delta H_C/H_C^0$ are linear and reversible with a slope $\Gamma \approx -30$ $\%V^{-1}$ $(= -0.3$ $V^{-1})$ for both types of samples (see Figure 3-6b and Figure 4-4b). This value is nearly independent of the Co thickness within the thickness range considered (Figure 4-6). In the work of A. D. Lamirand et al., the derived slope shows $\Gamma \approx -25\%V^{-1}$ in the case of ~0.8nm Co/Pd/Au/Si sample [42]. In this same potential range, the DW velocity v_{dw} is an exponential law of the applied potential. This can be derived from the creep law (from Eq. 2.28):

$$\ln v_{DW} = \ln v_0 - \alpha H_{prop}^{-1/4} \qquad 6.1$$

Where we assume that the coefficient α is proportional to the magnetic anisotropy $\alpha(E) = \frac{U_c}{kT} H_{dep}^{\frac{1}{4}} = \alpha_0 K_{MAE}(E)$, α_0 contains different micromagnetic parameters. Since $K_{MAE}(E) = K_v + \frac{K_s + \beta E}{d_{Co}}$ where β is the EFE coefficient, i.e., the variation coefficient per Vm^{-1} of K_s^{Co-EL} (surface anisotropy of Co/electrolyte interface), $\ln v_{DW}$ is linear with K_{MAE}. Eq. 6.1 can thus be written:

$$\ln v_{DW}(U) = \ln v_0 - \alpha_0 H^{-\frac{1}{4}} [K_V + \frac{K_s + \beta U/\delta_c}{d_{Co}}] \qquad 6.2$$

Where $\delta_c \approx 0.14\text{nm}$ is the distance between the Co surface and the plane of counter cations at the CO-covered cobalt surface [41], [42]. Figure 6-2 shows $\ln v_{DW}$ as function of $U_{propagation}$. (data originating from Figure 5-3b). The derived slope from Figure 6-2 which is linear with β correspond to 2.58 (black, first sequence) and 1.84 (red, second sequence) respectively. Therefore, one can deduce that $\alpha_0\beta$ is reduced from the first sequence to the second sequence, but it is difficult to determine which of the two parameters α_0 and β is the one that decreases the most, since we observe that the domain nucleation density is also changing significantly during the experiment. In the work of A. D. Lamirand et al., derived β corresponds to $\sim 34\text{fJ/Vm}$ which is expected to be similar in this case since used solution is exactly the same and the Co thickness is similar. Compared with previous studies in different systems, our sample clearly has the benefit in terms of the voltage controlled magnetism since the voltage-induced H_c changes in $\text{AlOx/Co}\ 0.8\text{nm/Pt4nm}$ equal $\Gamma = 0.1\%\text{V}^{-1}$ [22] and those in $\text{HfOx/FePt}\ 2\text{nm/Pt/MgO}$ equal $\Gamma = \sim 7.5\%\text{V}^{-1}$ [2].

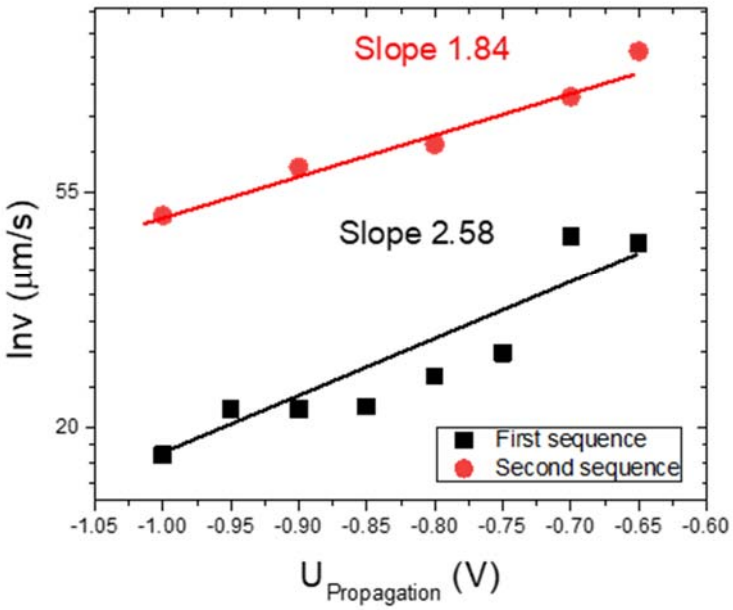

Figure 6-2 Rescaled domain wall velocity ($\ln v_{DW}$) as a function of the DW propagation velocity from Figure 5-3b. The potential range shown in this figure is out of the HER regime ($U_{HER} > -1.0\text{V}$). Straight lines are linear-fitted lines with derived slopes.

6. 3. 2. Influence of H-insertion ($U < -1$ V)

In this section we address the influence of the insertion of atomic H within the sample, i.e.

when the applied potential becomes < -1.0 V where the HER takes place.

We shall first discuss the MOKE imaging and P-MOKE data corresponding to the last experiments presented in Chapter 5, i.e. after 8 pulses at various potentials between -0.8 V and -1.3 V, because they offer a complete overview of the behavior of the system for a cobalt thickness of ~3.2 ML (Pt 20nm/SiOx/Si substrate). The data presented in Figure 5-5 and Figure 5-6 have been replotted as a function of q_{HER} because this parameter is expected to be directly related to the amount of absorbed H in contrast with the potential. In panel a Figure 6-3 we plot the variations of the density of inverted domains (black) and the v_{dw} (red). We plot the relative variations of the characteristic parameters in panels (b-d) knowing that their initial values are $M_S = 0.017\ (a.u), H_C = 350$ Oe, and $\Gamma = -0.23\ \mathrm{V}^{-1}$. In the charge range up to ~1.4mC, v_{DW} shows relatively strong change of more than a factor of ten while H_c and M_s reduced 6~10%.

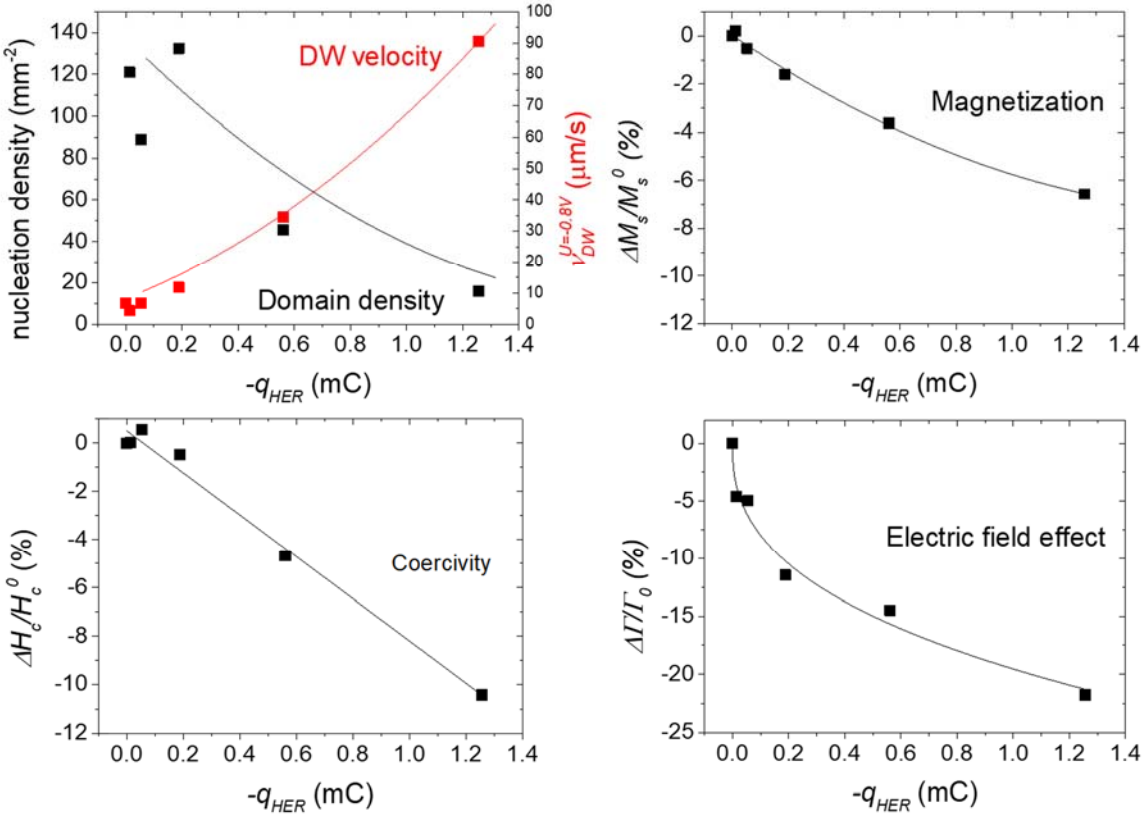

Figure 6-3 Magnetic parameter variations as a function of $-q_{HER}$ (mC) from Figure 5-5 & Figure 5-6. Each panel includes (a) nucleated domain density (black) and DW velocity variations, the relative variations of (b) M_s, (c) H_c, and (d) Γ.

To investigate the consistency of HER effects between previous results (Chapter 3, Chapter 4) and MOKE microscopy results (Chapter 5), MOKE microscopy mimic experiment with PMOKE (Figure 6-3) are extended by applying HER pulses with $U_{HER} = -1.6\mathrm{V}$. Figure 6-4 shows $\Delta M_s/M_s^0$, $\Delta H_c/H_c^0$, and Γ as function of cumulated charge (q_{HER}). Black is the extended result of the Figure 6-3 by applying $U_{HER} = -1.6\mathrm{V}$, red is the result from Chapter 3 having similar Co thickness ($\sim 2.5\mathrm{ML} \approx 0.5\mathrm{nm}$, after 1.2 ML correction) to black data. Gray region corresponds to the MOKE microscopy experiment range (experiment of Figure 5-6, the accumulated charge is up to ~$1.3\mathrm{mC}$). Even though they have different substrates (Pt 20nm or Pt 3nm / Ta 3nm), magnetic property variations upon HER pulses have the same tendencies: H_c & M_s reduces and Γ goes to zero. Therefore, we conclude that the changes in magnetic parameters determined from MOKE microscopy and those from PMOKE have the same origin, i.e., H absorption into Pt. Regarding MOKE microscopy observations, our results suggest that HER alleviates the fluctuation of the MAE energy landscape, in particular, the pinning centers controlling the DW propagation in the creep regime and magnetization reversal.

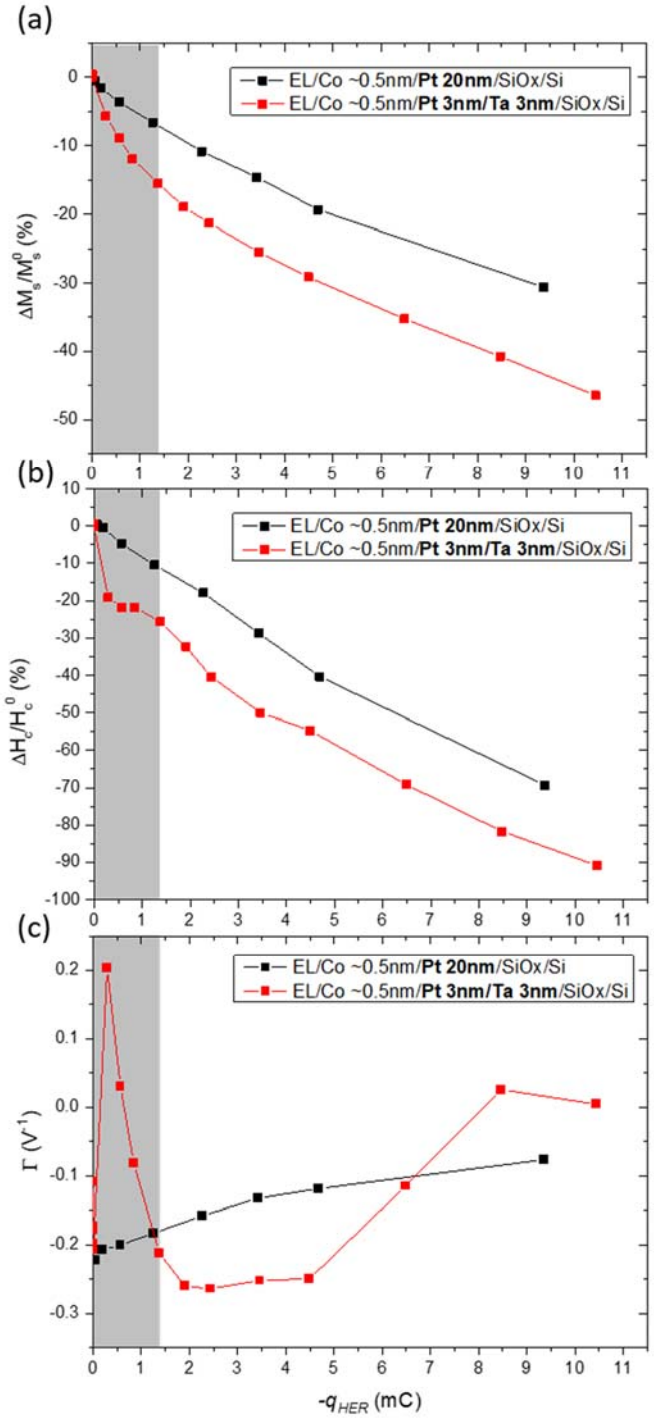

Figure 6-4 (a) $\Delta M_s/M_s^0$, (b) $\Delta H_c/H_c^0$, and (c) Γ variations as a function of cumulated charge ($-q_{HER}$) from different experiments having similar Co thicknesses. The black is the extended MOKE microscopy mimic experiment, the red is the result of the sputter-deposited sample having similar Co thickness (∼0.5nm, after 1.2ML subtraction) from the result of Chapter 4. Unlike MOKE microscopy and mimic experiment, constant HER pulses ($U_{HER} = -1.6\text{V}$) are applied on red data. Gray area corresponds to the MOKE microscopy experiment range (up to $\sim -1.3\text{mC}$).

In the following, we will try to estimate the changes of the different terms of the magnetic anisotropy energy induced by H. We will assume that H_c is proportional to K_{MAE} as in the Stoner-Wolfarth model considering a uniformly magnetized ferromagnet, and the coercive field (H_c) can be calculated as [141], [142]:

$$\boldsymbol{H_c = \frac{2K_{MAE}}{\mu_0 M_s}} \qquad 6.3$$

where K_{MAE} is the total magnetic anisotropy. Thus, the decrease of H_c that we observe should be related to a decrease of K_{MAE}. In Table 6-2, we present the main macroscopic magnetic parameters at different stages during HER treatment for a typical Co thickness of 0.5 nm.

Table 6-2 Magnetic property variations after 100 HER pulses with $U_{HER} = -1.6$V

Parameter	As prepared	After 100 $\boldsymbol{U_{HER} = -1.6V}$	Experiment
d_{Co} (nm)	~0.5nm	~0.5nm	Chapter 4. 5
K_v (J/m^3)	K_v^i	K_v^f (constant)	Assuming t_{Co} is conserved
M_s (a.u.)	M_s	$\sim 0.75 M_s$	Figure 3-9b & Figure 4-8a
H_c (Oe)	H_c	$\sim 0.8 H_c$	Figure 3-9a & Figure 4-8b
Γ (V^{-1}) or β (fJ/Vm)	Γ or β	0	Figure 3-9c & Figure 4-11 & Figure 6-2
K_{MAE}	K_{MAE}^i	K_{MAE}^f (reduced)	Figure 5-5

As shown in Figure 4-8, the effect of HER on M_S and H_c is large for the thinnest Co films and is significantly smaller for the thickest ones. This suggests that the HER effect is affecting the Co atoms at the interfaces. S. M. Vavidares et al. have indeed shown that incorporating H at the Pt/Co interface affects 1~2 ML of the Co by changing K_{MAE} [37].

The behavior of the electric field effect (Γ) variation is at variance since it doesn't depend a lot on thickness for Co layers thicker than 2.8 ML and converges to 0 in all cases. This variation means that Co surface state in contact with the electrolyte is also varying by HER potential pulses.

Let us see how these observations can be translated into constraints on macroscopic parameters. The magnetic anisotropy energy (K_{MAE}) variation after HER pulses can be rewritten as (derived from Eq. 2.31):

$$\Delta \boldsymbol{K_{MAE}} = \Delta \boldsymbol{K_V} - \boldsymbol{2\pi \Delta M_s^2} + \frac{\boldsymbol{\Delta K_s + \Delta \beta E}}{\boldsymbol{d_{Co}}}$$

$$\boldsymbol{\Delta K_s = (2\pi \Delta M_s^2 + \Delta K_{MAE}) d_{Co} - \Delta \beta E}$$

By putting variations of parameters from the Table 6-2 into the above equation, we can derive:

$$\Delta K_s = (-0.44 \cdot 2\pi M_s^2 + \Delta K_{MAE}) \cdot 0.7 \times 10^{-9}\ \text{m} + \beta \cdot E$$

In the case of Co, dipolar energy corresponds to $2\pi M_s^2 \approx 1.1 \times 10^6 \text{J/m}^3$ [13]. Furthermore, we can refer that the electric field effect coefficient β corresponds to $\sim 30 \text{fJ/V} \cdot \text{m}$ in the case of Co $\sim 0.8 \text{nm}$/Pd/Au/Si in the CO-saturated solution [20], [42]. $E = -0.8 \text{V}/0.14 \text{nm} = -5.7 \times 10^9\ [\text{V/m}]$ considering that the thickness of the electrochemical double layer is 0.14 nm. Then ΔK_s turns out to:

$$\Delta K_s = -3.4 \times \frac{10^{-4} \text{J}}{\text{m}^2} + \Delta K_{MAE} \cdot 0.7 \times 10^{-9} \text{m} + 1.7 \times 10^{-4} \text{J/m}^2$$

Since H_c decreases by 20 % upon applying HER pulses, ΔK_{MAE}<0 and is equal to $\sim -10^5 \text{J/m}^3$ (K_{eff} $\sim 5 \times 10^5 \text{J/m}^3$ derived from the Brillouin light scattering measurement for AlOx/Co/Pt) [121], [143]. Thus, $\Delta K_s = -2.4 \times 10^{-4} \text{J/m}^2$ which indicates the reduction of surface anisotropy either $K_s^{\text{Co-Pt}}$ or $K_s^{\text{Co-CO}}$ after application of HER.

General Conclusion

In this thesis, magnetic property dependence on the applied voltage is studied on the ultrathin ferromagnetic Co layer in contact with the electrolyte. Samples are prepared in two different ways: electrochemical epitaxial growth (Chapter 3)/magnetron-sputter deposition (Chapter 4 & Chapter 5). The Co/Pt samples in contact with the CO-saturated electrolyte have an out-of-plane magnetization (PMA). Magnetic properties are characterized by using the *in situ* polar Magneto-Optical Kerr Effect (MOKE) setup and MOKE microscopy.

Pristine samples after adsorbing CO showed the applied voltage dependence of H_c as well as of v_{DW}. The amplitude of the electric field effect in both cases is in agreement with electrodeposited Co layers on Pd/Au/Si(111) in contact with electrolyte [42]. In the case of H_c voltage dependence, $\Gamma = \frac{\Delta H_c/H_c^0}{\Delta U}$ is generally $20{\sim}30\%\mathrm{V}^{-1}$. Compared with solid state devices mentioned in the introduction of the thesis, our sample clearly has the benefit in terms of voltage-controlled magnetism (VCM).

However, irreversible magnetic property variations are shown after extending the applied potential to the HER regime: H_c, M_s, and Γ decreases continuously whereas the ferromagnetic Co layer remains stable. MOKE microscope results show that MAE and the magnetic domain nucleation density are reduced after HER. More specifically, HER effects are studied depending on Co thickness, HER pulse amplitude. Samples with thinner Co layer ($d_{Co} < {\sim}3ML$) are shown to be susceptible to degradation in H_c, M_s. However, Γ and reflectivity upon application of HER pulses seem to be independent of the Co thickness (follows general trends). The independence of Γ & reflectivity on Co thickness can support two hypotheses: Γ purely arises from Co surface state and the HER effects from the presence of Pt.

Throughout the results, HER induces a reduction in the surface anisotropy (K_s). This thesis has shown that this may relate to two sources: (i) one source of the K_s reduction comes from $K_s^{\mathrm{Co-Pt}}$ of the Co-Pt interface where hydrogen accumulates. (ii) the second source of the K_s reduction comes from $K_s^{\mathrm{Co-electrolyte}}$ of the Co-electrolyte interface where hydrogen may co-adsorb with CO and have an influence on the surface effect.

HER results in the magnetic moment quenching and the alleviation of pinning energy force which is a decisive contribution to the dynamic of the domain wall in the creep regime.

Therefore, we propose that the controlled HER pulse application can alleviate defect distributions resulting in the improvement on the dynamic of the DW propagation since defect creation is inevitable during the chemical/physical deposition process. Additionally, magnetic property tuning through interface modification through HER would be a method to design the low power consuming magnetic memory device since this thesis has shown that magnetic anisotropy is tunable conserving its PMA.

Perspectives

DW motion in a magnetic stripe

It has been often observed in the literature that DWs are pinned in magnetic stripes because of defects resulting from their microfabrication (lithography). The project is based on localized VCM to see if one can address this question. The idea is to have a magnetic stripe placed between two auxiliary Pt lines (Figure S. 1a). When the ensemble is immersed in the electrolyte under potential control (see above), applying voltage pulses between the magnetic strip and the auxiliary lines, generates an electric field which lateral extension onto the magnetic stripe depends on the pulse duration (Figure S. 1b). The idea is to confine the applied electric field in a region near the edges of the stripe, by adjusting the pulse parameters (duration and amplitude) to study whether one may reduce the influence of edge defects. Specific lithographed samples (Figure S. 1c-d) are provided by SPINTEC.

Figure S. 1c is the sample having the desired structure which is provided by the collaborator for testing. It is also required to have the specific sample holder (Figure S. 1d) to apply an electric field independently on each electrode.

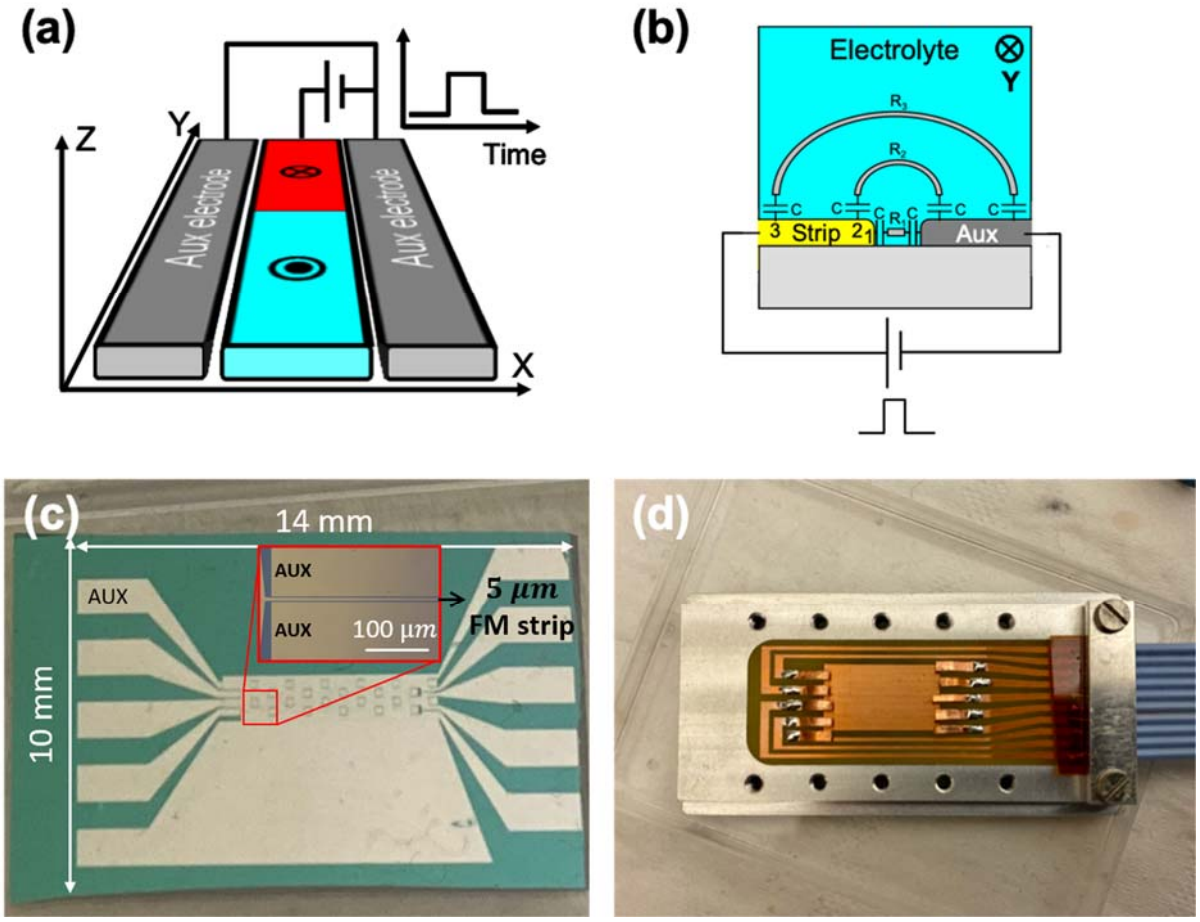

Figure S. 1 (a) Schematic of the sample showing the ferromagnetic strip surrounded by 2 auxiliary electrodes. (b) side view of the ferromagnetic strip and auxiliary electrode showing equivalent circuit where we confine electric field to control MAE (position 1). (c) deposited sample provided by SPINTEC. Inset shows a 40 times magnification of 5 µm width ferromagnetic strip surrounded by two auxiliary electrodes. (d) designed sample holder to apply electric field pulse individually (copper stripes)

Influence of applied potential on DMI (Dzyaloshinskii-Moriya Interaction) in the electrolyte

Due to the symmetry breaking of the interfaces, Dzyaloshinskii-Moriya Interaction (DMI) is found also in EL/FM/HM interface. DMI arises from broken inversion symmetry and spin-orbit coupling (SOC) [144], [145]. The sign of DMI decides the chirality of the Néel type DW. Upon application of an in-plane magnetic field (H_x) the domain propagation is asymmetric along the in-plane field direction indicating the presence of Néel type DW in our sample due to DMI in our system (Figure S. 2a,b). As investigated in previous works [146], [147], the variation of DMI upon application of voltage (as well as an electric field) was reported by

modifying the electrical state of FM interface. Since we have shown that DW velocity and the surface magnetic anisotropy depend on the applied potential, we expect the modification of DMI upon applied potential. Figure S. 2c shows DW velocity as a function of the in-plane field (H_x) where the DW was driven with the out-of-plane field of $H_z = 11\text{mT}$. Filled data shows DW propagation on the right side and unfilled data shows DW propagation on the left side. This figure shows asymmetric DW propagation. Furthermore, this opens a possibility that DMI increases with negative potential, similar to the work of Srivastava et al. [146]. For further study, *in situ* determination of the magnetic anisotropy energy is required.

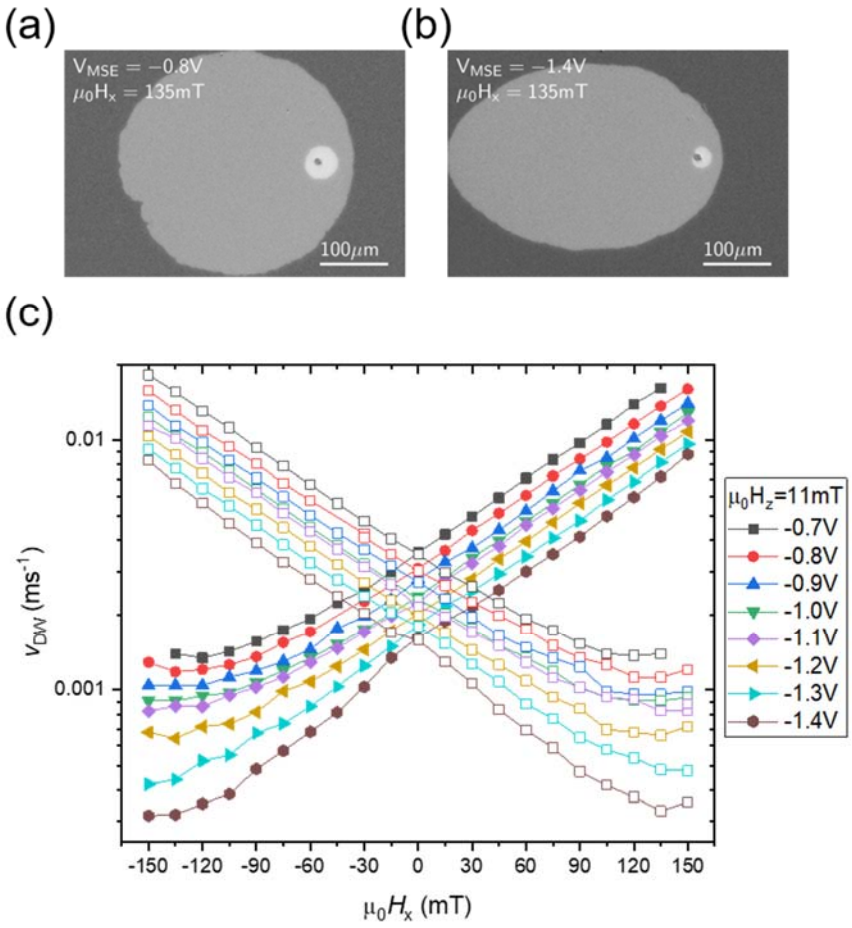

Figure S. 2 Asymmetric DW expansion MOKE images by applying out-of-plane magnetic field ($H_z = 11\text{mT}$) with in-plane magnetic field ($H_x = 135\text{mT}$) in different potential: (a) $-0.8V$, (b) $-1.4V$. (c) DW velocity as a function of in-plane field (H_x) where the DW was driven with out-of-plane field of $H_z = 11mT$. Filled data shows DW velocity on the right direction and unfilled data is on the left direction.

References

[1] C. Song, B. Cui, F. Li, X. Zhou, and F. Pan, "Recent progress in voltage control of magnetism: Materials, mechanisms, and performance," *Prog. Mater. Sci.*, vol. 87, pp. 33–82, 2017.

[2] M. Weisheit, S. Fähler, A. Marty, Y. Souche, C. Poinsignon, and D. Givord, "Electric field-induced modification of magnetism in thin-film ferromagnets," *Science (80-.).*, vol. 315, no. 5810, pp. 349–351, 2007.

[3] S. S. P. Parkin, M. Hayashi, and L. Thomas, "Magnetic domain-wall racetrack memory," *Science (80-.).*, vol. 320, no. 5873, pp. 190–194, 2008.

[4] T. Nozaki *et al.*, "Recent progress in the voltage-controlled magnetic anisotropy effect and the challenges faced in developing voltage-torque MRAM," *Micromachines*, vol. 10, no. 5, p. 327, May 2019.

[5] Y. Huai, "Spin-transfer torque MRAM (STT-MRAM): Challenges and prospects," *AAPPS Bull.*, vol. 18, no. 6, pp. 33–40, 2008.

[6] P. M. Tedrow and R. Meservey, "Spin-Dependent Tunneling into Ferromagnetic Nickel," *Phys. Rev. Lett.*, vol. 26, no. 4, p. 192, Jan. 1971.

[7] M. Julliere, "Tunneling between ferromagnetic films," *Phys. Lett. A*, vol. 54, no. 3, pp. 225–226, Sep. 1975.

[8] J. S. Moodera, L. R. Kinder, T. M. Wong, and R. Meservey, "Large Magnetoresistance at Room Temperature in Ferromagnetic Thin Film Tunnel Junctions," *Phys. Rev. Lett.*, vol. 74, no. 16, p. 3273, Apr. 1995.

[9] A. Brataas, A. D. Kent, and H. Ohno, "Current-induced torques in magnetic materials," *Nat. Mater.*, vol. 11, no. 5, pp. 372–381, 2012.

[10] M. Arora and Y. Huai, "Spin-transfer torque MRAM (STT-MRAM): Challenges and prospects," *AAPPS Bull.*, vol. 18, no. 6, pp. 33–40, 2008.

[11] Y. Tan *et al.*, "Strain induced magnetic anisotropy of high epitaxial Ni thin films grown on different oriented PMN-PT substrates," *Ceram. Int.*, vol. 44, no. 5, pp. 5564–5568, Apr. 2018.

[12] L. Ranno, A. Llobet, R. Tiron, and E. Favre-Nicolin, “Strain-induced magnetic anisotropy in epitaxial manganite films,” *Appl. Surf. Sci.*, vol. 188, no. 1–2, pp. 170–175, Mar. 2002.

[13] N. Di, “Electric and chemical manipulation of magnetic anisotropy of ultrathin ferromagnetic films,” Ecole Polytechnique, 2015.

[14] N. Tournerie, A. P. Engelhardt, F. Maroun, and P. Allongue, “Influence of the surface chemistry on the electric-field control of the magnetization of ultrathin films,” *Phys. Rev. B - Condens. Matter Mater. Phys.*, vol. 86, no. 10, pp. 1–5, 2012.

[15] M. Jaafar *et al.*, “Pattern-induced magnetic anisotropy in FePt thin films by ion irradiation,” *Phys. Rev. B - Condens. Matter Mater. Phys.*, vol. 83, no. 9, p. 094422, Mar. 2011.

[16] M. Matczak *et al.*, “Tailoring magnetic anisotropy gradients by ion bombardment for domain wall positioning in magnetic multilayers with perpendicular anisotropy,” *Nanoscale Res. Lett.*, vol. 9, no. 1, pp. 1–7, Dec. 2014.

[17] K. Nakamura, R. Shimabukuro, Y. Fujiwara, T. Akiyama, T. Ito, and A. J. Freeman, “Giant modification of the magnetocrystalline anisotropy in transition-metal monolayers by an external electric field,” *Phys. Rev. Lett.*, vol. 102, no. 18, p. 187201, May 2009.

[18] M. Tsujikawa and T. Oda, “Finite electric field effects in the large perpendicular magnetic anisotropy surface Pt/Fe/Pt(001): A first-principles study,” *Phys. Rev. Lett.*, vol. 102, no. 24, p. 247203, Jun. 2009.

[19] U. Bauer, M. Przybylski, J. Kirschner, and G. S. D. Beach, “Magnetoelectric charge trap memory,” *Nano Lett.*, vol. 12, no. 3, pp. 1437–1442, 2012.

[20] B. Dieny and M. Chshiev, “Perpendicular magnetic anisotropy at transition metal/oxide interfaces and applications,” *Rev. Mod. Phys.*, vol. 89, no. 2, 2017.

[21] F. Bonell *et al.*, “Reversible change in the oxidation state and magnetic circular dichroism of Fe driven by an electric field at the FeCo/MgO interface,” *Appl. Phys. Lett.*, vol. 102, no. 15, p. 152401, Apr. 2013.

[22] A. J. Schellekens, A. Van Den Brink, J. H. Franken, H. J. M. Swagten, and B. Koopmans, “Electric-field control of domain wall motion in perpendicularly magnetized materials,”

Nat. Commun., vol. 3, no. May, pp. 845–847, 2012.

[23] L. Xu and S. Zhang, "Electric field control of interface magnetic anisotropy," *J. Appl. Phys.*, vol. 111, no. 7, p. 07C501, Feb. 2012.

[24] S. E. Barnes, J. Ieda, and S. Maekawa, "Rashba Spin-Orbit Anisotropy and the Electric Field Control of Magnetism," *Sci. Reports 2014 41*, vol. 4, no. 1, pp. 1–5, Feb. 2014.

[25] K. Nakamura, T. Akiyama, T. Ito, M. Weinert, and A. J. Freeman, "Role of an interfacial FeO layer in the electric-field-driven switching of magnetocrystalline anisotropy at the Fe/MgO interface," *Phys. Rev. B - Condens. Matter Mater. Phys.*, vol. 81, no. 22, p. 220409, Jun. 2010.

[26] T. Maruyama *et al.*, "Large voltage-induced magnetic anisotropy change in a few atomic layers of iron," *Nat. Nanotechnol. 2009 43*, vol. 4, no. 3, pp. 158–161, Jan. 2009.

[27] T. Nozaki, Y. Shiota, M. Shiraishi, T. Shinjo, and Y. Suzuki, "Voltage-induced perpendicular magnetic anisotropy change in magnetic tunnel junctions," *Appl. Phys. Lett.*, vol. 96, no. 2, p. 022506, Jan. 2010.

[28] K. Kita, D. W. Abraham, M. J. Gajek, and D. C. Worledge, "Electric-field-control of magnetic anisotropy of Co0.6Fe0.2B0.2/oxide stacks using reduced voltage," *J. Appl. Phys.*, vol. 112, no. 3, p. 033919, Aug. 2012.

[29] S. S. Ha *et al.*, "Voltage induced magnetic anisotropy change in ultrathin Fe80Co20/MgO junctions with Brillouin light scattering," *Appl. Phys. Lett.*, vol. 96, no. 14, p. 142512, Apr. 2010.

[30] U. Bauer *et al.*, "Magneto-ionic control of interfacial magnetism," *Nat. Mater. 2014 142*, vol. 14, no. 2, pp. 174–181, Nov. 2014.

[31] G. Yu *et al.*, "Strain-induced modulation of perpendicular magnetic anisotropy in Ta/CoFeB/MgO structures investigated by ferromagnetic resonance," *Appl. Phys. Lett.*, vol. 106, no. 7, p. 072402, Feb. 2015.

[32] A. J. Tan *et al.*, "Magneto-ionic control of magnetism using a solid-state proton pump," *Nat. Mater.*, vol. 18, no. 1, pp. 35–41, 2019.

[33] B. D. Adams and A. Chen, "The role of palladium in a hydrogen economy," *Mater. Today*,

vol. 14, no. 6, pp. 282–289, Jun. 2011.

[34] L. Schlapbach and A. Züttel, “Hydrogen-storage materials for mobile applications,” *Nat. 2001 4146861*, vol. 414, no. 6861, pp. 353–358, Nov. 2001.

[35] H. Yang, A. Thiaville, S. Rohart, A. Fert, and M. Chshiev, “Anatomy of Dzyaloshinskii-Moriya Interaction at Co/Pt Interfaces,” *Phys. Rev. Lett.*, vol. 115, no. 26, p. 267210, Dec. 2015.

[36] A. Hoffmann, “Spin hall effects in metals,” *IEEE Trans. Magn.*, vol. 49, no. 10, pp. 5172–5193, 2013.

[37] S. M. Valvidares, J. Dorantes-Dávila, H. Isern, S. Ferrer, and G. M. Pastor, “Interface-driven manipulation of the magnetic anisotropy of ultrathin Co films on Pt(111): Substrate deposition of hydrogen and model calculations,” *Phys. Rev. B - Condens. Matter Mater. Phys.*, vol. 81, no. 2, pp. 1–11, 2010.

[38] K. Klyukin, G. Beach, and B. Yildiz, “Hydrogen tunes magnetic anisotropy by affecting local hybridization at the interface of a ferromagnet with nonmagnetic metals,” *Phys. Rev. Mater.*, vol. 4, no. 10, pp. 1–7, 2020.

[39] M. Gößler, S. Topolovec, H. Krenn, and R. Würschum, “Nanoporous Pd1-xCoxfor hydrogen-intercalation magneto-ionics,” *APL Mater.*, vol. 9, no. 4, 2021.

[40] F. Maroun *et al.*, “Potential dependence of the structure and magnetism of electrodeposited Pd/Co/Au(111) layers,” *J. Electroanal. Chem.*, vol. 819, no. 111, pp. 322–330, 2018.

[41] N. Tournerie, A. Engelhardt, F. Maroun, and P. Allongue, “Probing the electrochemical interface with in situ magnetic characterizations: A case study of Co/Au(111) layers,” *Surf. Sci.*, vol. 631, pp. 88–95, 2015.

[42] A. D. Lamirand, J. P. Adam, D. Ravelosona, P. Allongue, and F. Maroun, “In situ monitoring of electric field effect on domain wall motion in Co ultrathin films in direct contact with an electrolyte,” *Appl. Phys. Lett.*, vol. 115, no. 3, p. 032402, 2019.

[43] U. Gradmann, “Chapter 1 Magnetism in ultrathin transition metal films,” vol. 7, Elsevier, 1993, pp. 1–96.

[44] Y. Kakehashi, “Introduction to Magnetism,” *Springer Ser. Solid-State Sci.*, vol. 175, pp. 1–28, 2013.

[45] S. Chikazumi, *Physics of Ferromagnetism*. OUP Oxford, 2009.

[46] J. Bland and B. Heinrich, *Ultrathin Magnetic Structures I: An Introduction to the Electronic, Magnetic and Structural Properties*. 2005.

[47] M. T. Johnson, P. J. H. Bloemen, F. J. A. Den Broeder, and J. J. De Vries, “Magnetic anisotropy in metallic multilayers,” *Reports Prog. Phys.*, vol. 59, no. 11, pp. 1409–1458, 1996.

[48] I. F. Lyuksyutov, T. Nattermann, and V. Pokrovsky, “Theory of the hysteresis loop in ferromagnets,” *Phys. Rev. B - Condens. Matter Mater. Phys.*, vol. 59, no. 6, pp. 4260–4272, 1999.

[49] G. Savidand, “Effets d’interfaces sur le retournement de l’aimantation de couches ultraminces électrodéposées de Co sur Au (111),” Ecole Polytechnique, 2007.

[50] M. S. Milan Paunovic, “Kinetics and Mechanism of Electrodeposition,” in *Fundamentals of Electrochemical Deposition*, John Wiley & Sons, Ltd, 2006, pp. 77–112.

[51] J. O. Bockris and A. K. N. Reddy, *Modern Electrochemistry: An Introduction to an Interdisciplinary Area, Volume 1*, vol. 1. Springer US, 1970.

[52] A. J. Bard and L. R. Faulkner, *Electrochemical Methods: Fundamentals and Applications, 2nd Edition | Wiley*. John Wiley & Sons, Incorporated, 2008.

[53] P. W. Atkins, *Physical chemistry*. Oxford; New York: Oxford University Press, 1990.

[54] P. Allongue and F. Maroun, “Metal electrodeposition on single crystal metal surfaces mechanisms, structure and applications,” *Curr. Opin. Solid State Mater. Sci.*, vol. 10, no. 3–4, pp. 173–181, 2006.

[55] J. K. Nørskov *et al.*, “Trends in the Exchange Current for Hydrogen Evolution,” *J. Electrochem. Soc.*, vol. 152, no. 3, p. J23, 2005.

[56] K. Munbodh, F. A. Perez, C. Keenan, D. Lederman, M. Zhernenkov, and M. R. Fitzsimmons, “Effects of hydrogen/deuterium absorption on the magnetic properties of

Co/Pd multilayers," *Phys. Rev. B - Condens. Matter Mater. Phys.*, vol. 83, no. 9, pp. 1–10, 2011.

[57] J. O. Bockris, J. McBreen, and L. Nanis, "The Hydrogen Evolution Kinetics and Hydrogen Entry into a-Iron," *J. Electrochem. Soc.*, vol. 112, no. 10, p. 1025, Oct. 1965.

[58] J. O. M. Bockris, M. A. genshaw, and M. Fullenwider, "The electro-permeation of hydrogen into metals," *Electrochim. Acta*, vol. 15, no. 1, pp. 47–60, 1970.

[59] A. Lasia, "Hydrogen evolution reaction," *Handb. Fuel Cells*, no. June 2003, 2010.

[60] S. Trasatti, "Work function, electronegativity, and electrochemical behaviour of metals. III. Electrolytic hydrogen evolution in acid solutions," *J. Electroanal. Chem.*, vol. 39, no. 1, pp. 163–184, Sep. 1972.

[61] B. E. Conway and G. Jerkiewicz, "Relation of energies and coverages of underpotential and overpotential deposited H at Pt and other metals to the 'volcano curve' for cathodic H2 evolution kinetics," *Electrochim. Acta*, vol. 45, no. 25–26, pp. 4075–4083, Aug. 2000.

[62] C. Li and J. B. Baek, "Recent Advances in Noble Metal (Pt, Ru, and Ir)-Based Electrocatalysts for Efficient Hydrogen Evolution Reaction," *ACS Omega*, vol. 5, no. 1, pp. 31–40, Jan. 2019.

[63] R. Parsons, "The rate of electrolytic hydrogen evolution and the heat of adsorption of hydrogen," *Trans. Faraday Soc.*, vol. 54, pp. 1053–1063, 1958.

[64] W. Zhou *et al.*, "Recent developments of carbon-based electrocatalysts for hydrogen evolution reaction," *Nano Energy*, vol. 28. pp. 29–43, 2016.

[65] R. V. Digraskar, V. S. Sapner, S. M. Mali, S. S. Narwade, A. V. Ghule, and B. R. Sathe, "CZTS Decorated on Graphene Oxide as an Efficient Electrocatalyst for High-Performance Hydrogen Evolution Reaction," *ACS Omega*, vol. 4, no. 4, pp. 7650–7657, Apr. 2019.

[66] S. Dutta *et al.*, "Chemical and structural engineering of transition metal boride towards excellent and sustainable hydrogen evolution reaction," *Nano Energy*, vol. 67, p. 104245, Jan. 2020.

[67] J. M. D. Coey, "Introduction," in *Magnetism and Magnetic Materials*, Cambridge

University Press, 2012, pp. 1–23.

[68] P. J. Metaxas *et al.*, “Creep and flow regimes of magnetic domain-wall motion in ultrathin Pt/Co/Pt films with perpendicular anisotropy,” *Phys. Rev. Lett.*, vol. 99, no. 21, pp. 1–4, 2007.

[69] S. Lemerle, J. Ferré, C. Chappert, V. Mathet, T. Giamarchi, and P. Le Doussal, “Domain wall creep in an ising ultrathin magnetic film,” *Phys. Rev. Lett.*, vol. 80, no. 4, pp. 849–852, 1998.

[70] S. Lemerle, “Etude de la dynamique de renversement de l’aimantation dans les couches ultra-minces à anisotropie perpendiculaire : rôle de la nanostructure,” 1998.

[71] D. S. Fisher, M. P. A. Fisher, and D. A. Huse, “Thermal fluctuations, quenched disorder, phase transitions, and transport in type-II superconductors,” *Phys. Rev. B*, vol. 43, no. 1, pp. 130–159, Jan. 1991.

[72] E. E. Ferrero, S. Bustingorry, A. B. Kolton, and A. Rosso, “Numerical approaches on driven elastic interfaces in random media,” *Comptes Rendus Phys.*, vol. 14, no. 8, pp. 641–650, 2013.

[73] P. Chauve, T. Giamarchi, and P. Le Doussal, “Creep and depinning in disordered media,” *Phys. Rev. B*, vol. 62, no. 10, pp. 6241–6267, Sep. 2000.

[74] V. Jeudy *et al.*, “Universal Pinning Energy Barrier for Driven Domain Walls in Thin Ferromagnetic Films,” *Phys. Rev. Lett.*, vol. 117, no. 5, pp. 1–5, 2016.

[75] M. Oba, K. Nakamura, T. Akiyama, T. Ito, M. Weinert, and A. J. Freeman, “Electric-Field-Induced Modification of the Magnon Energy, Exchange Interaction, and Curie Temperature of Transition-Metal Thin Films,” *Phys. Rev. Lett.*, vol. 114, no. 10, p. 107202, Mar. 2015.

[76] G. H. O. Daalderop, P. J. Kelly, and M. F. H. Schuurmans, “Magnetocrystalline anisotropy and orbital moments in transition-metal compounds,” *Phys. Rev. B*, vol. 44, no. 21, p. 12054, Dec. 1991.

[77] T. Dietl and H. Ohno, “Dilute ferromagnetic semiconductors: Physics and spintronic structures,” *Rev. Mod. Phys.*, vol. 86, no. 1, pp. 187–251, Mar. 2014.

[78] S. von Molnár, H. Munekata, H. Ohno, and L. L. Chang, “New diluted magnetic semiconductors based on III–V compounds,” *J. Magn. Magn. Mater.*, vol. 93, no. C, pp. 356–364, Feb. 1991.

[79] D. Chiba, H. Yamanouchi, F. Hatsukura, and H. Ohno, “Electrical manipulation of magnetization reversal in a ferromagnetic semiconductor,” *Science (80-.).*, vol. 301, no. 5635, pp. 943–945, Aug. 2003.

[80] M. Endo, S. Kanai, S. Ikeda, F. Matsukura, and H. Ohno, “Electric-field effects on thickness dependent magnetic anisotropy of sputtered MgO/Co40Fe40B20/Ta structures,” *Appl. Phys. Lett.*, vol. 96, no. 21, p. 212503, May 2010.

[81] A. Okada, S. Kanai, M. Yamanouchi, S. Ikeda, F. Matsukura, and H. Ohno, “Electric-field effects on magnetic anisotropy and damping constant in Ta/CoFeB/MgO investigated by ferromagnetic resonance,” *Appl. Phys. Lett.*, vol. 105, no. 5, p. 052415, Aug. 2014.

[82] K. W. Park *et al.*, “Electric field control of magnetic anisotropy in the easy cone state of Ta/Pt/CoFeB/MgO structures,” *Appl. Phys. Lett.*, vol. 109, no. 1, p. 012405, Jul. 2016.

[83] U. Bauer, S. Emori, and G. S. D. Beach, “Electric field control of domain wall propagation in Pt/Co/GdOx films,” *Appl. Phys. Lett.*, vol. 100, no. 19, 2012.

[84] U. Bauer, S. Emori, and G. S. D. Beach, “Voltage-gated modulation of domain wall creep dynamics in an ultrathin metallic ferromagnet,” *Appl. Phys. Lett.*, vol. 101, no. 17, p. 172403, Oct. 2012.

[85] U. Bauer *et al.*, “Magneto-ionic control of interfacial magnetism,” *Nat. Mater. 2014 142*, vol. 14, no. 2, pp. 174–181, Nov. 2014.

[86] C. Bi *et al.*, “Reversible control of Co magnetism by voltage-induced oxidation,” *Phys. Rev. Lett.*, vol. 113, no. 26, p. 267202, Dec. 2014.

[87] D. A. Gilbert *et al.*, “Structural and magnetic depth profiles of magneto-ionic heterostructures beyond the interface limit,” *Nat. Commun. 2016 71*, vol. 7, no. 1, pp. 1–8, Jul. 2016.

[88] W. G. Wang, M. Li, S. Hageman, and C. L. Chien, “Electric-field-assisted switching in magnetic tunnel junctions,” *Nat. Mater. 2011 111*, vol. 11, no. 1, pp. 64–68, Nov. 2011.

[89] S. Kanai, M. Yamanouchi, S. Ikeda, Y. Nakatani, F. Matsukura, and H. Ohno, “Electric field-induced magnetization reversal in a perpendicular-anisotropy CoFeB-MgO magnetic tunnel junction,” *Appl. Phys. Lett.*, vol. 101, no. 12, p. 122403, Sep. 2012.

[90] W. Lin *et al.*, “Universal domain wall dynamics under electric field in Ta/CoFeB/MgO devices with perpendicular anisotropy,” *Nat. Commun. 2016 71*, vol. 7, no. 1, pp. 1–6, Nov. 2016.

[91] D. Chiba *et al.*, “Electric-field control of magnetic domain-wall velocity in ultrathin cobalt with perpendicular magnetization,” *Nat. Commun.*, vol. 3, no. May, pp. 887–888, 2012.

[92] A. Hubert and R. Schäfer, *Magnetic Domains: The Analysis of Magnetic Microstructures*. Springer, 1998.

[93] C. Daboo, J. A. C. Bland, R. J. Hicken, A. J. R. Ives, M. J. Baird, and M. J. Walker, “Vectorial magnetometry with the magneto-optic Kerr effect applied to Co/Cu/Co trilayer structures,” *Phys. Rev. B*, vol. 47, no. 18, pp. 11852–11859, May 1993.

[94] W. S. Kim, M. Aderholz, and W. Kleemann, “Calibration of polar Kerr rotation and ellipticity measurements,” *Meas. Sci. Technol.*, vol. 4, no. 11, pp. 1275–1280, 1993.

[95] J. McCord, “Progress in magnetic domain observation by advanced magneto-optical microscopy,” *J. Phys. D. Appl. Phys.*, vol. 48, no. 33, 2015.

[96] J. J. Mallett, E. B. Svedberg, J. E. Bonevich, A. J. Shapiro, W. F. Egelhoff, and T. P. Moffat, “Compositional Control in Electrodeposited Ni[sub x]Pt[sub 1−x] Films,” *J. Electrochem. Soc.*, vol. 155, no. 1, p. D1, 2008.

[97] B. W. Gregory and J. L. Stickney, “Electrochemical atomic layer epitaxy (ECALE),” *J. Electroanal. Chem. Interfacial Electrochem.*, vol. 300, no. 1–2, pp. 543–561, Feb. 1991.

[98] W. Chen, P. Yen, Y. Kuo, S. Chen, and S. Yau, “Epitaxial electrodeposition of nickel on Pt(111) electrode,” *J. Phys. Chem. C*, vol. 116, no. 40, pp. 21343–21349, 2012.

[99] P. Allongue, F. Maroun, H. F. Jurca, N. Tournerie, G. Savidand, and R. Cortès, “Magnetism of electrodeposited ultrathin layers: Challenges and opportunities,” *Surf. Sci.*, vol. 603, no. 10–12, pp. 1831–1840, 2009.

[100] L. Cagnon *et al.*, “Enhanced interface perpendicular magnetic anisotropy in electrodeposited Co/Au(111) layers,” *Phys. Rev. B - Condens. Matter Mater. Phys.*, vol. 63, no. 10, pp. 1044191–10441912, 2001.

[101] P. Allongue and F. Maroun, “Electrodeposited magnetic layers in the ultrathin limit,” *MRS Bull.*, vol. 35, no. 10, pp. 761–770, 2010.

[102] P. Allongue, L. Cagnon, C. Gomes, A. Gündel, and V. Costa, “Electrodeposition of Co and Ni/Au(1 1 1) ultrathin layers. Part I: Nucleation and growth mechanisms from in situ STM,” *Surf. Sci.*, vol. 557, no. 1–3, pp. 41–56, 2004.

[103] L. H. Mendoza-Huizar and C. H. Rios-Reyes, “Underpotential deposition of cobalt onto polycrystalline platinum,” *J. Solid State Electrochem.*, vol. 15, no. 4, pp. 737–745, 2011.

[104] P. Y. Yen, S. Chen, H. L. Tu, H. Wu, S. L. Yau, and J. S. Tsay, “Epitaxial electrodeposition of cobalt on a Pt(111) electrode covered with a Cu(111) film,” *J. Phys. Chem. C*, vol. 115, no. 48, pp. 23802–23808, 2011.

[105] L. Cagnon *et al.*, “Anion effect in Co/Au(111) electrodeposition: structure and magnetic behavior,” *Appl. Surf. Sci.*, vol. 164, no. 1–4, pp. 22–28, Sep. 2000.

[106] P. Prod’homme *et al.*, “Preparation, characterization and magneto-optical investigations of electrodeposited Co/Au films,” *J. Magn. Magn. Mater.*, vol. 315, no. 1, pp. 26–38, Aug. 2007.

[107] D. Matsumura, T. Yokoyama, K. Amemiya, S. Kitagawa, and T. Ohta, “CO induced spin reorientation transition of Co/Pd(111) studied by XMCD and XPS,” *Phys. Scr. T*, vol. T115, no. 111, pp. 583–585, 2005.

[108] X. Zhang *et al.*, “Interface effects on perpendicular magnetic anisotropy for molecular-capped cobalt ultrathin films,” *Appl. Phys. Lett.*, vol. 99, no. 16, pp. 97–100, 2011.

[109] D. Matsumura, T. Yokoyama, K. Amemiya, S. Kitagawa, and T. Ohta, “XPS and XMCD studies on spin reorientation transition of Co / Pd (111) induced by surface CO chemisorption,” *Phys. Scr.*, vol. T115, pp. 583–585, 2005.

[110] D. Matsumura *et al.*, “Surface structure of CO on CoPd(111) magnetic thin films and its effect on the spin reorientation transition of the film,” *Phys. Rev. B - Condens. Matter Mater. Phys.*, vol. 73, no. 17, pp. 1–9, 2006.

[111] R. Wang, U. Bertocci, H. Tan, L. A. Bendersky, and T. P. Moffat, “Self-Terminated Electrodeposition of Ni, Co, and Fe Ultrathin Films,” *J. Phys. Chem. C*, vol. 120, no. 29, pp. 16228–16237, 2016.

[112] D. Matsumura *et al.*, “Magnetization process of Co/Pd(1 1 1) thin films: Chemisorption-induced spin-reorientation transition,” *Surf. Sci.*, vol. 602, no. 11, pp. 1999–2003, 2008.

[113] N. Collas, B. Beden, J. M. Leger, and C. Lamy, “A simultaneous voltammetric and uv-visible reflectance spectroscopic investigation of the adsorption of carbon monoxide on a platinum electrode in aqueous solution,” *J. Electroanal. Chem.*, vol. 186, no. 1–2, pp. 287–297, 1985.

[114] M. Baca *et al.*, “A comparison of hydrogen storage in Pt, Pd and Pt/Pd alloys loaded disordered mesoporous hollow carbon spheres,” *Nanomaterials*, vol. 8, no. 9, pp. 15–20, 2018.

[115] M. Yamauchi, H. Kobayashi, and H. Kitagawa, “Hydrogen storage mediated by Pd and Pt nanoparticles,” *ChemPhysChem*, vol. 10, no. 15, pp. 2566–2576, 2009.

[116] N. Dubouis and A. Grimaud, “The hydrogen evolution reaction: from material to interfacial descriptors,” *Chem. Sci.*, vol. 10, no. 40, pp. 9165–9181, Oct. 2019.

[117] A. Czerwiński, R. Marassi, and S. Zamponi, “The absorption of hydrogen and deuterium in thin palladium electrodes. Part I. Acidic solutions,” *J. Electroanal. Chem.*, vol. 316, no. 1–2, pp. 211–221, Oct. 1991.

[118] K. A. Stoerzinger *et al.*, “Probing the Surface of Platinum during the Hydrogen Evolution Reaction in Alkaline Electrolyte,” *J. Phys. Chem. B*, vol. 122, no. 2, pp. 864–870, 2018.

[119] M. Ruge *et al.*, “Structural Reorganization of Pt(111) Electrodes by Electrochemical Oxidation and Reduction,” *J. Am. Chem. Soc.*, vol. 139, no. 12, pp. 4532–4539, Mar. 2017.

[120] M. Belmeguenai *et al.*, “Interfacial Dzyaloshinskii-Moriya interaction in perpendicularly magnetized Pt/Co/AlOx ultrathin films measured by Brillouin light spectroscopy,” *Phys. Rev. B - Condens. Matter Mater. Phys.*, vol. 91, no. 18, pp. 1–4, 2015.

[121] T. Ueno *et al.*, “Enhanced orbital magnetic moments in magnetic heterostructures with interface perpendicular magnetic anisotropy,” *Sci. Rep.*, vol. 5, no. September, pp. 1–7, 2015.

[122] S. Bandiera, R. R. Sousa, B. B. Rodmacq, and B. Dieny, “Asymmetric interfacial perpendicular magnetic anisotropy in pt/co/pt trilayers,” *IEEE Magn. Lett.*, vol. 2, p. 3000504, 2011.

[123] A. Y. Y. Chatalov, “Effet du pH sur le comportement électrochimique des métaux et leur résistance à la corrosion,” *Dokl Akad Nauk*, vol. S.S.S.R, no. 86, pp. 775–777, 1952.

[124] T. A. Moore *et al.*, “High domain wall velocities induced by current in ultrathin Pt/Co/AlOx wires with perpendicular magnetic anisotropy,” *Appl. Phys. Lett.*, vol. 93, no. 26, pp. 1–4, 2008.

[125] C. Lueng, F. Zighem, D. Faurie, and M. Kostylev, “Ferromagnetic resonance investigation of physical origins of modification of the perpendicular magnetic anisotropy in Pd/Co layered films in the presence of hydrogen gas,” *J. Appl. Phys.*, vol. 122, no. 16, 2017.

[126] R. Vollmer, T. Gutjahr-Löser, J. Kirschner, S. van Dijken, and B. Poelsema, “Spin-reorientation transition in Ni films on Cu(001): The influence of H2 adsorption,” *Phys. Rev. B - Condens. Matter Mater. Phys.*, vol. 60, no. 9, pp. 6277–6280, 1999.

[127] B. Santos *et al.*, “Hydrogen-induced reversible spin-reorientation transition and magnetic stripe domain phase in bilayer Co on Ru(0001),” *Phys. Rev. B - Condens. Matter Mater. Phys.*, vol. 85, no. 13, pp. 3–8, 2012.

[128] B. Újfalussy, L. Szunyogh, P. Bruno, and P. Weinberger, “First-Principles Calculation of the Anomalous Perpendicular Anisotropy in a Co Monolayer on Au(111),” *Phys. Rev. Lett.*, vol. 77, no. 9, pp. 1805–1808, 1996.

[129] R. Hammerling, C. Uiberacker, J. Zabloudil, P. Weinberger, L. Szunyogh, and J. Kirschner, “Magnetic anisotropy of thin films of Co on Cu(111),” *Phys. Rev. B - Condens. Matter Mater. Phys.*, vol. 66, no. 5, pp. 524021–524024, 2002.

[130] J. Dorantes-Dávila, H. Dreyssé, and G. M. Pastor, “Magnetic Anisotropy of Transition-Metal Interfaces from a Local Perspective: Reorientation Transitions and Spin-Canted

Phases in Pd Capped Co Films on Pd(111)," *Phys. Rev. Lett.*, vol. 91, no. 19, p. 197206, 2003.

[131] A. Shick, D. Novikov, and A. Freeman, "Relativistic spin-polarized theory of magnetoelastic coupling and magnetic anisotropy strain dependence: Application to Co/Cu(001)," *Phys. Rev. B - Condens. Matter Mater. Phys.*, vol. 56, no. 22, pp. R14259–R14262, 1997.

[132] K. M. E. Habermehl-Cwirzen, K. Kauraala, and J. Lahtinen, "Hydrogen on cobalt: The effects of carbon monoxide and sulphur additives on the D2/Co(0001) System," *Phys. Scr. T*, vol. T108, no. 0001, pp. 28–32, 2004.

[133] E. R. Cave *et al.*, "Trends in the Catalytic Activity of Hydrogen Evolution during CO2 Electroreduction on Transition Metals," *ACS Catal.*, vol. 8, no. 4, pp. 3035–3040, 2018.

[134] X. Ye *et al.*, "Magnetoelectric Tuning of Pinning-Type Permanent Magnets through Atomic-Scale Engineering of Grain Boundaries," *Adv. Mater.*, vol. 33, no. 5, pp. 2–8, 2021.

[135] P. C. Chang, C. M. Liu, C. C. Hsu, and W. C. Lin, "Hydrogen-mediated magnetic domain formation and domain wall motion in Co30Pd70 alloy films," *Sci. Reports 2018 81*, vol. 8, no. 1, pp. 1–13, Apr. 2018.

[136] H. C. Jamieson, G. C. Weatherly, and F. D. Manchester, "The β → α phase transformation in palladium-hydrogen alloys," *J. Less Common Met.*, vol. 50, no. 1, pp. 85–102, Nov. 1976.

[137] E. Gileadi, M. A. Fullenwider, and J. O. Bockris, "The Permeation of Electrolytic Hydrogen through Platinum," *J. Electrochem. Soc.*, vol. 113, no. 9, p. 926, 1966.

[138] L. Gao and B. E. Conway, "Absorption and adsorption of H in the H2 evolution reaction and the effects of co-adsorbed poisons," *Electrochim. Acta*, vol. 39, no. 11–12, pp. 1681–1693, 1994.

[139] M. G. T. Burrows and W. H. Stookmayer, "The poisoning of a palladium catalyst by carbon monoxide," *Proc. R. Soc. London. Ser. A. Math. Phys. Sci.*, vol. 176, no. 967, pp. 474–483, Nov. 1940.

[140] C. P. O'Brien and I. C. Lee, "CO Poisoning and CO Hydrogenation on the Surface of

Pd Hydrogen Separation Membranes," *J. Phys. Chem. C*, vol. 121, no. 31, pp. 16864–16871, Aug. 2017.

[141] E. ~C. Stoner and E. ~P. Wohlfarth, "A mechanism of magnetic hysteresis in heterogeneous alloys," *Philos. Trans. R. Soc. London. Ser. A, Math. Phys. Sci.*, vol. 240, no. 826, pp. 599–642, 1948.

[142] C. Tannous and J. Gieraltowski, "The Stoner-Wohlfarth model of ferromagnetism," *Eur. J. Phys.*, vol. 29, no. 3, pp. 475–487, 2008.

[143] N. H. Kim *et al.*, "Role of top and bottom interfaces of a Pt/Co/AlOx system in Dzyaloshinskii-Moriya interaction, interface perpendicular magnetic anisotropy, and magneto-optical Kerr effect," *AIP Adv.*, vol. 7, no. 3, 2017.

[144] U. K. Rößler, A. N. Bogdanov, and C. Pfleiderer, "Spontaneous skyrmion ground states in magnetic metals," *Nature*, vol. 442, no. 7104, pp. 797–801, Aug. 2006.

[145] A. R. Fert, "Magnetic and Transport Properties of Metallic Multilayers," *Mater. Sci. Forum*, vol. 59–60, pp. 439–480, Jan. 1990.

[146] T. Srivastava *et al.*, "Large-Voltage Tuning of Dzyaloshinskii-Moriya Interactions: A Route toward Dynamic Control of Skyrmion Chirality," *Nano Lett.*, vol. 18, no. 8, pp. 4871–4877, 2018.

[147] K. Nawaoka *et al.*, "Voltage induction of interfacial Dzyaloshinskii-Moriya interaction in Au/Fe/MgO artificial multilayer," *APExp*, vol. 8, no. 6, p. 063004, Jun. 2015.

DOCTORAL SCHOOL

Titre : Influence de l'hydrogène sur les propriétés magnétiques de films ultraminces de cobalt en contact avec un électrolyte

Mots clés : Ferromagnétisme, Cobalt, Réaction d'évolution de l'hydrogène (HER), paroi de domaine magnétique

Résumé : Les flms magnétiques ultra-minces ont été étudiés depuis de nombreuses années en raison de leurs diverses applications. De nos jours, la réduction de la consommation d'énergie dans le processus d'écriture des dispositifs à base de matériaux magnétiques est cruciale. Une façon d'atteindre cet objectif est le contrôle du magnétisme par une tension électrique qui permet des modifications des propriétés magnétiques en appliquant un potentiel à l'échantillon. L'application de cette tension à l'interface électrochimique présente plusieurs avantages comme un champ électrique important et spatialement homogène. Dans cette thèse, nous étudions les modifications des propriétés magnétiques de couches de cobalt d'épaisseur nanométrique par une réaction électrochimique contrôlée par le potentiel (la décomposition de l'eau en hydrogène). Nous utilisons deux méthodes différentes pour la préparation des couches de cobalt et leur stabilisation dans un électrolyte. Nous montrons que les changements magnétiques sont dus à la diffusion d'hydrogène dans le substrat et à l'interface entre le substrat et la couche de cobalt.

Title : Influence of hydrogen on the magnetic properties of ultrathin cobalt films in contact with electrolyte

Keywords : Ferromagnetism, Cobalt, Hydrogen evolution reaction (HER), magnetic domain wall, voltage control magnetism

Abstract : Magnetic thin films have been investigated since many years because of their various applications. Nowadays, reducing energy consumption in the writing process of magnetic material-based devices is crucial. One way to reach this goal is voltage control magnetism which enables modifications of magnetic property by applying a potential on the sample. Applying this voltage at the electrochemical interface has several benefits as a large and a spatially homogeneous electric field. In this thesis, we investigate the modifications of the magnetic properties of nanometer thick cobalt layers by an electrochemical reaction controlled by the potential (water splitting into hydrogen). We use two different methods for the preparation of the cobalt layers and their stabilization in an electrolyte. We show that the magnetic changes are due to hydrogen diffusion in the substrate and at the interface between the substrate and the cobalt layer.

Institut Polytechnique de Paris
91120 Palaiseau, France